DYNAMIC RESPONSE OF ELECTRONIC SYSTEMS: AN IMPLEMENTATION AND APPLICATION OF TIME-DEPENDENT DENSITY-FUNCTIONAL-THEORY

By

Ryan Michael Hatcher

Dissertation

Submitted to the Faculty of the

Graduate School of Vanderbilt University

in partial fulfillment of the requirements

for the degree of

DOCTOR OF PHILOSOPHY

in

Physics

August, 2007

Nashville, Tennessee

Approved:

Professor Sokrates T. Pantelides

Professor Alan R. Tackett

Professor Richard F. Haglund

Professor Paul D. Sheldon

Professor Sait A. Umar

To my beautiful daughter, Emily

ACKNOWLEDGEMENTS

I want to thank my parents first and foremost for their love and patience. I am unable to express in words how much their advice, generosity and unflinching support has meant to me. I would also like to thank my sister, Amy, and my brother-in-law, Brian for their unconditional support, love and encouragement.

I am grateful to Drs. Alan Wright and Normand Modine at Sandia National Laboratory for inviting me to participate in the Socorro project. I learned a tremendous amount about high performance computing codes while contributing to Socorro in large part due to their patient instruction. I am grateful to count them as friends. The time I spent at Sandia was extraordinarily rewarding – both academically and personally.

I want to thank Professors Natalie Holzwarth and G. Eric Matthews at Wake Forest University. Professor Holzwarth is an exceptional Physicist. She has selflessly and consistently provided outstanding technical advice throughout my time in graduate school. I would like to thank Professor Matthews for inspiring me to pursue a career in Physics when I was an undergraduate. Professor Matthews is a rare and special person and I am very lucky to have had him as my advisor and friend.

I am indebted to the entire staff at the Advanced Computing Center for Research and Education (ACCRE). My graduate school experience was greatly enhanced due to my association with ACCRE. It was a great privilege and honor to have been a part of this organization starting from its humble beginnings to the world-class computing center that it is today. I will also miss the lunches and arguments and the arguments about where to go to lunch!

I want to thank Professors Leonard Feldman, Richard Haglund and Robert Weller at Vanderbilt University for very valuable discussions and advice.

I want to thank all the members of the Solid-State group at Vanderbilt University, especially Drs. Matthew Evans, Leonidas Tsetseris and Matthew Beck who were always there to help me work through problems ranging from theory to coding issues to applications. I also want to thank Debbie Frizzel, Valerie Mauro, and Vicki Abernathy for going above and beyond when organizing my travel, scheduling committee meetings etc. and generally keeping me out of trouble!

I want to thank my advisor, Professor Sokrates Pantelides. I learned a great deal of Physics from him but perhaps the most important lessons were about how to succeed as a professional research scientist. He has a real gift for presenting scientific material and I will always be grateful for his patient and thoughtful feedback.

I want to especially thank my pseudo-advisor, Professor Alan Tackett. Alan has been a mentor, teacher, and friend to me for a long time. He first taught me to program a decade ago. Since then, I have learned more from him about computer hardware, Applied Mathematics/Computer Science, coding, and Physics than anyone. I truly hope that we will remain in contact, both personally and professionally, for the decades to come.

Finally, I would like to acknowledge support by Sandia National Laboratory contract #31411, DOE DSR #16458-A and #16458-B, DOE Computational Materials Science Network, AFOSR MURI grant FA9550-05-1-0306, and the McMinn Endowment at Vanderbilt University. I would also like to acknowledge the computational resources provided by Sandia National Laboratory and ACCRE at Vanderbilt University.

TABLE OF CONTENTS

Page

Chapter

LIST OF TABLES

LIST OF FIGURES

CHAPTER I

INTRODUCTION

1.1. Overview

One of the great scientific achievements of the 20th century is the development of quantum mechanics. Quantum mechanics governs the behavior and interaction of matter and energy at atomic length scales. Although certain properties of macroscopic systems can be treated classically (e.g. fluid dynamics), other properties of even macroscopic systems may be dependent on the quantum mechanical behavior of the constituent atoms (e.g. the photoabsorption spectrum).

In general, a system of atoms (nuclei and electrons) can be described by wavefunctions that are solutions of the Dirac equation. When relativistic effects are negligible, it is sufficient to describe such systems by solving the many-body time-dependent Schrödinger equation (TDSE)

$$i\hbar\frac{\partial}{\partial t}\Psi = \hat{H}\Psi . \tag{1.1}$$

$\hat{H}$ is the many-body Schrödinger Hamiltonian and Ψ is the corresponding wavefunction describing both the electrons and the nuclei. Time-independent systems are described by the time independent Schrödinger equation (SE)

$$\hat{H}\Psi = \varepsilon\Psi , \tag{1.2}$$

where the ε are energy eigenvalues. The SE (1.2) has only been solved analytically for single-electron systems (e.g. the hydrogen atom or He^+). In order to study systems with many electrons, it is necessary to make further approximations and to solve either the SE or the TDSE numerically.

The Hamiltonian in (1.1) and (1.2) for a system of n electrons and N nuclei is

$$\hat{H} = -\sum_I \frac{\hbar^2}{2M_I}\nabla_I^2 - \frac{\hbar^2}{2m_e}\sum_i \nabla_i^2 + \sum_{i<j}\frac{e^2}{\left|\mathbf{r}_i - \mathbf{r}_j\right|} - \sum_{I,i}\frac{e^2 Z_I}{\left|\mathbf{r}_i - \mathbf{R}_I\right|} + \sum_{I<J}\frac{e^2 Z_I Z_J}{\left|\mathbf{R}_I - \mathbf{R}_J\right|}, \tag{1.3}$$

where m_e is the mass of the electron M_I is the mass of the I^{th} nucleus, $\{\mathbf{R}_I\} = \mathbf{R}_1, \mathbf{R}_2, \ldots, \mathbf{R}_N$ are the nuclear coordinates, $\{\mathbf{r}_i\} = \mathbf{r}_1, \mathbf{r}_2, \ldots, \mathbf{r}_n$ are the electron coordinates, ∇_I is the gradient with respect to $\mathbf{R}_I$, and ∇_i is the gradient with respect to $\mathbf{r}_i$.

The slow motion of massive nuclei relative to light-mass electrons allows one to separate the electron and nuclear degrees of freedom by the Born-Oppenheimer approximation [1]. For the time-independent case, eq. (1.2), density functional theory (DFT), introduced by Walter Kohn and coworkers in the 1960's, is a powerful recasting of the resulting many-electron problem in terms of the electron density $n(\mathbf{r})$, eliminating the need to construct explicit many-electron wavefunctions. The original theory was developed for the electronic ground state when the nuclei are at specified positions. It has been applied widely to materials systems for several decades. An extension of the theory introduces time dependence by time stepping the nuclei classically while the electrons remain in their instantaneous ground state. The forces on the nuclei include contributions from the instantaneous electronic Hamiltonian. This semi-classical treatment of the system is generally known as Born-Oppenheimer Molecular Dynamics except when the electrons are treated using DFT where it is commonly referred to as Car-Parrinello Molecular Dynamics [2].

Time-dependent DFT (TDDFT) was formulated in the 1980's as a way to treat the time-dependent many-body problem, eq. (1.1), i.e., allowing time-stepping of both the nuclei and the electron density beyond the ground state. Few implementations of the theory have been reported so far. The focus of this thesis is on the implementation and application of TDDFT to investigate the dynamical response of systems comprised of nuclei and electrons. We consider phenomena that cannot be properly described without the dynamical response of the electrons (i.e. ground-state methods are not able to capture the phenomenon of interest). For example, we apply TDDFT to study the slowing down of energetic ions moving through matter, the nonlinear optical response of noble gases to intense laser light and dynamics of an optical electron-hole pair.

In the remainder of Chapter I, we outline the Born-Oppenheimer as it applies to both the time-independent and the time-dependent SE. We briefly mention alternatives to DFT for the many-electron problem. We then introduce DFT and TDDFT, which are the formalisms we employ to capture the ground-state behavior and dynamics of electrons, respectively. In Chapter II, several algorithms for implementing the time evolution operator are described. We also describe how to implement free-space boundary conditions in a plane-wave basis. Chapter III focuses on the application of TDDFT on low-energy ions traveling through materials. Specifically, we calculate and discuss the stopping power of silicon for low-energy ions. In Chapter IV, the electronic response to light is investigated with TDDFT.

1.2. The Many-Body Problem

In this section, we examine the many-body formalism in more detail and describe some of the approximations that are assumed throughout this work. First, we derive a ground-state theory for the electrons from the SE, with the nuclei either at equilibrium or in motion as classical particles. Then, we derive a coupled set of dynamical equations for the electrons and the nuclei (where the nuclei are treated as classical particles) from the TDSE. The formalism follows the derivations given in several excellent reviews [3-5].

1.2.1. The time-independent many-electron problem

We start with the time-independent many-body problem, eq. (1.2), where the total wavefunction is a function of the electronic and nuclear coordinates,

$$\Psi_{tot} = \Psi_{tot}\left(\{\mathbf{r}_i\},\{\mathbf{R}_I\}\right) \ . \tag{1.4}$$

We invoke the usual Born-Oppenheimer Ansatz,

$$\Psi_{tot} = \Psi^{el}_{\{\mathbf{R}_I\}}\left(\{\mathbf{r}_i\}\right)\ \Phi\left(\{\mathbf{R}_I\}\right), \tag{1.5}$$

where the electronic wavefunction $\Psi^{el}_{\{\mathbf{R}_I\}}\left(\{\mathbf{r}_i\}\right)$ is a function of the electronic degrees of freedom but depends *parametrically* on the nuclear coordinates (no derivatives with respect to $\mathbf{R}$ are to be taken). Similarly, the nuclear wavefunction $\Phi\left(\{\mathbf{R}_I\}\right)$ is a function of only the nuclear degrees of freedom.

Using eq. (1.5) in eq. (1.2) gives

$$\begin{gathered} \hat{H}_e \Psi^{el}_{\{\mathbf{R}_I\}} = \varepsilon_{el} \Psi^{el}_{\{\mathbf{R}_I\}} \\ \left(-\sum_I \frac{1}{2M_I}\nabla_I^2 + \hat{H}_e\right)\Phi = \varepsilon_{tot}\Phi, \end{gathered} \tag{1.6}$$

where ε_{el} are the electronic eigenvalues, ε_{tot} are the eigenvalues of the entire sysem and

$$\hat{H}_e \equiv -\frac{\hbar^2}{2m_e}\sum_i \nabla_i^2 + \sum_{i<j}\frac{e^2}{\left|\mathbf{r}_i - \mathbf{r}_j\right|} - \sum_{I,i}\frac{e^2 Z_I}{\left|\mathbf{r}_i - \mathbf{R}_I\right|} + \sum_{I,J}\frac{e^2 Z_I Z_J}{\left|\mathbf{R}_I - \mathbf{R}_J\right|}. \tag{1.7}$$

Note that the last term in this Hamiltonian affects the electrons by shifting the eigenvalues by a constant energy.

When the nuclei are in an equilibrium configuration, e.g., a perfect crystal lattice, the equation for the nuclear wave function can be used to derive harmonic vibrations (e.g., phonons in crystals) by expanding the "potential energy" to second order in **R**. Alternatively, the nuclei can be treated as classical particles described by the corresponding classical Hamiltonian. The net result is the pair of equations

$$\begin{aligned} &\hat{H}_e(t)\Psi_{el}(t) = \varepsilon\Psi_{el}(t) \\ &M_I\ddot{\mathbf{R}}_I = -\nabla_I\left\langle \Psi_{el}\middle|\hat{H}_e\middle|\Psi_{el}\right\rangle. \end{aligned} \tag{1.8}$$

The force term in the classical equation of motion for the nuclei in (1.8) is derived using the Hellman-Feynmann theorem [6].

The set of equations given by (1.8) provides a method to evolve a system of electrons and nuclei assuming the electrons are always in their *instantaneous* ground state. It is known by a number of different names including Born-Oppenheimer Molecular Dynamics (BOMD) and adiabatic molecular dynamics. When the ground state of the electrons is calculated using DFT, the approach is known as Car-Parinello Molecular Dynamics [2]

1.2.2. The time-dependent many-electron problem

Applying the Born-Oppenheimer approximation to the time-dependent many-body problem, eq. 1.1., one obtains the following set of coupled dynamical equations [7, 8]:

$$\begin{aligned} i\hbar\frac{\partial}{\partial t}\Psi_{el} &= \left(-\frac{\hbar^2}{2m_e}\sum_i \nabla_i^2 + \left\langle \Phi \middle| \hat{V} \middle| \Phi \right\rangle\right)\Psi_{el} \\ i\hbar\frac{\partial}{\partial t}\Phi &= \left(-\sum_I \frac{\hbar^2}{2M_I}\nabla_I^2 + \left\langle \Psi_{el} \middle| \hat{H}_e \middle| \Psi_{el} \right\rangle\right)\Phi, \end{aligned} \tag{1.9}$$

where $\hat{V}$ is defined as the sum of the coulomb interaction terms in the Hamiltonian,

$$\hat{V} \equiv \sum_{i<j}\frac{1}{\left|\mathbf{r}_i - \mathbf{r}_j\right|} - \sum_{I,i}\frac{Z_I}{\left|\mathbf{r}_i - \mathbf{R}_I\right|} + \sum_{I,J}\frac{Z_I Z_J}{\left|\mathbf{R}_I - \mathbf{R}_J\right|}. \tag{1.10}$$

Following the spirit of the previous section, the nuclei are treated as classical point charges,

$$\begin{aligned} i\hbar\frac{\partial}{\partial t}\Psi_{el}(t) &= \hat{H}_e(t)\Psi_{el}(t) \\ M_I\ddot{\mathbf{R}}_I &= -\nabla_I\left\langle \Psi_{el} \middle| \hat{H}_e \middle| \Psi_{el} \right\rangle. \end{aligned} \tag{1.11}$$

Here the electrons propagate by integrating the TDSE where the Hamiltonian depends parametrically on the positions of the nuclei while at the same time the nuclei propagate by integrating the classical equation of motions with the forces depending on the Hamiltonian. This method is sometimes referred to as “Ehrenfest Molecular Dynamics” since it was Ehrenfest who first suggested this coupling of a classical description of the nuclei with a quantum mechanical treatment of the electrons [9].

In the next remainder of this section, we describe briefly the major methods that have been employed for the many-electron problem: the Hartree-Fock (HF) approximation, Post-Hartree-Fock methods, and DFT (including TDDFT).

1.3. Formulations of the many-electron problem

1.3.1. Hartree-Fock

The Hartree-Fock (HF) method can be used to find approximate solutions to the SE (see e.g. [10,11] for reviews of the HF method). One assumes that the electronic wavefunction is a Slater determinant of one-electron orbitals

$$\Psi_{el}\left(\{\mathbf{r}_i\}\right) \cong \frac{1}{\sqrt{N!}} \begin{vmatrix} \psi_1(\mathbf{r}_1) & \psi_1(\mathbf{r}_2) & \cdots & \psi_1(\mathbf{r}_N) \\ \psi_2(\mathbf{r}_1) & \psi_2(\mathbf{r}_2) & & \\ \vdots & & \ddots & \\ \psi_N(\mathbf{r}_1) & & & \psi_N(\mathbf{r}_N) \end{vmatrix}. \tag{1.12}$$

This form of the wavefunction automatically satisfies the anti-symmetry property of fermions. The one-electron orbitals are assumed to be orthonormal, $\left\langle \psi_i \middle| \psi_j \right\rangle = \delta_{ij}$.

The next step is to construct an expression for the total energy in terms of the one-electron orbitals (see [10] for a detailed derivation).

$$\begin{aligned} E_{HF} \equiv \sum_i \left\langle \psi_i \middle| \hat{h}_i \middle| \psi_i \right\rangle &+ \frac{1}{2}\sum_{i,j}\int d\mathbf{r}_1 d\mathbf{r}_2 \frac{\psi_i^*(\mathbf{r}_1)\psi_i(\mathbf{r}_1)\psi_j^*(\mathbf{r}_2)\psi_j(\mathbf{r}_2)}{|\mathbf{r}_1-\mathbf{r}_2|} \\ &- \frac{1}{2}\sum_{i,j}\int d\mathbf{r}_1 d\mathbf{r}_2 \frac{\psi_i^*(\mathbf{r}_1)\psi_j(\mathbf{r}_1)\psi_j^*(\mathbf{r}_2)\psi_i(\mathbf{r}_2)}{|\mathbf{r}_1-\mathbf{r}_2|} + E_{nn}\,. \end{aligned} \tag{1.13}$$

Note that we have adopted atomic units $\hbar = e = 1$, which we will assume unless otherwise stated throughout the rest of this thesis. In the first term of eq. (1.13),

$$\hat{h}_i \equiv -\frac{1}{2}\nabla_i^2 + \sum_I \frac{Z_I}{|\mathbf{r}_i - \mathbf{R}_I|}\,. \tag{1.14}$$

The second and third terms in (1.13) are the Hartree and exchange energies. The last term is the Coulomb repulsion energy of the nuclei.

Since the energy is minimized when the system is in the ground state, $\frac{\delta E_{HF}}{\delta \psi_i} = 0$, we can apply the variational theorem to obtain a set of coupled eigenvalue equations to solve for the one-electron orbitals

$$\hat{F}\psi_i = \varepsilon_i \psi_i . \tag{1.15}$$

The Fock operator, $\hat{F}$, is defined as

$$\hat{F} \equiv \hat{h} + \sum_j \hat{J}_j - \hat{K}_j . \tag{1.16}$$

The Hartree and exchange operators are given by

$$\begin{aligned} \hat{J}_j &\equiv \int d\mathbf{r}' \frac{\psi_j^*(\mathbf{r}')\psi_j(\mathbf{r}')}{|\mathbf{r}'-\mathbf{r}|} \\ \hat{K}_j\psi_i &\equiv \left(\int d\mathbf{r}' \frac{\psi_j^*(\mathbf{r}')\psi_i(\mathbf{r}')}{|\mathbf{r}'-\mathbf{r}|} \right)\psi_j . \end{aligned} \tag{1.17}$$

The HF approximation does not account for contributions to the total energy due to correlation effects beyond exchange. The absence of such correlation effects is often the largest source of error for many systems of interest [10].

1.3.2. Post-Hartree-Fock

Once it was recognized that the lack of correlation was responsible for much of the error in HF calculations, formulations for incorporating correlation effects were developed. These methods are collectively referred to as “Post-Hartree-Fock” and include Configuration Interaction (CI), Coupled Cluster (CC), and Møller-Plesset perturbation theory (MP2, MP3, etc. . .) to name a few [12]. They incorporate correlation effects by expanding the wavefunction to include more terms than just those from a single Slater determinant. Many of the Post-Hartree-Fock methods provide excellent agreement with experiment but are more computationally demanding due to the larger basis. These methods have been applied mostly to atoms and molecules.

1.3.3. Density-Functional Theory

Ground-state Theory

Ground-state DFT was formulated in the 1960's in two papers by Hohenberg and Kohn [13] and by Kohn and Sham [14]. A precursor to this theory is the Thomas-Fermi model of the atom that goes back to the 1920's. Because of its historical significance, we first summarize the Thomas-Fermi model.

Thomas-Fermi Model

Thomas [15] and Fermi [16] wrote the total energy of the many-electron system of an atom as the sum of four terms

$$E = T + E_{nn} + E_{ne} + E_{ee}. \tag{1.18}$$

For the kinetic energy of the electrons, T, they adopted the expression for the homogeneous electron gas, allowing the density to be a function of position:

$$T = \frac{3}{10}\left(3\pi^2\right)^{2/3} \int d\mathbf{r}\, n^{5/3}(\mathbf{r}). \tag{1.19}$$

E_{ne} is the electron-nucleus Coulomb energy given by

$$E_{ne} = -\sum_I Z_I \int d\mathbf{r} \frac{n(\mathbf{r})}{|\mathbf{R}_I - \mathbf{r}|} \tag{1.20}$$

and E_{nn} is the corresponding nucleus-nucleus Coulomb energy. Finally, E_{ee} is the electron-electron Coulomb energy

$$E_{ee} = \tfrac{1}{2}\iint d\mathbf{r}\, d\mathbf{r}' \, \frac{n(\mathbf{r})\, n(\mathbf{r}')}{|\mathbf{r}-\mathbf{r}'|} . \tag{1.21}$$

This term later became known as the Hartree energy, E_H . According to the variational principle, the ground-state density minimizes the energy functional given in (1.18). One then sets

$$\frac{\delta E}{\delta n} = \tfrac{1}{2}\left(3\pi^2 n\right)^{2/3} - \sum_i \frac{Z_i}{|\mathbf{R}_i - \mathbf{r}|} + \int d\mathbf{r}' \, \frac{n(\mathbf{r}')}{|\mathbf{r}-\mathbf{r}'|} = 0 , \tag{1.22}$$

which, constrained by

$$N = \int d\mathbf{r} \, n(\mathbf{r}) , \tag{1.23}$$

is solved for the ground-state density. Thomas and Fermi used this method to calculate the binding energy of atoms. The original formulation of the TF method does not account for the anti-symmetric behavior of the electrons (i.e. the exchange energy). Dirac extended TF theory to include an approximation to the exchange energy of an electron gas with uniform density [17]

$$E_x^{unif} = \frac{4}{3}\left(\frac{3}{\pi}\right)^{1/3} \int d\mathbf{r} \, n^{4/3}(\mathbf{r}) . \tag{1.24}$$

The exchange term raised the binding energy bringing it closer to the observed values. In 1943, Gombas introduced an additional term to include correlation effects which also raised the binding energy [18].

<u>Hohenberg-Kohn Theorems</u>

In 1964, Hohenberg and Kohn [13] proved two seemingly simple but powerful theorems that formed the foundation of ground-stae DFT. By proving that the density alone can determine the ground-state properties of a system, Hohenberg and Kohn provided an exact formalism without the need for Schrödinger many-body wavefunction. The Hohenberg-Kohn theorems along with the proofs are given below:

Theorem 1: *The external potential* $\upsilon(\mathbf{r})$ *is a unique functional of the density,* $n(\mathbf{r})$ *apart from a trivial additive constant.*

Proof: The proof relies on the minimum energy principle. Consider two external potentials that differ by more than additive constant, υ and υ'. The Hamiltonians corresponding to υ and υ' are $\hat{H}$ and $\hat{H}'$ respectively. Let the ground-state wavefunctions, Ψ and Ψ' correspond to $\hat{H}$ and $\hat{H}'$ respectively. According to the minimum energy principle (i.e. variational method), for any Hamiltonian the energy is minimized by the ground-state wavefunction,

$$E_0 = \left\langle \Psi \middle| \hat{H} \middle| \Psi \right\rangle < \left\langle \Psi' \middle| \hat{H} \middle| \Psi' \right\rangle, \tag{1.25}$$

$$E_0' = \left\langle \Psi' \middle| \hat{H}' \middle| \Psi' \right\rangle < \left\langle \Psi \middle| \hat{H}' \middle| \Psi \right\rangle. \tag{1.26}$$

If we let $\hat{H} = \hat{H}' + (\hat{H} - \hat{H}')$ and $\hat{H}' = \hat{H} - (\hat{H} - \hat{H}')$ then (1.25) and (1.26) become

$$E_0 < \left\langle \Psi' \middle| \hat{H}' \middle| \Psi' \right\rangle + \left\langle \Psi' \middle| \Delta\hat{H} \middle| \Psi' \right\rangle = E_0' + \left\langle \Psi' \middle| \Delta\hat{H} \middle| \Psi' \right\rangle, \tag{1.27}$$

$$E_0' < \left\langle \Psi \middle| \hat{H} \middle| \Psi \right\rangle - \left\langle \Psi \middle| \Delta\hat{H} \middle| \Psi \right\rangle = E_0 - \left\langle \Psi \middle| \Delta\hat{H} \middle| \Psi \right\rangle, \tag{1.28}$$

where $\Delta\hat{H} \equiv \hat{H} - \hat{H}'$. If υ and υ' were to return the same density, $n(\mathbf{r})$, then the expectation values of $\Delta\hat{H} = \upsilon - \upsilon'$ for both Ψ and Ψ' are

$$\left\langle \Psi' \middle| \Delta\hat{H} \middle| \Psi' \right\rangle = \left\langle \Psi \middle| \Delta\hat{H} \middle| \Psi \right\rangle = \int n(\mathbf{r}) \left[\upsilon(\mathbf{r}) - \upsilon'(\mathbf{r}) \right] d\mathbf{r}. \tag{1.29}$$

Substituting (1.29) into (1.27) and (1.28) and adding the two inequalities yields

$$E_0 + E_0' < E_0 + E_0'. \tag{1.30}$$

Since (1.30) is not possible, it follows that two external potentials differing by more than an additive constant cannot map to the same density. In other words, there is a unique one-to-one mapping between the density and the external potential. Since the external potential determines the Hamiltonian, the density uniquely determines the Hamiltonian as well. Moreover, according to Hohenberg and Kohn,

> Thus $\upsilon(\mathbf{r})$ is (to within a constant) a unique functional of $n(\mathbf{r})$; since, in turn, $\upsilon(\mathbf{r})$ fixes $\hat{H}$ we see that the full many-particle ground state is a unique functional of $n(\mathbf{r})$. [13]

Thus the ground-state wavefunction, Ψ, is a functional of the density, *n*.

Theorem 2: *There exists some functional of density,* $E_\upsilon[n]$, *that assumes its minimum value for the correct* $n(\mathbf{r})$.

Proof: The Hamiltonian for a system of electrons subject to an external potential $\upsilon(\mathbf{r})$ is

$$\hat{H} = \hat{T} + \hat{V}_{ee} + \hat{V}_{ext} . \tag{1.31}$$

$\hat{T}$ is the kinetic energy operator, $\hat{V}_{ee}$ is the electron-electron interaction operator, and $\hat{V}_{ext}$ is the external potential operator, which is related to the external potential function by the following equation

$$\left\langle \Psi \middle| \hat{V}_{ext} \middle| \Psi \right\rangle = \int \upsilon(\mathbf{r})\, n(\mathbf{r})\, d\mathbf{r} . \tag{1.32}$$

The total energy is the expectation value of this Hamiltonian

$$E = \left\langle \Psi \middle| \hat{T} + \hat{V}_{ee} + \hat{V}_{ext} \middle| \Psi \right\rangle . \tag{1.33}$$

Substituting (1.32) into (1.33) gives

$$E = \left\langle \Psi \middle| \hat{T} + \hat{V}_{ee} \middle| \Psi \right\rangle + \int \upsilon(\mathbf{r})\, n(\mathbf{r})\, d\mathbf{r} . \tag{1.34}$$

One can then define a universal energy functional,

$$F[n] = \left\langle \Psi \middle| \hat{T} + \hat{V}_{ee} \middle| \Psi \right\rangle . \tag{1.35}$$

Note that F is independent of the external potential, υ, and is a functional of the density because Ψ is a functional of the density (as shown in Theorem 1). The total energy of a system of electrons subject to an external potential, $\upsilon(\mathbf{r})$, can, therefore, be written as

$$E_{\upsilon}[n] = \int \upsilon(\mathbf{r}) n(\mathbf{r}) d\mathbf{r} + F[n] . \tag{1.36}$$

The variational principle is once again employed to prove the second Hohenberg-Kohn theorem. Consider two different densities: n is the density of the ground state for a potential υ and n' is the density for the potential υ'. Since Ψ is a functional of n and Ψ' is a functional of n', the following inequality holds

$$E_{\upsilon}[\Psi] = \langle \Psi | \upsilon | \Psi \rangle + \langle \Psi | T + V_{ee} | \Psi \rangle < \langle \Psi' | \upsilon | \Psi' \rangle + \langle \Psi' | T + V_{ee} | \Psi' \rangle = E_{\upsilon}[\Psi'] . \tag{1.37}$$

If $E_{\upsilon}[\Psi] < E_{\upsilon}[\Psi']$, then since Ψ is a functional of n, then $E_{\upsilon}[n] < E_{\upsilon}[n']$ Thus it has been shown that the density corresponding to the exact many-body ground-state wave-function of the system minimizes the total energy.

Despite the simplicity of the derivations, the implication of these two theorems is impressive. According to Hohenberg and Kohn,

> If $F[n]$ were a known and relatively simple functional of n, the problem of determining the ground-state energy and density in a given external potential would be rather easy since it requires merely the minimization of a functional of the three-dimensional density function. The major part of the complexities of the many-electron problems are associated with the determination of the universal functional $F[n]$. [13]

Kohn-Sham Method

In 1965, Kohn and Sham [14] developed a method to make DFT calculations to a high degree of accuracy. First, they defined a non-interacting one-electron wavefunction (Kohn-Sham wavefunction) from which the kinetic energy could be calculated. Then they defined the total energy of the system as a functional of the density (parameterized by the nuclear positions and charges). Finally, they applied the variational theorem to derive a set of equations to solve for the ground-state density and energy.

The Kohn-Sham method provides the ability to calculate the kinetic energy with greater accuracy. Kohn and Sham recognized that it is not possible to obtain an explicit expression for $T[n]$ as a functional of n because the Schrödinger many-electron wavefunction, Ψ, does not commute with the kinetic energy operator

$$T = \left\langle \Psi \left| \sum_{i=1}^{N} -\tfrac{1}{2}\nabla_i^2 \right| \Psi \right\rangle \neq -\tfrac{1}{2}\sum_{i=1}^{N} \int \nabla^2 n(\mathbf{r}_1, \mathbf{r}_2, \ldots \mathbf{r}_N)\, d\mathbf{r}_1 d\mathbf{r}_2 \ldots d\mathbf{r}_N\ . \tag{1.38}$$

Kohn and Sham invented a very clever (yet rigorous) technique to avoid this problem. They introduced a fictitious wavefunction that corresponds to non-interacting electrons. Following the Hartree-Fock convention, the Kohn-Sham total wavefunction Ψ_{KS} is defined to be a Slater determinant of orthonormal non-interacting one-electron orbitals,

$$\Psi_{KS}(\{\mathbf{r}_i\}) \cong \frac{1}{\sqrt{N!}} \begin{vmatrix} \psi_1(\mathbf{r}_1) & \psi_1(\mathbf{r}_2) & \cdots & \psi_1(\mathbf{r}_N) \\ \psi_2(\mathbf{r}_1) & \psi_2(\mathbf{r}_2) & & \\ \vdots & & \ddots & \\ \psi_N(\mathbf{r}_1) & & & \psi_N(\mathbf{r}_N) \end{vmatrix}, \tag{1.39}$$

where ψ_i are one-electron wavefunctions. Assuming no spin dependence, the total density $n(\mathbf{r})$ is a function of the three spatial degrees of freedom. Note that Ψ_{KS} as given in

(1.39) is a function of *3N* degrees of freedom. The density operator in the Kohn-Sham approach is the same as for the Schödinger approach:

$$\hat{n} = \sum_i \delta(\mathbf{r} - \mathbf{r}_i) . \tag{1.40}$$

Applying the density operator to the Kohn-Sham wavefunction yields a familiar expression for the electron density

$$n(\mathbf{r}) = \sum_{i=1}^{N} \left\langle \Psi_{KS} \left| \delta(\mathbf{r} - \mathbf{r}_i) \right| \Psi_{KS} \right\rangle = \sum_{i=1}^{N} \left| \psi_i(\mathbf{r}) \right|^2 . \tag{1.41}$$

Similarly, taking the expectation value of the kinetic energy operator yields the total Kohn-Sham kinetic energy T_{KS}

$$T_{KS} = \sum_{i=1}^{N} \left\langle \Psi_{ks} \left| -\tfrac{1}{2} \nabla_i^2 \right| \Psi_{ks} \right\rangle = \sum_{i=1}^{N} \left\langle \psi_i \left| -\tfrac{1}{2} \nabla^2 \right| \psi_i \right\rangle . \tag{1.42}$$

Note that this expression for the kinetic energy is a functional of the density because the ψ_i are functionals of the density as shown below.

One can then define an exact form of the universal functional and write the total energy as follows:

$$E_{KS} = T_{KS} + E_H + E_{ext} + E_{xcT} . \tag{1.43}$$

T_{KS} is the kinetic energy (1.42), E_H is the Hartree energy (1.21), and E_{xcT} is whatever is left over, namely exchange, correlations beyond exchange, and the difference between the kinetic energy of the real electrons and the KS expression T_{KS}.. Usually the error in the kinetic energy is ignored and only the exchange and correlation effects are included, i.e., $E_{xcT} \approx E_{xc}$.

Next, we apply the variational principle to (1.43) subject to the normalizarion constraint (1.23) to obtain an eigenvalue equation for the quasi-particles (see e.g. [19] for a more detailed description). The result is a Schrödinger-like equation

$$\left(-\tfrac{1}{2}\nabla^2 + \upsilon_{eff}\right)\psi_i = \varepsilon_i \psi_i , \tag{1.44}$$

where υ_{eff} is an effective potential through which the quasi-particles interact. It is a mean-field approximation, with the effective potential defined by

$$\upsilon_{eff}\left(\mathbf{r}\right) \equiv \upsilon_{ext}\left(\mathbf{r}\right) + \int \frac{n\left(\mathbf{r}'\right)}{\left|\mathbf{r}-\mathbf{r}'\right|} d\mathbf{r}' + \upsilon_{xc}\left(\mathbf{r}\right), \tag{1.45}$$

where each of the terms corresponds to a term in the expression for the total energy (1.43). The last term, υ_{xc}, is the functional derivative of the exchange-correlation energy E_{xc} , i.e.,

$$\upsilon_{xc} = \frac{\delta E_{xc}}{\delta n} . \tag{1.46}$$

Given υ_{eff}, the wavefunctions are found by solving (1.44). Equations (1.41), (1.44), (1.45) and (1.46) are collectively referred to as the Kohn-Sham Equations.

Note that (1.43) is the total energy of the electronic system. For a system of nuclei and electrons, the total energy would also include the kinetic and Coulomb interaction energy of the nuclei. However, since the electronic wavefunction does not depend explicitly on the nuclear coordinates, neither the eigenstates nor the eigenvalues depend on either the kinetic or Coulomb interaction energy of the nuclei (aside from a constant shift in the eigenvalues).

To solve for the ground-state density corresponding to a given external potential υ_{ext}, an initial guess for the density n_{init} is made and then one iterates around the Kohn-Sham self-consistent loop until convergence. The process is illustrated in Figure 1.1.

The Kohn-Sham wavefunctions and energy eigenvalues correspond to a system of non-interacting particles and are not guaranteed to have any physical significance. Nevertheless, it is not surprising that using the ∇^2 operator to find the kinetic energy yields a much better approximation than the $n^{5/3}$ form in the Thomas-Fermi Model.

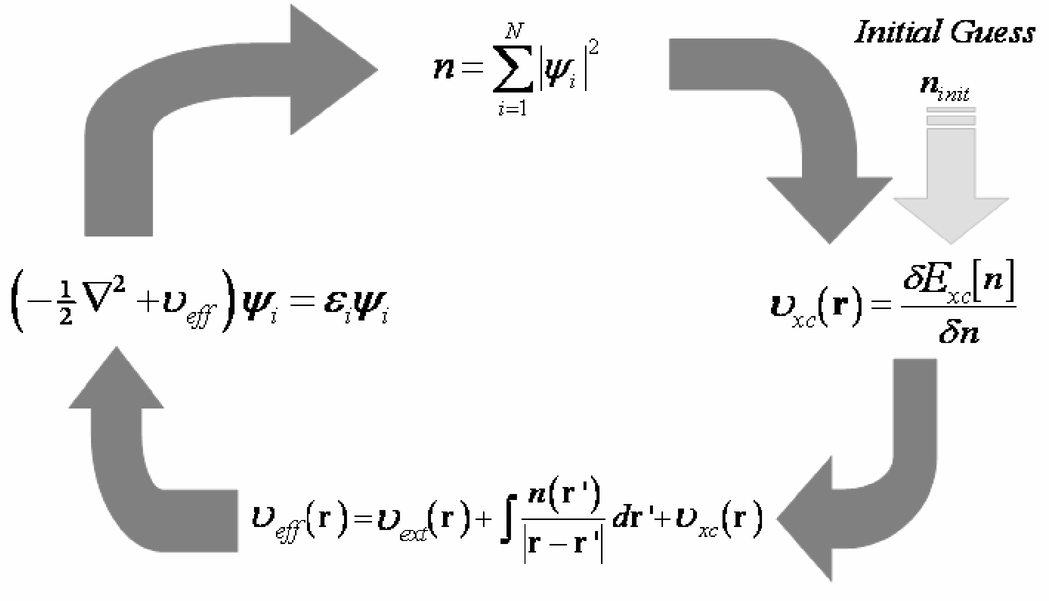

Figure 1.1: Kohn-Sham Loop

Car-Parinello Dynamics

In 1985, Car and Parrinello [2] introduced a method to efficiently include molecular dynamics (i.e. the motion of the nuclei) in a density-functional calculation. In a Car-Parrinello Molecular Dynamics calculation, one starts with a self-consistent ground state for the electrons. A Lagrangian formalism is then employed to derive equations of motion to propagate the electrons using a fictitious mass instead of finding the ground-state wavefunctions at each time step. Car and Parrinello described their method as a “dynamical simulated annealing” for the electrons [2]. The method as they introduced it is not currently in wide use because the cost of performing ground-state calculations was significantly reduced with the introduction of several numerical methods such as nonlocal pseudopotentials, iterative eigensolvers, and pre-conditioning techniques [20,21]. Nevertheless, CPMD is the first practical DFT-based implementation of BOMD.

Time-Dependent Density Functional Theory

DFT as described above is a time-independent theory. The HK theorems are formally valid only for static external potentials. Since the Kohn-Sham eigenvalue equation looks very much like the one-electron SE in an effective potential, several groups extended DFT to treat time-dependent systems by introducing a Time-Dependent Kohn-Sham (TDKS) equation analogous to the one-electron TDSE. The first attempts were successful only for specific types of time-dependent potentials. Deb and Ghosh [22] and Bartolotti [23] proved that TDDFT is valid for external perturbations that vary periodically in time. Peuckert [24] and Chakravarty et al [25] were able to show that TDDFT is a valid quantum mechanical method for small time-dependent adiabatic perturbations. Zangwill and Soven described a method that extends Kohn-Sham DFT to calculate photoabsorption spectra of rare gases [26].

In 1984, 20 years after the HK theorems were published for static DFT, Runge and Gross [27] reported a set of four theorems proving that TDDFT is formally valid for any time-dependent potential that can be expanded in a Taylor series.

According to Runge and Gross, it took two decades to extend the static DFT theorems to the time-dependent case because

> The difficulty for td (time-dependent) systems arises from the fact that no minimum principle is available; the action integral
>
> $$A = \int_{t_0}^{t_1} dt \left\langle \Psi(t) \middle| i\frac{\partial}{\partial t} - \hat{H}(t) \middle| \Psi(t) \right\rangle \tag{1.47}$$
>
> provides only a stationary point (but, in general, no minimum) at the solution of the td SE. [27]

Hohenberg and Kohn, on the other hand, were able to take advantage of the fact that the action is minimized (not just stationary) at the ground state.

The proofs for the Runge-Gross theorems are based on the Schrödinger formalism which is outlined below. The time-dependent Schrödinger equation is given by

$$i\frac{\partial}{\partial t}\Psi(t) = \hat{H}(t)\Psi(t). \tag{1.48}$$

The time-dependent Hamiltonian is the sum of three terms

$$\hat{H}(t) = \hat{T} + \hat{V}_{ee} + \hat{V}_{ext}(t), \tag{1.49}$$

where $\hat{T}$ is the kinetic energy operator, $\hat{V}_{ee}$ is the electron-electron interaction operator, and $\hat{V}_{ext}(t)$ is operator corresponding to the external time-dependent potential $v(\mathbf{r}t)$. Note that the external potential is the only term that depends explicitly on time. The density operator has already been defined in (1.40). To find the time-dependent density, apply the density operator to the time-dependent wavefunctions

$$n(\mathbf{r}t) = \langle \Psi(t) | \, \hat{n} \, | \Psi(t) \rangle. \tag{1.50}$$

The current density operator is given by

$$\hat{\mathbf{j}} = \frac{1}{2i}\sum_k \left[\vec{\nabla}_k \delta(\mathbf{r}-\mathbf{r}_k) + \delta(\mathbf{r}-\mathbf{r}_k)\vec{\nabla}_k \right]. \tag{1.51}$$

Runge-Gross Theorems

The Runge and Gross theorems are organized in two parts. The first part (consisting of the first theorem) proves the validity of using the particle and current densities as fundamental quantities in an exact quantum mechanical treatment of time-dependent systems. The second part (the last three theorems) consists of a collection of auxiliary equations that can be used in implementations of TD-DFT. The theorems are given below. Only the proof for the first theorem is shown.

Theorem 1: *For every single-particle potential $v(\mathbf{r}t)$ which can be expanded into a Taylor series with respect to the time coordinate around t = t₀, a map $G: v(\mathbf{r}t) \rightarrow n(\mathbf{r}t)$ is defined by solving the time-dependent Schrödinger equation with a fixed initial state $\Psi(t_0) = \Psi_0$ and calculating the corresponding densities $n(\mathbf{r}t)$. This map can be inverted up to an additive merely time-dependent function in the potential.*

Proof: The unique mapping between the density and the potential is proven by showing that two different time-dependent potentials, $v(\mathbf{r}t)$ and $v'(\mathbf{r}t)$, will result in different time-dependent densities, $n(\mathbf{r}t)$ and $n'(\mathbf{r}t)$. The only restrictions are that the potentials must differ by more than a time-dependent function, $v(\mathbf{r}t) - v'(\mathbf{r}t) \neq c(t)$, and that the potentials must be expandable in Taylor series. The first restriction is necessary because it can be shown that if two potentials do differ by only a time-dependent function, the corresponding time-dependent densities will be identical if the initial states are identical. The two restrictions combine to form the following necessary condition:

$$\left.\frac{d^k}{dt^k}\left[v(\mathbf{r}t) - v'(\mathbf{r}t) \right]\right|_{t=t_0} \neq constant, \tag{1.52}$$

where k is some nonnegative integer.

There are two parts to the proof. First it is shown that the current densities must be different at some infinitesimal time after the start. Second, it is shown that different current densities lead to different particle densities.

First, it will be shown that the time-dependent current densities, $\mathbf{j}(\mathbf{r}t)$ and $\mathbf{j}'(\mathbf{r}t)$, corresponding to $\upsilon(\mathbf{r}t)$ and $\upsilon'(\mathbf{r}t)$ differ at some infinitesimal time after t_0. To prove this, apply the Ehrenfest theorem [28], which can be used to find the time dependence of the expectation value of any quantum mechanical operator. Applied to the current density, the theorem gives

$$i\frac{d}{dt}\langle\mathbf{j}\rangle=\left\langle\Psi(t)\left|i\frac{\partial\hat{\mathbf{j}}}{\partial t}\right|\Psi(t)\right\rangle+\left\langle\Psi(t)\left|\left[\hat{\mathbf{j}},\hat{H}\right]\right|\Psi(t)\right\rangle. \tag{1.53}$$

The time derivative of the current density operator (1.51) is zero, whereby the above equation reduces to

$$i\frac{d}{dt}\langle\mathbf{j}\rangle=\left\langle\Psi(t)\left|\left[\hat{\mathbf{j}},\hat{H}\right]\right|\Psi(t)\right\rangle. \tag{1.54}$$

Both $\Psi(t)$ and $\Psi'(t)$ start from the same initial state

$$\Psi(0)=\Psi'(0)=\Psi_0. \tag{1.55}$$

The difference of the time derivatives of the current densities is

$$\begin{aligned}i\frac{d}{dt}\left[\langle\mathbf{j}\rangle-\langle\mathbf{j}'\rangle\right]\Big|_{t=t_0}&=\left\langle\Psi_0\left|\left[\hat{\mathbf{j}},\hat{H}-\hat{H}'\right]\right|\Psi_0\right\rangle\\&=\left\langle\Psi_0\left|\left[\hat{\mathbf{j}},\upsilon-\upsilon'\right]\right|\Psi_0\right\rangle\\&=\left\langle\Psi_0\left|\hat{\mathbf{j}}(\upsilon-\upsilon')-(\upsilon'-\upsilon)\hat{\mathbf{j}}\right|\Psi_0\right\rangle.\end{aligned} \tag{1.56}$$

Substituting $u\equiv\upsilon-\upsilon'$ into the above equation and evaluating,

$$i\frac{d}{dt}\langle[\mathbf{j}-\mathbf{j}']\rangle\Big|_{t=t_0} = \frac{1}{2i}\sum_k \left\langle \Psi_0 \right| \nabla_k\ \delta(\mathbf{r}-\mathbf{r}_k)\, u \left|\Psi_0\right\rangle + \left\langle \Psi_0 \right| \delta(\mathbf{r}-\mathbf{r}_k)\, \nabla_k\ u \left|\Psi_0\right\rangle$$
$$- \left\langle \Psi_0 \right| u \nabla_k\ \delta(\mathbf{r}-\mathbf{r}_k) \left|\Psi_0\right\rangle - \left\langle \Psi_0 \right| u\ \delta(\mathbf{r}-\mathbf{r}_k)\, \nabla_k \left|\Psi_0\right\rangle . \tag{1.57}$$

Applying the derivatives in the above equation yields

$$i\frac{d}{dt}\langle[\mathbf{j}-\mathbf{j}']\rangle\Big|_{t=t_0} = \frac{1}{2i}\sum_k \left\langle \Psi_0 \right| \left[\nabla_k \delta(\mathbf{r}-\mathbf{r}_k)\right] u \left|\Psi_0\right\rangle + 2\left\langle \Psi_0 \right| \delta(\mathbf{r}-\mathbf{r}_k)\, \nabla_k\ u \left|\Psi_0\right\rangle$$
$$- \left\langle \Psi_0 \right| u \left[\nabla_k\ \delta(\mathbf{r}-\mathbf{r}_k)\right] \left|\Psi_0\right\rangle - 2\left\langle \Psi_0 \right| u\ \delta(\mathbf{r}-\mathbf{r}_k)\, \nabla_k \left|\Psi_0\right\rangle . \tag{1.58}$$

The first and third terms cancel. Expanding the derivative in the second term

$$i\frac{d}{dt}\langle[\mathbf{j}-\mathbf{j}']\rangle\Big|_{t=t_0} = i\sum_k \left\langle \Psi_0 \right| \delta(\mathbf{r}-\mathbf{r}_k)\ (\nabla_k\ u) \left|\Psi_0\right\rangle$$
$$+ \left\langle \Psi_0 \right| \delta(\mathbf{r}-\mathbf{r}_k)\, u\, \nabla_k \left|\Psi_0\right\rangle - \left\langle \Psi_0 \right| u\ \delta(\mathbf{r}-\mathbf{r}_k)\, \nabla_k \left|\Psi_0\right\rangle . \tag{1.59}$$

The second and third terms cancel leaving

$$i\frac{d}{dt}\langle[\mathbf{j}-\mathbf{j}']\rangle\Big|_{t=t_0} = -i\sum_k \left\langle \Psi_0 \right| \delta(\mathbf{r}-\mathbf{r}_k)\ (\nabla_k\ u) \left|\Psi_0\right\rangle . \tag{1.60}$$

Finally, the delta functions collapse the integrals leaving

$$\frac{d}{dt}\langle[\mathbf{j}-\mathbf{j}']\rangle\Big|_{t=t_0} = n(\mathbf{r}t_0)\, \nabla\left[\upsilon(\mathbf{r}t_0)-\upsilon'(\mathbf{r}t_0)\right] . \tag{1.61}$$

According to the restriction given in (1.52), there must be a nonnegative integer *k* such that the k^{th} time derivative of $\upsilon(\mathbf{r}t_0)-\upsilon'(\mathbf{r}t_0)$ is not constant and therefore the gradient of this quantity is not zero. If *k* is the smallest integer for which (1.52) holds, then the following quantity must vanish for any $m<k$

$$\nabla\left[\frac{d^m}{dt^m}(\upsilon-\upsilon')\right]=0 \qquad for \quad m<k\ . \tag{1.62}$$

Therefore, the k^{th} time derivative of (1.61) has the following form and must not vanish

$$\frac{d^{k+1}}{dt^{k+1}}\langle[\mathbf{j}-\mathbf{j}']\rangle\Big|_{t=t_0}=n(\mathbf{r}t_0)\,\nabla\left\{\frac{d^k}{dt^k}\big[\upsilon(\mathbf{r}t_0)-\upsilon'(\mathbf{r}t_0)\big]\right\}\neq 0\,. \tag{1.63}$$

Thus, the current densities will be different at some infinitesimal time after t_0.

The second part of the proof is to show that the particle densities, $n(\mathbf{r})$ and $n'(\mathbf{r})$, will be different at some infinitesimal time after t_0. The continuity equation relates the particle density to the current density:

$$\nabla\cdot\mathbf{j}+\frac{\partial n}{\partial t}=0\,. \tag{1.64}$$

Taking the divergence of both sides of (1.63) and substituting in the continuity equation yields an expression for the difference between the particle densities

$$\frac{d^{k+2}}{dt^{k+2}}\big[n(\mathbf{r}t)-n'(\mathbf{r}t)\big]\Big|_{t=t_0}=-\nabla\cdot\left\{n(\mathbf{r}t_0)\,\nabla\left(\frac{d^k}{dt^k}\big[\upsilon(\mathbf{r}t)-\upsilon'(\mathbf{r}t)\big]_{t=t_0}\right)\right\}. \tag{1.65}$$

It was shown in the first part of the proof that the quantity in curly braces in the above equation will not vanish for some nonnegative k. For any nontrivial density, it can be assumed that the spatial derivative of the quantity in curly braces will not be zero. Therefore the densities, $n(\mathbf{r}t)$ and $n'(\mathbf{r}t)$ will differ at some infinitesimal time after t_0.

The remaining three theorems provide a continuity equation (with a definition of a current density), a formal definition of the exchange-correlation potential and an expression for the time-dependent density. These three theorems are listed for completeness.

Theorem 2: *There exists a three-component density functional* $\mathbf{P}[n](\mathbf{r}t)$ *which depends parametrically on* $(\mathbf{r}t)$ *such that the exact particle and current densities can be determined from a set of "hydrodynamical" equations*

$$\partial_t n(\mathbf{r}t)+\nabla\cdot\mathbf{j}(\mathbf{r}t)=0 \tag{1.66}$$

$$\partial_t \mathbf{j}(\mathbf{r}t) = \mathbf{P}[n](\mathbf{r}t) \tag{1.67}$$

with initial conditions

$$n(\mathbf{r}t_0) = \left\langle \Psi_0 \middle| \hat{n}(\mathbf{r}) \middle| \Psi_0 \right\rangle \tag{1.68}$$

and

$$\mathbf{j}(\mathbf{r}t_0) = \left\langle \Psi_0 \middle| \hat{\mathbf{j}}(\mathbf{r}) \middle| \Psi_0 \right\rangle . \tag{1.69}$$

Theorem 3: *The action integral (1.47) can be represented as a functional of the density* $A[n]$. *If the potential* $\upsilon(\mathbf{r}t)$ *is chosen such that no additive time-dependent function can be split, the total action can be written as*

$$A[n] = B[n] - \int_{t_0}^{t_1} dt \int d\mathbf{r}\; n(\mathbf{r}t)\, \upsilon(\mathbf{r}t), \tag{1.70}$$

where $B[n]$ *is a* ***universal*** *functional of the density in the sense that the same dependence on* $n(\mathbf{r}t)$ *holds for all external potentials* $\upsilon(\mathbf{r}t)$. $A[n]$ *has a stationary point at the exact density of the system, i.e., the exact density can be computed from the Euler equation*

$$\frac{\delta A}{\delta n} = 0. \tag{1.71}$$

Theorem 4: *The exact time-dependent density of the system can be computed from*

$$n(\mathbf{r}t) = \sum_j \phi_j^*(\mathbf{r}t)\, \phi_j(\mathbf{r}t), \tag{1.72}$$

where the single-particle orbitals $\phi_j(\mathbf{r}t)$ *fulfill the time-dependent Schrödinger equation*

$$\left(i\partial_t + \tfrac{1}{2}\nabla^2\right)\phi_j(\mathbf{r}t) = \upsilon_{eff}\left[\mathbf{r}t; n(\mathbf{r}t)\right]\phi_j(\mathbf{r}t) \tag{1.73}$$

with an effective one-particle potential given by

$$v_{eff}\left[\mathbf{r}t;n(\mathbf{r}t)\right]=v(\mathbf{r}t)+\int d\mathbf{r}'\frac{n(\mathbf{r}'t)}{|\mathbf{r}-\mathbf{r}'|}+\frac{\delta A_{xc}}{\delta n(\mathbf{r}t)} \tag{1.74}$$

Where A_{xc} is the exchange-correlation part of the action integral (1.47).

Linear Response

In 1980, before the Runge-Gross paper was published, Zangwill and Soven published a density-functional method to calculate the photoabsorption spectra in rare gases. This approach has become known as "Linear Response" because it involves the linearization of the TDDFT equations. In this formalism, it is assumed that the Hamiltonian consists of a static part and a relatively small time-dependent part

$$\hat{H}(t)=\hat{H}_0+\hat{H}_1(t)\,. \tag{1.75}$$

The density then evolves in time and can then be split into a static and dynamic part

$$n(\mathbf{r}t)=n_0(\mathbf{r})+n_1(\mathbf{r}t)\,, \tag{1.76}$$

where the static part of the density n_0 corresponds to v_0. The density may be calculated directly from the Kohn-Sham wavefunctions using the density operator

$$n(\mathbf{r}t)=\sum_m f_m\left\langle\psi_m(\mathbf{r}t)\middle|\delta(\mathbf{r}-\mathbf{r}')\middle|\psi_m(\mathbf{r}'t)\right\rangle, \tag{1.77}$$

where f_m is the occupation number for the m^{th} time-dependent Kohn-Sham wavefunction, $\psi_m(\mathbf{r}t)$. The time-dependent Kohn-Sham wavefunctions can be represented as

$$\begin{aligned}\psi_m(\mathbf{r}t)&=e^{-i\int_{-\infty}^{t}\hat{H}(t')dt'}\psi_m^0(\mathbf{r})=e^{-i\hat{H}_0\int_{-\infty}^{t}dt'}e^{-i\int_{-\infty}^{t}\hat{H}_1(t')dt'}\psi_m^0(\mathbf{r})=e^{-iE_mt}e^{-i\int_{-\infty}^{t}\hat{H}_1(t')dt'}\psi_m^0(\mathbf{r})\\&=\mathbf{U}(t)\psi_m^0(\mathbf{r}),\end{aligned} \tag{1.78}$$

where $\psi_m^0(\mathbf{r})$, E_m and $\hat{H}_0$, and are the ground-state wavefunctions, energy eigenvalues and static Hamiltonian that satisfy the eigenvalue equation: $\hat{H}_0\psi_m^0 = E_m\psi_m^0$. $\mathbf{U}(t)$ is the time evolution operator

$$\mathbf{U}(t) \equiv e^{-iE_m t} e^{-i\int_{-\infty}^{t} \hat{H}_1(t')dt'} . \tag{1.79}$$

Substituting (1.78) into (1.77) yields the following expression for the time-dependent density:

$$\begin{aligned} n(\mathbf{r}t) &= \sum_m f_m \left\langle \psi_m^0 \middle| \mathbf{U}^{-1}\delta(\mathbf{r}-\mathbf{r}')\mathbf{U} \middle| \psi_m^0 \right\rangle \\ &= \sum_m f_m \left\langle \psi_m^0 \middle| e^{iE_m t} e^{i\int_{-\infty}^{t} \hat{H}_1(t')dt'} \delta(\mathbf{r}-\mathbf{r}') e^{-iE_m t} e^{-i\int_{-\infty}^{t} \hat{H}_1(t')dt'} \middle| \psi_m^0 \right\rangle \\ &= \sum_m f_m \left\langle \psi_m^0 \middle| e^{i\int_{-\infty}^{t} \hat{H}_1(t')dt'} \delta(\mathbf{r}-\mathbf{r}') e^{-i\int_{-\infty}^{t} \hat{H}_1(t')dt'} \middle| \psi_m^0 \right\rangle . \end{aligned} \tag{1.80}$$

Taylor expanding the time propagation operators in the above equation keeping only the first two terms in the expansion

$$n(\mathbf{r}t) \approx \sum_m f_m \left\langle \psi_m^0 \middle| \left(1 + i\int_{-\infty}^{t} \hat{H}_1(t')dt' + \ldots \right) \delta(\mathbf{r}-\mathbf{r}') \left(1 - i\int_{-\infty}^{t} \hat{H}_1(t')dt' + \ldots \right) \middle| \psi_m^0 \right\rangle . \tag{1.81}$$

Multiply through and keep only the zeroth and first order terms in $\hat{H}_1$

$$\begin{aligned} n(\mathbf{r}t) = \sum_m f_m \Big[&\left\langle \psi_m^0 \middle| \delta(\mathbf{r}-\mathbf{r}') \middle| \psi_m^0 \right\rangle \\ &+ i\int_{-\infty}^{t} dt' \left\langle \psi_m^0 \middle| \hat{H}_1(t')\delta(\mathbf{r}-\mathbf{r}') \middle| \psi_m^0 \right\rangle - i\int_{-\infty}^{t} dt' \left\langle \psi_m^0 \middle| \delta(\mathbf{r}-\mathbf{r}')\hat{H}_1(t') \middle| \psi_m^0 \right\rangle \Big] . \end{aligned} \tag{1.82}$$

The first term is just the ground-state density and the second and third term combine to form the commutator of the Hamiltonian and the density operator.

$$n(\mathbf{r}t) = n_0(\mathbf{r}) + i\sum_m f_m \int_{-\infty}^{t} dt' \left\langle \psi_m^0 \left\| \left[\hat{H}_1(t'), \delta(\mathbf{r}-\mathbf{r}') \right] \right\| \psi_m^0 \right\rangle . \tag{1.83}$$

Note that the time ordering condition $t > t'$ (and thus causality) is explicitly enforced in the above equation (i.e. the perturbation at time t' can only affect an observable at some later time *t*). Finally, substituting (1.76) into (1.83) yields an approximate expression for the dynamic part of the density that is accurate to linear order

$$n_1(\mathbf{r}t) = i\sum_m f_m \int_{-\infty}^{t} dt' \left\langle \psi_m^0 \left\| \left[\hat{H}_1(t'), \delta(\mathbf{r}-\mathbf{r}') \right] \right\| \psi_m^0 \right\rangle . \tag{1.84}$$

If the explicitly time-dependent part of the Hamiltonian can be represented as a local potential then one may write the Hamiltonian in the following form:

$$\hat{H}_1(\mathbf{r}'t') = \int d\mathbf{r}'' \delta(\mathbf{r}'-\mathbf{r}'')\, \upsilon_1(\mathbf{r}'', t'), \tag{1.85}$$

where

$$\upsilon_1(\mathbf{r}t) = \upsilon_{ext}(\mathbf{r}t) + \upsilon_H(\mathbf{r}t) + \upsilon_{xc}(\mathbf{r}t). \tag{1.86}$$

$\upsilon_{ext}(\mathbf{r}t)$ is a small time-varying external potential. Substituting (1.85) into (1.84) leaves the following expression for the time-dependent part of the density

$$\begin{aligned} n_1(\mathbf{r}t) &= i\sum_m f_m \int_{-\infty}^{t} dt' \int d\mathbf{r}'' \left\langle \psi_m^0 \left\| \left[\delta(\mathbf{r}'-\mathbf{r}'')\upsilon_1(\mathbf{r}'',t'), \delta(\mathbf{r}-\mathbf{r}') \right] \right\| \psi_m^0 \right\rangle \\ &= i\sum_m f_m \int_{-\infty}^{t} dt' \int d\mathbf{r}'' \left\langle \psi_m^0 \left\| \left[\delta(\mathbf{r}'-\mathbf{r}''), \delta(\mathbf{r}-\mathbf{r}') \right] \right\| \psi_m^0 \right\rangle \upsilon_1(\mathbf{r}'',t'). \end{aligned} \tag{1.87}$$

Note that the time-dependent density is a linear functional of the time-dependent potential, which is the reason this method is known as “linear response”. The equation above is in a form that is comparable to the density-density correlation equation:

$$n_1(\mathbf{r}t) = \int_{-\infty}^{\infty} dt' \int d\mathbf{r}' \chi(\mathbf{r},\mathbf{r}',t-t')\, \upsilon_1(\mathbf{r}'t'). \tag{1.88}$$

From (1.87) and (1.88), an expression for the susceptibility can be found

$$\begin{aligned}\chi(\mathbf{r},\mathbf{r}',t-t') &\equiv i\theta(t-t')\sum_{m} f_m \left\langle \psi_m^0 \middle| \left[\delta(\mathbf{r}'-\mathbf{r}''),\delta(\mathbf{r}-\mathbf{r}'')\right] \middle| \psi_m^0 \right\rangle \\ &= i\theta(t-t')\sum_{m} f_m \left[\left\langle \psi_m^0 \middle| \delta(\mathbf{r}'-\mathbf{r}'')\delta(\mathbf{r}-\mathbf{r}'') \middle| \psi_m^0 \right\rangle - \left\langle \psi_m^0 \middle| \delta(\mathbf{r}-\mathbf{r}'')\delta(\mathbf{r}'-\mathbf{r}'') \middle| \psi_m^0 \right\rangle\right],\end{aligned} \tag{1.89}$$

where the Heaviside function is defined by

$$\theta(t-t') \equiv \begin{cases} 1 & ,t-t'>0 \\ 0 & ,t-t'<0\,. \end{cases} \tag{1.90}$$

Including the Heaviside function in (1.89) ensures that causality will be enforced. Assuming that the basis is complete, then the following relation holds

$$\sum_{n} \left|\psi_n^0\right\rangle\left\langle\psi_n^0\right| = \mathbf{1}\,. \tag{1.91}$$

Insert the above equation into (1.89)

$$\begin{aligned}\chi(\mathbf{r},\mathbf{r}',t-t') = i\theta(t-t')\sum_{mn} f_m \Big[&\left\langle \psi_m^0 \middle| \delta(\mathbf{r}'-\mathbf{r}'') \middle| \psi_n^0 \right\rangle \left\langle \psi_n^0 \middle| \delta(\mathbf{r}-\mathbf{r}'') \middle| \psi_m^0 \right\rangle \\ &- \left\langle \psi_m^0 \middle| \delta(\mathbf{r}-\mathbf{r}'') \middle| \psi_n^0 \right\rangle \left\langle \psi_n^0 \middle| \delta(\mathbf{r}'-\mathbf{r}'') \middle| \psi_m^0 \right\rangle\Big].\end{aligned} \tag{1.92}$$

The Dirac functions collapse the integrals in the above expression leaving

$$\begin{aligned}\chi(\mathbf{r},\mathbf{r}',t-t') &= i\theta(t-t')\sum_{mn} f_m \Big[\psi_m^{0*}(\mathbf{r}')\psi_n^0(\mathbf{r}')\psi_n^{0*}(\mathbf{r})\psi_m^0(\mathbf{r}) \\ &\qquad\qquad - \psi_m^{0*}(\mathbf{r})\psi_n^0(\mathbf{r})\psi_n^{0*}(\mathbf{r}')\psi_m^0(\mathbf{r}')\Big] \\ &= i\theta(t-t')\sum_{mn} (f_m - f_n)\psi_m^{0*}(\mathbf{r}')\psi_n^0(\mathbf{r}')\psi_n^{0*}(\mathbf{r})\psi_m^0(\mathbf{r})\,.\end{aligned} \tag{1.93}$$

Transforming to the frequency domain and writing the above expression in the Lehman level representation [29] leaves

$$\chi(\mathbf{r},\mathbf{r}',\omega) = \sum_{m,n} (f_m - f_n)\frac{\psi_m^{0*}(\mathbf{r})\psi_n^0(\mathbf{r})\psi_n^{0*}(\mathbf{r}')\psi_m^0(\mathbf{r}')}{\omega - (\omega_m - \omega_n) + i\delta}\,, \tag{1.94}$$

where $i\delta$ is a broadening term that can be attributed to finite temperature. There are poles in the density-density correlation response function at the Kohn-Sham transition energies,

$\omega_m - \omega_n$. It is known that the Kohn-Sham transition energies deviate significantly from the true transition energies when exchange and correlation effects are approximated with the local density approximation. Petersilka et al. [30] derived the following technique to find the transition true transition energies using a Kohn-Sham formalism. Substitute (1.86) into (1.88), transform to the frequency domain and express the Hartree and exchange-correlation potentials in integral form:

$$n_1(\mathbf{r}\omega) = \int d\mathbf{r}' \chi(\mathbf{r},\mathbf{r}',\omega) \left[v_{ext}(\mathbf{r}'\omega) + \int d\mathbf{r}'' \left(\frac{1}{|\mathbf{r}''-\mathbf{r}'|} + f_{xc}\left[n_0(\mathbf{r}',\mathbf{r}'',\omega)\right] \right) n_1(\mathbf{r}''\omega) \right]. \quad (1.95)$$

Move the Hartree and exchange-correlation terms to the left side of the equation and rewrite the time-dependent density in integral form, $n_1(\mathbf{r}\omega) = \int d\mathbf{r}'' \delta(\mathbf{r}-\mathbf{r}'') n_1(\mathbf{r}''\omega)$:

$$\begin{aligned} \int d\mathbf{r}'' \left[\delta(\mathbf{r}-\mathbf{r}'') - \int d\mathbf{r}' \chi(\mathbf{r},\mathbf{r}',\omega) \left(\frac{1}{|\mathbf{r}''-\mathbf{r}'|} + f_{xc}\left[n_0(\mathbf{r}',\mathbf{r}'',\omega)\right] \right) \right] n_1(\mathbf{r}''\omega) \\ = \int d\mathbf{r}' \chi(\mathbf{r},\mathbf{r}',\omega) v_{ext}(\mathbf{r}'\omega). \end{aligned} \quad (1.96)$$

Note that the poles in the exact density response, n_1, correspond to the true transition energies and therefore. Because the poles in the Kohn-Sham density-density response functions do *not* correspond to the true transition energy, the integral operator on the left side of (1.96) must vanish at the transition energies in order to satisfy the equation. Therefore the eigenvalues of this integral operator must vanish for the true transition energies satisfying the following equation

$$\int d\mathbf{r}'' \left[\delta(\mathbf{r}-\mathbf{r}'') - \int d\mathbf{r}' \chi(\mathbf{r},\mathbf{r}',\omega) \left(\frac{1}{|\mathbf{r}''-\mathbf{r}'|} + f_{xc}\left[n_0(\mathbf{r}',\mathbf{r}'',\omega)\right] \right) \right] \xi(\mathbf{r}''\omega) = 0 \quad . \quad (1.97)$$

Applying the delta operator to collapse the integral, one may rewrite (1.97) as an eigenvalue equation,

$$\int d\mathbf{r}'' \int d\mathbf{r}' \chi(\mathbf{r},\mathbf{r}',\omega) \left(\frac{1}{|\mathbf{r}''-\mathbf{r}'|} + f_{xc}\left[n_0(\mathbf{r}',\mathbf{r}'',\omega) \right] \right) \xi(\mathbf{r}''\omega) = \lambda(\omega)\, \xi(\mathbf{r}\omega), \tag{1.98}$$

where the eigenvalues satisfy $\lambda(\omega = \Omega_n) = 1$ at the true transition energies, Ω_n. Note that this method for finding the transition energies is exact to within the linear response approximation (1.84). In practice, deviations from the exact transition energy may also be due to the approximation to the time-dependent exchange-correlation kernel, $f_{xc}\left[n_0(\mathbf{r}',\mathbf{r}'',\omega) \right]$. Instead of solving for the transition energies directly from (1.98), Petersilka et al [30] suggested several additional approximations to calculate them more easily. However, Vasiliev et al [31] demonstrated that these approximations led to an appreciable deviation from the true excitation spectrum when compared to experiment and therefore one should solve for the transition energies directly from (1.98) when making quantitative predictions.

Linear response has been a successful application of TD-DFT. Several authors have applied linear response to calculate dynamic polarizabilities, hyperpolarizabilities and optical absorption spectra [32].

TDDFT+MD

Theilhaber [33] first implemented TDDFT-based molecular dynamics to study the bulk properties of sodium at finite temperature. In the TDDFT+MD approach, the system evolves by self-consistently propagating the coupled set of equations given by (1.11) where the electronic equation is cast into the TDDFT formulation. Thus, the electrons are described by Kohn-Sham wavefunctions and propagate by integrating the time-dependent Kohn-Sham equation. The details of the implementation of (1.11), as carried out in the present work, are given in the next Chapter.

Excluding external interactions, there are three quantities that are conserved in the TDDFT+MD approach [33]. First, the total number of electrons N_e is conserved:

$$N(t) = \int d\mathbf{r}\, n(\mathbf{r}) = N_e. \tag{1.99}$$

This feature is due to the orthonormality of the time propagation operator and will be discussed in more detail in the next Chapter. The total momentum of the system, namely

$$\mathbf{P} \equiv \sum_I M_I \dot{\mathbf{R}}_I(t) + \int d\mathbf{r}\, \Psi^*(-i\nabla)\Psi, \tag{1.100}$$

is also conserved. One can prove conservation of momentum by taking the time derivative of (1.100) and showing that it vanishes so long as (1.11) is satisfied. Finally, the total energy of the system, defined by

$$E_{tot} \equiv E_{instant} + E_{nuc} \tag{1.101}$$

is conserved. Here E_{nuc} is the sum of the classical kinetic energy of the nuclei and $E_{instant}$ is the energy of the system as defined by the time-*independent* density functional theory.

$$E_{instant} \equiv T_e + E_{Hxc} + E_{ne} + E_{nn} \tag{1.102}$$

Where T_e is the kinetic energy of the electrons, E_{Hxc} is the sum of the Hartree, exchange and correlation energies, E_{ne} is the electrostatic nuclear-electronic energy, and E_{nn} is the electrostatic nuclear-nuclear energy (i.e. the Ewald Energy for periodic systems). $E_{instant}$ is a functional of $n(t)$. The conservation of energy can be shown using a Lagrangian formalism [33]

The TDDFT approach has the advantage of not being restricted to the adiabatic surface in that the electrons are not restricted to be in the instantaneous ground state at each time step. Note that this approach assumes the mean field approximation for the time-dependent Hamiltonian. As a result, the electrons can interact only with classical fields. The practical implication of this restriction is that the electrons can only interact with classical electromagnetic fields – i.e. there is no prescription for quantizing light in this formulation. The electrons couple to electromagnetic fields via the scalar and vector potentials in the Hamiltonian. Moreover, there is no mechanism for treating transitions between states. The occupations of the bands at the beginning of a TDDFT run remain fixed throughout the calculation – the bands themselves are evolving in time. For example, as the occupied orbitals evolve out of their instantantaneous ground-state analogs, there is no prescription to emit a photon and transition into a lower state. Conversely, there is no mechanism to absorb a quantized photon and transition into a higher energy state. From a practical standpoint, TDDFT+MD is limited to those systems where optical transitions are negligible.

TDDFT+MD has been successfully used to study charge transfer between clusters of atoms [34,35], low-energy ion induced damage in graphene [36] and, despite the limitation discussed above, photo-assisted self-healing in carbon nanotubes [37]. In Chapter III, we apply TDDFT+MD to stopping power calculations of ions moving through various target materials.

1.4. References

[1] M. Born and R. Oppenheimer, *Ann D Phys*, **84** 457 (1927).

[2] R. Car and M. Parrinello, *Phys. Rev. Lett.* **55,** 2471 (1985).

[3] G. Galli and M. Parrinello, *Computer Simulations in Material Science,* p. 282. eds. M. Meyer and V. Pontikis (Kluwer, Dordrecht, 1991).

[4] G. Galli and A. Pasquarello *Computer Simulations in Chemical Physics,* eds M. P. Allen and D.J. Tildesley (Kluwer, Dordrecht, 1993).

[5] D. Marx and J. Hutter, *Modern Methods and Algorithms of Quantum Chemistry*, ed J. Grotendorst, NIC, Jülich, 2000.

[6] M. DiVentra and S.T. Pantelides. *Phys. Rev. B.* **61**, 16207 (2000).

[7] P.A.M. Dirac, *The Principls of Quantum Mechanics*, Oxford University Press, Oxford. 3rd ed. (1947). Chapters 31-32.

[8] A. Messiah, *Quantum Mechanics*. North-Holland Publishing Co., Amsterdam, (1964).

[9] P. Ehrenfest, *Z Phys.* **45** 455 (1927).

[10] R. McWeeny, *Methods of Molecular Quantum Mechanics*, Academic Press, London (1992).

[11] O. Madelung. *Introduction to Solid-State Theory*. Springer-Verlag, Berlin (1978).

[12] T. Helgaker, P Jorgensen, and J. Olsen, *Molecular Electronic-Structure Theory*, Wiley & Sons Ltd., West Sussex (2000).

[13] P. Hohenberg, and W. Kohn, *Phys. Rev.* **136:** B864 (1964).

[14] W. Kohn, and L. J. Sham, *Phys. Rev.* **140:** A1133 (1965).

[15] L. H. Thomas, *Proc. Camb. Phil. Soc.* **23:** 542 (1927).

[16] E. Fermi, *Z. Phys.* **48:** 73 (1928).

[17] P.A.M. Dirac, *Proc Cambridge Phil Soc*, **26**, 376 (1930).

[18] P. Gombas, *Z Physik*, **121**, 523 (1943).

[19] G. B. Arfken and H.J. Weber, *Mathematical Methods for Physicists,* Academic Press, New York (1995).

[20] L. Kleinman and D.M. Bylander, *Phys Rev Lett.* **48** 1425 (1982).

[21] R. Martin, *Electronic Structure: Basic Theory and Practical Methods*. Cambridge University Press, Cambridge, (2004).

[22] B.M. Deb and S.K. Ghosh, *J. Chem. Phys.* **77** 342 (1982).

[23] L.J. Bartolotti, *Phys. Rev. A*, **24**. 1661 (1981).

[24] V. Peuckert, *J. Phys. C.* **11**, 4945 (1978).

[25] S. Chakraverty, M.B. Fogel, and W. Kohn, *Phys. Rev. Lett.* **43**, 775 (1979).

[26] A. Zangwill and P. Soven, *Phys. Rev. A* **21,** 1561 (1980).

[27] E. Runge and E.K.U. Gross, *Phys. Rev. Lett.* **52**, 997 (1984).

[28] R. Shankar, *Principles of Quantum Mechanics*, 2nd Ed. Plenum Press. New York (1994).

[29] C. Kittel, *Quantum Theory of Solids*. Revised Printing. John Wiley & Sons, New York (1963).

[30] M. Petersilka, U.J. Grossman, and E.K.U. Gross, *Phys Rev. Lett.* **76**, 1212 (1996).

[31] I. Vasiliev, S. Öğüt, and J.R. Chelikowsky, *Phys. Rev. Lett*, **82**, 1919 (1999).

[32] K. Nuroh M.J. Stott and E. Zaremba, *Phys. Rev. Lett*. **49**, 862 (1982).

[33] J Theilhaber. *Phys. Rev. B*. **46** 12990 (1992).

[34] U. Saalmann and R. Schmidt. *Z. Phys. D.* **38** 153 (1996).

[35] U. Saalmann and R. Schmidt. *Phys. Rev. Lett.* **80** 3213 (1998).

[36] Y. Miyamoto, private communication with author.

[37] Y. Miyamoto, S. Berber, M. Yoon, A. Rubio, and D. Tománek. *Chem Phys. Lett.* **392** 209 (2004).

CHAPTER II

ALGORITHMS

2.1. Introduction

In this chapter the various algorithms that were implemented will be described. First, several techniques for expanding the time-evolution operator will be presented. After that, the technique for including freespace boundary conditions in a code with a plane-wave basis will be presented.

2.2. The Time Evolution Operator

In this section we describe and discuss several methods for expanding the formal time propagation operator. It can be shown that the solution to the TDSE (1.1) is given by

$$\Psi(t) = \mathcal{T}\ \exp\left(-i\int_{t_0}^{t} \hat{H}(t')\,dt'\right)\Psi(t_0) \tag{2.1}$$

where $\mathcal{T}$ indicates that the integral is time-ordered, i.e., the solution at some time t requires that $\Psi(t)$ is known for all prior times.. The time evolution operator from time t_0 to t_1 can be defined from (2.1)

$$\hat{U}(t_0,t_1) \equiv \mathcal{T}\ \exp\left(-i\int_{t_0}^{t_1} \hat{H}(t)\,dt\right) \tag{2.2}$$

The time evolution operator has several important properties. First, since the Hamiltonian is Hermitian, the time evolution operator is unitary, i.e.,

$$\hat{U}^{\dagger}\hat{U} = \hat{U}\hat{U}^{\dagger} = \mathbf{1} \tag{2.3}$$

or, equivalently,

$$\hat{U}^{\dagger} = \hat{U}^{-1}. \tag{2.4}$$

Second, the time evolution operator is symmetric in time, satisfying

$$\hat{U}^{-1}(t_1, t_0) = \hat{U}(t_0, t_1) \tag{2.5}$$

Third, it satisfies

$$\hat{U}(t_0, t_2) = \hat{U}(t_1, t_2)\hat{U}(t_0, t_1), \tag{2.6}$$

where $t_0 < t_1 < t_2$. This last property suggests an alternative description of the formal time evolution operator. It is possible to write the time-ordered integral as an infinite product of exponentials.

$$\begin{aligned}\hat{U}(t_0, t_1) &= \hat{U}(t_1 - \Delta, t_1)\hat{U}(t_1 - 2\Delta, t_1 - \Delta)\ldots\hat{U}(t_0 + \Delta, t_0 + 2\Delta)\hat{U}(t_0, t_0 + \Delta) \\ &= \lim_{\substack{\Delta\to 0 \\ N\to\infty}} \prod_{n=0}^{N} \hat{U}\left(t_0 + n\Delta,\ t_0 + (n+1)\Delta\right)\end{aligned}. \tag{2.7}$$

Note that in the limit as the size of the time step goes to zero, the integral in the exponential becomes a simple product

$$\lim_{\Delta\to 0} \hat{U}(t_0, t_0 + \Delta) = \mathcal{T}\left(e^{-i\int_{t_0}^{t_0+\Delta} \hat{H}(t)dt} \right) \cong e^{-i\Delta \hat{H}(t_0)}. \tag{2.8}$$

In order to apply the time evolution operator numerically, two approximations are made. First, the infinite product in the exact expression above is approximated as a finite product. That is, let N be some large but *finite* number and let Δ be some small positive number such that

$$t_1 - t_0 = N\Delta. \tag{2.9}$$

where $t_1 - t_0$ is the total time of propagation. In order for this approximation to be valid, the time step, Δ, must be small enough that the Hamiltonian does *not* change appreciably during the time step

$$\hat{H}(t) \approx \hat{H}(t+\Delta). \tag{2.10}$$

The second approximation is how the exponential Hamiltonian operator given in (2.8) is applied. The seven subsections below describe different algorithms for implementing this second approximation.

The basic time propagation scheme starts with a system described by a set of wavefunctions in some initial state that is often (but not necessarily) the ground state,

$$n_0(\mathbf{r}) = \sum_i f_i \left|\psi_i^0(\mathbf{r})\right|^2, \tag{2.11}$$

where n_0 is the initial density, f_i are the occupation coefficients and ψ_i^0 are the initial wavefunctions. The basic time propagation scheme is then as follows:

```
$Given:\ n_0, f_i, \psi_i^0$
    $t = t_0$
    $\psi_i(t) = \psi_i^0$
    $n(t) = n_0$
    $while\ t < t_1$
        $\hat{H}(t) = \hat{H}\left[n(t), \phi_\alpha^{ext}(t)\right]$
        $\psi_i(t+\Delta) = e^{-i\Delta\hat{H}(t)}\psi_i(t)$
        $n(t+\Delta) = \sum_i f_i \left|\psi_i(t+\Delta)\right|^2$
        $t = t + \Delta$
    $end$
```
(2.12)

where $\phi_\alpha^{ext}(t) = \left[\upsilon_{ext}(t), \mathbf{A}_{ext}(t)\right]$ is an external time dependent 4-vector potential (e.g. the time-dependent electromagnetic field due to light or the motion of nuclei – there is no

DFT theorem for an external vector potential, but the option has been included in the algorithms; the issue is dicussed further in Chapter 4). Note that the Hamiltonian is updated using the density and the external time potential. Although not shown here, in general the Hamiltonian must be updated using not only the external 4-vector potential and the scalar density but also the current density **j**. However, if the Adiabatic Local Density Approximation (ALDA) is used, then the Hamiltonian is not necessarily a functional of the current density. In this scheme the Hamiltonian, the density and the wavefunctions are all updated simultaneously at each time step while the occupations remain fixed throughout the calculation.

Each subsection below describes a different algorithm that can be used to apply the exponential operator, $e^{-i\Delta\hat{H}}$. The methods described below are compared with respect to unitarity, time symmetry, stability, accuracy, and efficiency. The accuracy of a single time propagation step is given by the order of the Taylor series expansion (e.g. $O\left[\left(\Delta\hat{H}\right)^{n}\right]$ is accurate to order n in $\Delta\hat{H}$). The application of the Hamiltonian to the wavefunctions ($\hat{H}\psi_i$) and the calculation of the overlap matrix $\left\langle\psi_i\middle|\psi_j\right\rangle$ are the most time consuming operations of a typical calculation. Therefore, the efficiency is typically reported as the number of $\hat{H}\psi_i$ and or $\left\langle\psi_i\middle|\psi_j\right\rangle$ operations per time step. The stability of a method is a measure of the unitary-ness of that method (i.e. how many times the method can be applied before the wavefunctions lose orthonormality).

There are seven algorithms described in the following seven subsections. The first three algorithms, the Diagonalization method, the Crude Euler, and the Crank-Nicholson [1, 2] propagation scheme are described but have not been implemented. The remaining four methods for applying the time evolution operator – the Chebychev [3] expansion, the Multi-Step Differencing Scheme [4], the Short Iterative Lanczos [5] method and the split operator [6] method – are not only described in detail but have been implemented by the author.

2.2.1. Diagonal (Exact) Time Propagator

In the limit as the time step size is small enough that the Hamiltonian does not change appreciably, the time propagation operator (2.8) may be applied trivially. The wavefunctions must be eigenstates of the Hamiltonian at every time step. Therefore, the eigenvalue equation below must be satisfied

$$\hat{H}(t)\psi_i(t) = \varepsilon_i(t)\,\psi_i(t). \tag{2.13}$$

The time propagation equation is

$$\psi_i(t+\Delta) = e^{-i\Delta\hat{H}(t)}\psi_i(t). \tag{2.14}$$

Performing a Taylor series expansion on the above equation yields

$$\psi_i(t+\Delta) = e^{-i\Delta\hat{H}(t)}\psi_i(t) = \sum_{n=0}^{\infty}\left[\frac{(-i\Delta)^n}{n!}\hat{H}^n(t)\right]\psi_i(t). \tag{2.15}$$

If (2.13) holds, then the Hamiltonian can be applied any number of times and the energy eigenvalue can be substituted for the Hamiltonian $\hat{H}^n\psi_i = \varepsilon_i^n\psi_i$. Substituting (2.13) into (2.15) and contracting the infinite sum yields

$$\psi_i(t+\Delta) = \sum_{n=0}^{\infty}\left[\frac{(-i\Delta)^n}{n!}\hat{H}^n(t)\right]\psi_i(t) = \sum_{n=0}^{\infty}\left[\frac{(-i\Delta)^n}{n!}\varepsilon_i^n(t)\right]\psi_i(t) = e^{-i\Delta\varepsilon_i(t)}\psi_i(t). \tag{2.16}$$

A method for applying the full time-propagation operator based on this technique requires that the Hamiltonian be diagonalized and the wavefunctions be projected onto the new basis at every time step. The state of the system is projected onto a basis of eigenstates of the Hamiltonian, $|\psi_i(t)\rangle$. In principle, it is sufficient to keep only one basis function per electron if one includes spin (or one basis function per two electrons if one ignores spin). However, for this method it is necessary to include enough eigenstates so that the basis spans the space of the state as it evolves in time. In the scheme outlined below, the state of the system at time *t* is described by the coefficients $c_i(t)$

```
$t = t_0$
while $t < t_1$
    $t = t + \Delta$
    update $\hat{H}$
    Calculate new basis at time t $\hat{H}(t)|\psi_i(t)\rangle = \varepsilon_i(t)|\psi_i(t)\rangle$        (2.17)
    Project state onto new basis $c_i(t) = \sum_j c_j(t-\Delta)\langle\psi_j(t)|\psi_i(t-\Delta)\rangle$
    Propagate basis $\psi_i(t) = e^{-i\Delta\varepsilon_i(t)}\psi_i(t-\Delta)$
end
```

As long as the new basis at each time step continues to span the space of the state as it evolves in time, the method is very accurate, unitary and stable. Assuming that the basis spans the space of the state, then one can prove that the method is unitary explicitly:

$$\hat{U}\hat{U}^{\dagger} = e^{-i\Delta\varepsilon_i} e^{i\Delta\varepsilon_i} = \mathbf{1} \tag{2.18}$$

It can also be shown that it is symmetric in time

$$\begin{aligned} \hat{U}\,(t, t+\Delta) &= \hat{U}^{-1}\,(t+\Delta, t) \\ e^{-i\Delta\varepsilon_i} &= e^{-\left[-i(-\Delta)\varepsilon_i\right]} = e^{-i\Delta\varepsilon_i} \end{aligned} \tag{2.19}$$

It is difficult to determine how many basis functions are needed before the run starts. If there are not enough basis functions to span the space of the state as it evolves, then during the projection part of the scheme, electrons are effectively lost (e.g. the method is unstable). The accuracy of the propagator also depends on how well the eigenvalue equation is satisfied. When iterative self-consistent eigensolvers are implemented, the eigenvalue equation can be solved with controllable error. One can measure the error in the eigenvalue equation for each eigenstate and eigenvalue.

$$error = \left\langle \psi_i(t) \middle| \hat{H} - \varepsilon_i(t) \middle| \psi_i(t) \right\rangle \tag{2.20}$$

As long as the error is negligible and there are enough basis functions to span the space of the state as it evolves, this method is very accurate and stable.

This method is very inefficient (relative to other methods) because not only must the Hamiltonian be diagonalized but the full overlap must also be calculated for the projection operation at every time step. Moreover, as mentioned earlier, many more basis functions are required in order to span the space of the state than the minimum that would otherwise be necessary just to represent the electrons (i.e. one basis state per electron if including spin or one basis state per two electrons if not including spin).

2.2.2. Crude Euler

Perhaps the most obvious method for applying the exponential operator is a simple Taylor series expansion. One truncates the infinite sum given in (2.15) to N terms in order to yield an expression that can be implemented numerically

$$\psi_i(t+\Delta) = \sum_{n=0}^{N-1} \left[\frac{(-i\Delta)^n}{n!} \hat{H}^n(t) \right] \psi_i(t). \tag{2.21}$$

This method is often referred to as the Euler or Crude Euler scheme [4]. In this method, the number of $\hat{H}\psi_i$ operations per time step (and thus the accuracy) is determined by the N, which is chosen by the user. This method is unconditionally unstable for any finite number of terms, N, in the sum in (2.21). To show this, consider an expansion with N=1, i.e.,

$$\hat{U}_{EU}(t, t+\Delta) = 1 - i\Delta\hat{H} \ . \tag{2.22}$$

Substitute this expansion into (2.3) to test whether it is unitary

$$\hat{U}_{EU}\hat{U}_{EU}^{\dagger} = \left(1 - i\Delta\hat{H}\right)\left(1 + i\Delta\hat{H}\right) = 1 + \Delta^2\hat{H}^2 \neq 1 \, . \tag{2.23}$$

The error in the unitarity of $\hat{U}_{EU}$ is $O\left[\left(\Delta\hat{H}\right)^2\right]$. This expansion is not symmetric in time as can be shown by substituting it into (2.5)

$$\hat{U}_{EU}\left(t_0, t_0 + \Delta\right) = 1 - i\Delta\hat{H} \neq \left(1 + i\Delta\hat{H}\right)^{-1} = \hat{U}_{EU}^{-1}\left(t_0 + \Delta, t_0\right). \tag{2.24}$$

It can be shown by multiplying both sides by $\left(1 + i\Delta\hat{H}\right)$ that this relation has an error of $O\left[\left(\Delta\hat{H}\right)^2\right]$.

To study the stability of the method, assume that the wavefunctions are eigenstates of the Hamiltonian [7] so that the wavefunctions at the next time step are given by

$$\psi_m(t + \Delta) = e^{-i\Delta\varepsilon_m}\psi_m(t) \, . \tag{2.25}$$

One can define a growth factor, g, that can be used to the measure of the ability of the method to conserve normalization of the wavefunctions. It is a complex number that relates the wavefunctions from one time step to the next

$$\psi_m(t + \Delta) = g\,\psi_m(t) \, . \tag{2.26}$$

For the exact evolution, the growth factor is $g = e^{-i\Delta\varepsilon_m}$. When approximating the exponential time propagator, the form of the growth factor must be modified to include the error.

$$g \equiv |g| e^{-i\Delta\varepsilon_m + ie_{phase}}, \tag{2.27}$$

where e_{phase} is the error in the phase. It is also assumed for the sake of the analysis that g does not vary in time. In this way, the error in the magnitude can be analyzed separately from the error in the phase. Note that if the magnitude of the growth factor is not unity, $|g| \neq 1$, then the magnitude of the wavefunctions will either grow or decay exponentially with the number of time steps. On the other hand, the error in the phase accumulates linearly with the number of time steps:

$$e_{phase}(N) = Ne_{phase}. \tag{2.28}$$

The stability of the Crude Euler propagator is then found by substituting it into (2.26) (again it is assumed that it the wavefunctions are eigenstates of the Hamiltonian)

$$\psi_m(t+\Delta) = (1 - i\Delta\varepsilon_m)\psi_m(t). \tag{2.29}$$

Following the convention of Iitaka [7], define a dimensionless quantity $\alpha \equiv \Delta\varepsilon_m$ so that the growth factor is then

$$g_{EU} = 1 - i\alpha. \tag{2.30}$$

As can be seen immediately, the magnitude of the growth factor for the Crude Euler method is greater than unity for any nonzero time step size (i.e. $|g_{EU}| > 1$). Therefore the Crude Euler method is unconditionally unstable for any nonzero time step size.

Finally, it can be shown that the error in the accuracy is $O\left[\left(\Delta\hat{H}\right)^2\right]$ by simply summing the remaining terms in the expansion:

$$error_{EU} = \sum_{n=2}^{\infty} \frac{(-i\Delta)^n}{n!} \hat{H}^n(t). \tag{2.31}$$

It is assumed that the time step is chosen small enough that $\left|\Delta\hat{H}\right| < 1$ and therefore the total error is $O\left[\left(\Delta\hat{H}\right)^2\right]$.

The efficiency of the method is simply the number of $\hat{H}\psi_i$ operations per time step as there is no need for re-orthogonalization. So the efficiency is proportional to the order of the expansion in the Taylor series. For example, if one chooses $N=1$ then there is only one $\hat{H}\psi_i$ operation per time step.

Note that although the above analysis is for an expansion of $N=1$, it holds that the method is not unitary, unconditionally unstable and inaccurate for any finite N to $O\left[\left(\Delta\hat{H}\right)^{N+1}\right]$. Therefore one could simply choose N to be large enough that $\hat{U}_{EU}$ is stable and accurate to machine precision. The reason why this method was not implemented by the author is that there are more optimal polynomial expansions (e.g. the Chebychev and Short Iterative Lanzcos methods).

2.2.3. Crank-Nicholson

Goldberg, Schey and Schwartz [8] first applied the Crank-Nicholson approximation to solve the 1-D TDSE. Consider time evolving the system forward and backward with a simple two-term Taylor expansion of the time evolution operator

$$\psi(\Delta) = \left(\mathbf{1} - i\Delta\hat{H}\right)\psi(0), \tag{2.32}$$

$$\psi(-\Delta) = \left(\mathbf{1} + i\Delta\hat{H}\right)\psi(0). \tag{2.33}$$

Multiplying both sides of (2.33) on the left by $\left(\mathbf{1} + i\Delta\hat{H}\right)^{-1}$ yields an expression for the state at *t*=0:

$$\psi(0) = \left(\mathbf{1} + i\Delta\hat{H}\right)^{-1}\psi(-\Delta). \tag{2.34}$$

By halving the time step, shifting the time, and substituting (2.34) into (2.32), one may obtain the following expression

$$\psi(\Delta) = \left(\mathbf{1} - i\frac{\Delta}{2}\hat{H}\right)\left(\mathbf{1} + i\frac{\Delta}{2}\hat{H}\right)^{-1}\psi(0). \tag{2.35}$$

Note that this is often referred to as the Caley approximation to the exponential time evolution operator [9]. Nevertheless, this expression will be referred to as the Crank-Nicholson scheme,

$$\hat{U}_{CN}(0,\Delta) \equiv \left(\mathbf{1} - i\frac{\Delta}{2}\hat{H}\right)\left(\mathbf{1} + i\frac{\Delta}{2}\hat{H}\right)^{-1}. \tag{2.36}$$

Perhaps the most striking feature of this scheme is that it is an implicit method. i.e, it is necessary to invert the Hamiltonian in order to apply this method. One can show that the Crank-Nicholson scheme is unitary by substituting (2.36) into (2.3):

$$\begin{aligned}\hat{U}_{CN}^{\dagger}\hat{U}_{CN} &= \left[\left(\mathbf{1} - i\frac{\Delta}{2}\hat{H}\right)\left(\mathbf{1} + i\frac{\Delta}{2}\hat{H}\right)^{-1}\right]^{\dagger}\left(\mathbf{1} - i\frac{\Delta}{2}\hat{H}\right)\left(\mathbf{1} + i\frac{\Delta}{2}\hat{H}\right)^{-1} \\ &= \left(\mathbf{1} - i\frac{\Delta}{2}\hat{H}\right)^{-1}\left(\mathbf{1} + i\frac{\Delta}{2}\hat{H}\right)\left(\mathbf{1} - i\frac{\Delta}{2}\hat{H}\right)\left(\mathbf{1} + i\frac{\Delta}{2}\hat{H}\right)^{-1}.\end{aligned} \tag{2.37}$$

Since the middle two terms commute, $\left[\left(\mathbf{1}+i\frac{\Delta}{2}\hat{H}\right),\left(\mathbf{1}-i\frac{\Delta}{2}\hat{H}\right)\right]=0$, the expression above can be rearranged:

$$\hat{U}_{CN}^{\dagger}\hat{U}_{CN}=\left(\mathbf{1}-i\frac{\Delta}{2}\hat{H}\right)^{-1}\left(\mathbf{1}-i\frac{\Delta}{2}\hat{H}\right)\left(\mathbf{1}+i\frac{\Delta}{2}\hat{H}\right)\left(\mathbf{1}+i\frac{\Delta}{2}\hat{H}\right)^{-1}=\mathbf{1}. \tag{2.38}$$

Thus, the Crank-Nicholson propagator is unitary.

Next, test whether the Crank-Nicholson scheme is symmetric in time by taking one time step forward and then take another time step back

$$\begin{aligned}&\hat{U}_{CN}(t+\Delta,t)\hat{U}_{CN}(t,t+\Delta)\psi(t)\\&=\left(\mathbf{1}+i\frac{\Delta}{2}\hat{H}\right)\left(\mathbf{1}-i\frac{\Delta}{2}\hat{H}\right)^{-1}\left(\mathbf{1}-i\frac{\Delta}{2}\hat{H}\right)\left(\mathbf{1}+i\frac{\Delta}{2}\hat{H}\right)^{-1}\psi(t)\\&=\psi(t).\end{aligned} \tag{2.39}$$

Note that the wavefunction has not changed, whereby the Crank-Nicholson scheme is symmetric in time.

To determine the stability of the Crank-Nicholson scheme, substitute the Crank-Nicholson approximation (2.36) into (2.26), which yields an expression for the growth factor,

$$g_{CN}=\left(1-i\frac{\alpha}{2}\right)\left(1+i\frac{\alpha}{2}\right)^{-1}, \tag{2.40}$$

where it has been assumed for the sake of the stability analysis that the wavefunctions are eigenstates of the Hamiltonian and the dimensionless quantity α is defined as $\alpha\equiv\varepsilon_m\Delta$. From inspection, it can be seen that $|g_{CN}|=1$ and therefore the Crank-Nicholson propagator is unconditionally stable.

Since the Taylor series expansion in the derivation of the Crank-Nicholson propagator is to first order, it is clear that the method is accurate to second order.

Finally, consider the efficiency of the Crank-Nicholson scheme. There are effectively two $\hat{H}\psi_i$ operations in addition to one inversion of the matrix, $\left(\mathbf{1}+i\frac{\Delta}{2}\hat{H}\right)$, per time step. With the advent of iterative methods, modern plane-wave pseudopotential DFT codes typically do not form the full Hamiltonian matrix and invert it. For such codes, the full Hamiltonian matrix is never formed. Instead, the Hamiltonian is only applied in operator form. The benefit of this approach is that if the size of the system is $O[N]$, then the memory requirements will also be $O[N]$. Conversely, if one forms the full Hamiltonian matrix, the memory requirements will be of size $O\left[N^2\right]$. According to Iitaka [7], "this implicit method is prohibitive in more than two dimensions due to the large memory and CPU time required by the matrix inversion".

In 1996, Choptuik [10] suggested solving the implicit Crank-Nicholson equation iteratively, which would effectively make it an explicit method and remove the need to form and invert the full Hamiltonian. However, it was shown by Teukolsky [11] that performing more than two iterations does not improve the accuracy of the method. Moreover, the method becomes *conditionally* stable when it is solved iteratively. It is for these reasons that this method was not implemented by the author.

2.2.4. Multi-Step Differencing Scheme

In 1978, Askar and Cakmak [4] suggested a simple, conditionally stable and explicit method to approximate the time propagation operator. They recognized that the source of the instability of the straightforward Taylor expansion (Crude Euler) of the time evolution operator is the lack of time symmetry. Their method is sometimes referred to as a time-symmetrized Euler method but more often as the Multi-step Differencing Scheme (MSDS). The derivation of the method starts by taking the difference of the wavefunction at the next step and at the previous step,

$$\psi(t+\Delta)-\psi(t-\Delta)=\left(e^{-i\Delta\hat{H}}-e^{i\Delta\hat{H}}\right)\psi(t)\,. \tag{2.41}$$

One then approximates the exponential operators with a second-order Taylor series expansion,

$$\psi(t+\Delta)-\psi(t-\Delta)\cong\left\{\left[1-i\Delta\hat{H}-\left(\Delta\hat{H}\right)^{2}\right]-\left[1+i\Delta\hat{H}-\left(\Delta\hat{H}\right)^{2}\right]\right\}\psi(t)\,. \tag{2.42}$$

Canceling terms and rearranging the above equation yields an explicit method that is accurate to second order (i.e. the error is third order),

$$\psi(t+\Delta)=\psi(t-\Delta)-2i\Delta\hat{H}\psi(t)\,. \tag{2.43}$$

The method described by (2.43) is sometimes referred to as MSD2 as it is the second-order Multi-step Differencing Scheme.

Since the MSD2 requires the history, it is necessary to represent the MSD2 propagator as a matrix. Assuming that the initial state, $\psi(0)$, is given and letting $\psi(\Delta)=\psi(0)$, then the MSD2 propagation matrix equation for a time evolution with *N* steps has the following form

$$\begin{bmatrix} \psi(0) \\ \psi(\Delta) \\ \psi(2\Delta) \\ \psi(3\Delta) \\ \vdots \\ \psi(N\Delta) \end{bmatrix} = \begin{bmatrix} 1 & 0 & 0 & 0 & \dots & 0 \\ 1 & 0 & 0 & 0 & \dots & 0 \\ 1 & -2i\Delta\hat{H} & 0 & 0 & \cdots & 0 \\ 0 & 1 & -2i\Delta\hat{H} & 0 & \dots & 0 \\ \vdots & \vdots & \vdots & \vdots & \ddots & 0 \\ 0 & 0 & 0 & 1 & -2i\Delta\hat{H} & 0 \end{bmatrix} \begin{bmatrix} \psi(0) \\ \psi(\Delta) \\ \psi(2\Delta) \\ \psi(3\Delta) \\ \vdots \\ \psi(N\Delta) \end{bmatrix}. \tag{2.44}$$

From this equation, it can be readily seen that the MSD2 propagator is a matrix of the following form

$$\mathbf{U}_{MSD2} = \begin{bmatrix} 1 & 0 & 0 & 0 & \dots & 0 \\ 1 & 0 & 0 & 0 & \dots & 0 \\ 1 & -2i\Delta\hat{H} & 0 & 0 & \cdots & 0 \\ 0 & 1 & -2i\Delta\hat{H} & 0 & \dots & 0 \\ \vdots & \vdots & \vdots & \vdots & \ddots & 0 \\ 0 & 0 & 0 & 1 & -2i\Delta\hat{H} & 0 \end{bmatrix}. \tag{2.45}$$

With this expression for the MSD2 propagator, one can check whether the method is unitary. Substituting (2.45) into (2.3),

$$\mathbf{U}^{\dagger}_{MSD2}\mathbf{U}_{MSD2} = \begin{bmatrix} 1 & 1 & 1 & 0 & \dots & 0 \\ 1 & 1 & 1 & 0 & \dots & 0 \\ 1 & 1 & \left(1+4\Delta^2\hat{H}^2\right) & -2i\Delta\hat{H} & \cdots & 0 \\ 0 & 0 & 2i\Delta\hat{H} & \left(1+4\Delta^2\hat{H}^2\right) & \dots & 0 \\ \vdots & \vdots & \vdots & \vdots & \ddots & -2i\Delta\hat{H} \\ 0 & 0 & 0 & 0 & 2i\Delta\hat{H} & \left(1+4\Delta^2\hat{H}^2\right) \end{bmatrix} \neq \mathbf{1}. \tag{2.46}$$

As this is not equal to identity, the MSD2 scheme is *not* unitary.

The MSD2 propagator is symmetric with respect to time. This should not be surprising since enforcing time symmetry was one of the goals of the developers of the method. To show this, note that by adding $2i\Delta\hat{H}$ to both sides of the MSD2 equation

(2.43) yields an expression to time step backwards. Therefore, the same expression can be used to time step forward and backward,

$$\psi(t-\Delta)=\psi(t+\Delta)+2i\Delta\hat{H}\psi(t). \tag{2.47}$$

Next, consider the stability of the MSD2 propagator. Once again, for the sake of stability analysis, assume that the wavefunctions are eigenstates of the Hamiltonian. Moreover, it is assumed that the growth factor, *g*, is some complex number that relates the wavefunctions at one time step to the next as shown in (2.26). One can then form a stability equation from the MSD2 equation, (2.43), by making the substitutions for the wavefunctions at three time steps: $\psi(t)$, $\psi(t+\Delta)=g\,\psi(t)$ and $\psi(t+2\Delta)=g^2\,\psi(t)$,

$$g^2\psi(t)=\psi(t)-2i\Delta\hat{H}g\psi(t). \tag{2.48}$$

Dividing the above equation by the wavefunction at *t* yields the following stability equation.

$$g^2+2i\alpha g-1. \tag{2.49}$$

Solving for *g* gives

$$g=-i\alpha\pm\sqrt{1-\alpha^2}. \tag{2.50}$$

The condition for stability is that the magnitude of *g* be unity. The magnitude of (2.50) depends on whether or not α is larger than unity:

$$|g|=\begin{cases}1 & ,\quad \alpha\le 1\\ \sqrt{2\alpha^2\mp\alpha\sqrt{\alpha^2-1}-1} & ,\quad \alpha>1.\end{cases} \tag{2.51}$$

As can be seen from the above expression for the magnitude of the growth factor, MSD2 is conditionally stable with the condition $\alpha\le 1$. Thus, the size of the time step is effectively restricted by the value (magnitude) of the largest eigenvalue of the Hamiltonian $\Delta \le \frac{1}{\left|\varepsilon_{\max}\right|}$.

MSD2 requires only one $\hat{H}\psi_i$ operation per time step to achieve accuracy to third order. With no orthogonalization and only one $\hat{H}\psi_i$ operation required per time step, MSD2 is very efficient if third-order accuracy is sufficient.

It is possible to extend the accuracy of the method to higher orders. For example, MSD4 is accurate to fourth order and is derived in the following manner.

$$e^{-2i\Delta\hat{H}} - e^{2i\Delta\hat{H}} = -4i\Delta\hat{H} - \frac{8}{3}\left(i\Delta\hat{H}\right)^3, \tag{2.52}$$

$$e^{-i\Delta\hat{H}} + e^{i\Delta\hat{H}} = 2 + \left(i\Delta\hat{H}\right)^2. \tag{2.53}$$

Factoring out $4i\Delta\hat{H}$ from (2.52),

$$e^{-2i\Delta\hat{H}} - e^{2i\Delta\hat{H}} = -4i\Delta\hat{H}\left[1 + \frac{2}{3}\left(i\Delta\hat{H}\right)^2\right]. \tag{2.54}$$

Rearranging (2.53) to solve for $\left(i\Delta\hat{H}\right)^2$ and substituting into the above equation leaves

$$e^{-2i\Delta\hat{H}} - e^{2i\Delta\hat{H}} = -4i\Delta\hat{H}\left[1 + \frac{2}{3}\left(e^{-i\Delta\hat{H}} + e^{i\Delta\hat{H}} - 2\right)\right]. \tag{2.55}$$

Multiplying both sides of this equation by $\psi(t)$ and noting that $\psi(t+2\Delta) = e^{-2i\Delta\hat{H}}\psi(t)$, $\psi(t+\Delta) = e^{-i\Delta\hat{H}}\psi(t)$, $\psi(t-\Delta) = e^{i\Delta\hat{H}}\psi(t)$, and $\psi(t-2\Delta) = e^{2i\Delta\hat{H}}\psi(t)$, leaves the following expression for the MSD4 propagator

$$\psi(t+2\Delta) = \psi(t-2\Delta) - 4i\Delta\hat{H}\left[\frac{2}{3}\psi(t-\Delta) - \frac{1}{3}\psi(t) + \frac{2}{3}\psi(t+\Delta)\right]. \tag{2.56}$$

This scheme is referred to as MSD4 since it is accurate to fourth order. Just as for MSD2, it can be shown that MSD4 is not unitary, symmetric in time, and conditionally stable. However, the growth factor equation for MSD4 is different than that of MSD2 and therefore the condition for stability is different. The growth factor equation for MSD4 is then by

$$g^4 = 1 - \frac{8}{3} i\alpha g + \frac{4}{3} i\alpha g^2 - \frac{8}{3} i\alpha g^3 . \tag{2.57}$$

The four roots of this equation must be calculated numerically. The stability condition for MSD4 is that $\alpha < 0.4$ or equivalently, $\Delta < \frac{0.4}{|\varepsilon_{\max}|}$. Notice that MSD4 only requires one $\hat{H}\psi_i$ operation per time step but yields fourth order accuracy. However, it is necessary to take smaller time steps with MSD4 due to the stability condition. It is possible to derive Multi-Step Differencing Schemes of still higher order. For example, MSD6 is given by

$$\begin{aligned}\psi(t+3\Delta) = \psi(t-3\Delta) - 6i\Delta\hat{H}\Big[&\frac{11}{20}\psi(t-2\Delta) - \frac{7}{10}\psi(t-\Delta) \\ &+ \frac{13}{10}\psi(t) - \frac{7}{10}\psi(t+\Delta) + \frac{11}{20}\psi(t+2\Delta)\Big].\end{aligned} \tag{2.58}$$

Just as for MSD4, the stability condition for MSD6 must also be calculated numerically. It has been found to be $\alpha < 0.4$ or equivalently $\Delta < \frac{0.1}{|\varepsilon_{\max}|}$. MSD6 is accurate to sixth order with only one $\hat{H}\psi_i$ required per time step but the stability of condition limits the maximum time step size to $\frac{1}{10}$ that of MSD2. The author has implemented MSDS methods up to 12th order.

2.2.5. Chebychev Expansion

In 1984, Hillel Tal-Ezer and Ronnie Kosloff proposed approximating the time propagation operator using a Chebychev expansion [3]. The following description follows from the excellent survey of time propagator schemes [12] by Leforestier et al. In this approach, the time-evolution operator (2.8) is approximated by a polynomial expansion of the operator $-i\Delta\hat{H}$,

$$e^{-i\Delta\hat{H}} \approx \sum_{n=0}^{N-1} a_n P_n\left(-i\Delta\hat{H}\right). \tag{2.59}$$

Where a_n is the n^{th} coefficient of the n^{th} polynomial $P_n\left(-i\Delta\hat{H}\right)$. The Taylor series expansion (perhaps the most well-known type of polynomial expansion) of this function would be $a_n = \frac{1}{n!}$ and $P_n\left(-i\Delta\hat{H}\right) = \left(-i\Delta\hat{H}\right)^n$. The Crude Euler scheme described in section 2.1.1 is a polynomial expansion using a Taylor series approximation to the time propagation operator. However, it has been shown that the Taylor series approximation is not an optimal choice for expanding an exponential function [3]. The optimal polynomial approximation is the Cheybchev expansion. According to Leforestier et al. [12], "In this case it is known that the Chebyshev polynomial approximations are optimal, since the maximum error in the approximation is minimal compared to almost all possible polynomial approximations."

Whereas the Chebychev polynomials are only defined on the interval $[-1,1]$, the complex Chebychev polynomials are defined in the interval $[-i,i]$. Therefore it is necessary to shift and renomalize the $-i\Delta\hat{H}$ operator so that all of the eigenvalues lie within this interval. To that end, define the following operator based on the Hamiltonian that is guaranteed to have eigenvalues that are in the interval $\left[-1,1\right]$

$$\hat{H}_{norm} \equiv 2\frac{\hat{H}-\hat{I}\left(\frac{1}{2}E_{grid}+E_{min}\right)}{E_{grid}}. \tag{2.60}$$

E_{max} and E_{min} are the maximum and minimum possible energy of the Hamiltonian and $E_{grid} \equiv E_{max}$ - E_{min}. Given that $\hat{H}=\hat{T}+\hat{V}$, then $E_{max}=\frac{G_{max}^2}{2m}+V_{max}$ and $E_{min}=V_{min}$, where G_{max} is the magnitude of the largest Fourier component in reciprocal space (which is related to the grid spacing, Δx, in real space as $G_{max}=\frac{1}{\Delta x}$). To find V_{min} and V_{max}, simply scan through the local potential and find the minimum and maximum values.

To construct the propagator, first shift the spectrum of the eigenvalues of the Hamiltonian

$$e^{-i\Delta\hat{H}}=e^{-i\Delta\left(\hat{H}-\hat{I}\xi+\hat{I}\xi\right)}=e^{-i\Delta\xi}e^{-i\Delta\left(\hat{H}-\hat{I}\xi\right)}, \tag{2.61}$$

where $\xi \equiv \frac{1}{2}\left(E_{max}+E_{min}\right)$ is the average of the maximum and minimum possible eigenvalues and is used to shift the spectrum of the eigenvalues so that it (the spectrum) is centered at zero. Next multiply and divide the argument in (2.61) by E_{grid},.

$$e^{-i\Delta\hat{H}}=e^{-i\Delta\xi}e^{-\alpha i\hat{H}_{norm}}, \tag{2.62}$$

where $\hat{H}_{norm}$ was defined in (2.60) and $\alpha \equiv \frac{E_{grid}\Delta}{2}$. The above expression for the time evolution propagator can be directly approximated via the Chebychev expansion

$$e^{-i\Delta\hat{H}}=e^{-i\Delta\xi}\sum_{n=0}^{N-1}a_n\,\phi_n\left(-i\hat{H}_{norm}\right), \tag{2.63}$$

where a_n is the n^{th} Chebychev coefficient and ϕ_n is the n^{th} Chebychev polynomial. The polynomials are generated by the following recursion relation

$$\phi_{n+1}(x) = 2x\phi_n(x) + \phi_{n-1}(x), \tag{2.64}$$

where $x = -i\hat{H}_{norm}$ and the recursion relation is initialized with $\phi_0 = 1$ and $\phi_1 = x$. The Chebychev coefficients are calculated from the following

$$a_n = \int_{-i}^{i} dx \frac{e^{\alpha x}\phi_n(x)}{\sqrt{1-x^2}} = \begin{cases} J_n(\alpha)\ , n = 0 \\ 2J_n(\alpha)\ , n \geq 1. \end{cases} \tag{2.65}$$

where $J_n(\alpha)$ are Bessel functions of the first kind of order *n*. One property of Bessel functions of the first kind is that $J_n(\alpha) \to 0$ exponentially fast when $n > \alpha$. This property also contributes to why the Chebychev method is considered the optimal polynomial expansion of the time propagation operator.

This method is neither unitary, symmetric in time, nor stable except when the expansion is completed to machine precision. In practice, one of the tests of the method during a calculation is how well the norm is conserved. That is, the norms of the wavefunctions are monitored during a run in order to determine whether the Chebychev approximation to the time propagation operator is still stable. Not surprisingly, the Chebychev method is extremely accurate – in practice, it is often expanded so that it is accurate to machine precision.

The efficiency of the Chebychev method is dependent on several factors. As mentioned above, once the number of terms, N, in the expansion exceeds $\alpha = \frac{1}{2}E_{grid}\Delta$, then the coefficients will vanish exponentially. Thus, once $N > \alpha$ then the number of additional $\hat{H}\psi$ required for the expansion to converge to machine precision is proportional to $\log(\alpha)$. The number of $\hat{H}\psi$ operations required to achieve a certain precision is then roughly

$$N = \alpha + \beta \log(\alpha), \tag{2.66}$$

where β is some proportionality constant. When α is large, the number of $\hat{H}\psi$ operations required to achieve the desired precision is $O(\alpha)$. However, the efficiency of the method suffers when α is small because the number of extra $\hat{H}\psi$ operations required by $\beta \log(\alpha)$ can begin to dominate.

The Chebychev method requires two additional wavefunction-sized data structures in order to implement the recursion relation. Therefore, the Chebychev method requires a constant (and relatively small) amount of memory regardless of the desired precision. It is for this reason that the Chebychev method is considered to be very efficient with respect to memory usage.

2.2.6. Split-Operator Method

In 1978, Feit and Fleck first presented the split operator method for solving the paraxial form of the Helmholtz equation for light propagating in an optical fiber [6, 13, 14, 15, 16]. In the original formulation, a solution to the paraxial form of the Helmholtz equation was cast in a form that is mathematically identical to the TDSE. A few years later, Feit, Fleck and Steiger implemented the split operator method to solve the TDSE directly [17, 18].

Let $\hat{A} = \hat{B} + \hat{C}$ where both $\hat{B}$ and $\hat{C}$ are Hermitian operators. The Trotter formula [19] can be applied to the following exponentiated operator $e^{a\hat{A}}$.

$$e^{a\hat{A}} = e^{a\left(\hat{B}+\hat{C}\right)} = \lim_{n\to\infty}\left(e^{\frac{a}{n}\hat{B}}e^{\frac{a}{n}\hat{C}}\right)^{n}, \tag{2.67}$$

where a is some scalar quantity. The split operator method proposed by Feit and Fleck is a 2nd order approximation to the Trotter formula (2.67) for the TDSE,

$$e^{a\hat{H}} = e^{a\left(\hat{T}+\hat{V}\right)} = e^{a\left(\frac{1}{2}\hat{T}+\hat{V}+\frac{1}{2}\hat{T}\right)} \approx e^{\frac{a}{2}\hat{T}}e^{a\hat{V}}e^{\frac{a}{2}\hat{T}}, \tag{2.68}$$

where $a \equiv -i\Delta$. Note that the kinetic energy operator, $\hat{T}$, is split in two so as to symmetrize the approximation – thus the "split operator" in the split operator method. As stated above, this approximation is accurate to 2nd order. The error is due to the fact that $\hat{T}$ and $\hat{V}$ do not commute [12, 20]. The usefulness of this method depends on the Fast Fourier Transform (FFT) which makes dual-space representations of the wavefunctions numerically efficient. The FFT requires only $N\log(N)$ multiple operations in order to transform a wavefunction of size N back and forth between reciprocal space and real space. Since the kinetic energy operator, $\hat{T}$, is diagonal in reciprocal space and the potential operator, $\hat{V}$, is diagonal in real space, one may apply the split operator method trivially with two FFT operations. The basic procedure is given below

$$\begin{aligned}
\tilde{\psi}(\mathbf{G};t+\Delta) &= e^{-i\frac{\Delta}{4}G^{2}}\tilde{\psi}(\mathbf{G};t)\\
\psi(\mathbf{r};t+\Delta) &= IFFT\left[\tilde{\psi}(\mathbf{G};t+\Delta)\right]\\
\psi(\mathbf{r};t+\Delta) &= e^{-i\Delta v(\mathbf{r})}\psi(\mathbf{r};t+\Delta)\\
\tilde{\psi}(\mathbf{G};t+\Delta) &= FFT\left[\psi(\mathbf{r};t+\Delta)\right]\\
\tilde{\psi}(\mathbf{G};t+\Delta) &= e^{-i\frac{\Delta}{4}G^{2}}\tilde{\psi}(\mathbf{G};t+\Delta).
\end{aligned} \tag{2.69}$$

where $\psi(\mathbf{r})$ is the wavefunction represented in real space, $\tilde{\psi}(\mathbf{G})$ is the wavefunction represented in reciprocal space, *FFT* is the Fast Fourier Transform which transforms the wavefunction from real space to reciprocal space, *IFFT* is the inverse Fast Fourier

Transform which transforms the wavefunction from reciprocal space back to real space, and G are reciprocal space grid points (i.e. integral multiples of the reciprocal space lattice vectors). The kinetic energy, $K.E. = \frac{G^2}{2m_e}$, is diagonal in reciprocal space (note that in (2.69), atomic units are used so that m_e=1), and $v(\mathbf{r})$ is the local potential (which is diagonal in real space).

In a series of publications, Matsuo Suzuki et al. formally described how to implement finite approximations of arbitrary order to the Trotter formula (2.67) for an operator that is the sum of non-commutating operators [21-26]. The so-called 2nd order Suzuki-Trotter split operator method for an exponentiated Hamiltonian consisting of n terms $\hat{H} = \sum_{j=1}^{n} \hat{H}_j$ is given by

$$e^{a\hat{H}} \approx e^{\frac{a}{2}\hat{H}_1} e^{\frac{a}{2}\hat{H}_2} \ldots e^{\frac{a}{2}\hat{H}_{n-1}} e^{a\hat{H}_n} e^{\frac{a}{2}\hat{H}_{n-1}} \ldots e^{\frac{a}{2}\hat{H}_2} e^{\frac{a}{2}\hat{H}_1} \equiv S_2(a). \tag{2.70}$$

Here $S_2(a)$ is defined as the 2nd order Suzuki-Trotter split operator method. The higher-order approximations are built up from $S_2(a)$. For example, the 4th order symmetric Suzuki-Trotter split operator for a time-dependent Hamiltonian is given by

$$S_4(a) = S_2(p_1 a; t_5) S_2(p_2 a; t_4) S_2(p_3 a; t_3) S_2(p_2 a; t_2) S_2(p_1 a; t_1). \tag{2.71}$$

In the above equation, the Hamiltonian is applied times given by

$$t_j \equiv \left(-\frac{p_j}{2} + \sum_{k=1}^{j} p_k \right) \Delta. \tag{2.72}$$

The parameters, p_j, in (2.71) and (2.72) are given by

$$\begin{aligned} p_1 = p_2 = p_4 = p_5 &= \frac{1}{4-4^{\frac{1}{3}}} \approx 0.41 \\ p_3 &= 1-4p_1 \approx -0.66\,. \end{aligned} \tag{2.73}$$

The parameters derived by Suzuki have the property that for any order of approximation, $|p_j| < 1$.

Many implementations of DFT treat core electrons differently from valence electrons in order to reduce the numerical workload of a given calculation. The contributions to the Hamiltonian from the nuclei and core electrons are combined and replaced with a pseudopotential. This approach is valid when the core electrons do not interact with the rest of the system (i.e. the other atoms). Although Vanderbilt's Ultrasoft-Pseudopotential (US) [27, 28, 29] method and Blochl's Projector-Augmented-Wave Method (PAW) [30] are becoming increasingly popular, perhaps the most common type of pseudopotential formulation is the separable nonlocal pseudopotential or Norm-Conserving Pseudopotential (NCP) method introduced by Kleinmann and Bylander [31]. In this formulation, the Kleinmann-Bylander potential, $\hat{V}_{KB}$, represents the contribution to the Hamiltonian from the nuclei and core electrons as the sum of atom-centered terms.

$$\hat{V}_{KB} = \sum_{\alpha} \upsilon_{\alpha}^{loc}(\mathbf{r}-\mathbf{R}_{\alpha}) + \upsilon_{\alpha lm}^{nl}(\mathbf{r}-\mathbf{R}_{\alpha})\,. \tag{2.74}$$

Here, υ_{α}^{loc} is the local contribution, $\upsilon_{\alpha lm}^{nl}$ is the nonlocal contribution and $\mathbf{R}_{\alpha}$ is the position of atom α. The local potential is just a spherically symmetric atom-centered function. It can be combined with the Hartree and Exchange-Correlation potentials to form a total local potential which can be applied trivially in real space as shown in (2.69). The nonlocal potential has the following form

$$v^{nl}_{\alpha lm}(\mathbf{r}) = \frac{v^{ps}_{\alpha l} \left| p_{\alpha lm} \right\rangle \left\langle p_{\alpha lm} \right| v^{ps}_{\alpha l}}{\left\langle p_{\alpha lm} \left| v^{ps}_{\alpha l} \right| p_{\alpha lm} \right\rangle}, \tag{2.75}$$

where $p_{\alpha lm}$ is an atomic pseudo-wavefunction, which is the product of a radial function and a spherical harmonic. The radial pseudopotential, $v^{ps}_{\alpha l}$, is an atom-centered spherically symmetric function. The quantity $v^{ps}_{\alpha l} \left| p_{\alpha lm} \right\rangle$ is referred to as a projector.

Joachim Theilhaber [32] first described how to implement the split operator method using the NCP atomic representation; however the derivation below follows the formulation of Sugino and Miyamoto [33]. The nonlocal pseudopotential (2.75) raised to the n^{th} power is given by

$$\left\{ v^{nl}_{\alpha lm}(\mathbf{r}) \right\}^n = \frac{v^{ps}_{\alpha l} \left| p_{\alpha lm} \right\rangle \left\langle p_{\alpha lm} \left| v^{ps}_{\alpha l} v^{ps}_{\alpha l} \right| p_{\alpha lm} \right\rangle^{n-1} \left\langle p_{\alpha lm} \right| v^{ps}_{\alpha l}}{\left\langle p_{\alpha lm} \left| v^{ps}_{\alpha l} \right| p_{\alpha lm} \right\rangle^n}, \quad n \geq 1 \tag{2.76}$$

In order to exponentiate the nonlocal pseudopotential, Taylor expand the exponential

$$\exp\left(x v^{nl}_{\alpha lm} \right) = \sum_{n=0}^{\infty} \frac{\left(x v^{nl}_{\alpha lm} \right)^n}{n!} = 1 + \frac{v^{ps}_{\alpha l} \left| p_{\alpha lm} \right\rangle \left[\sum_{n=1}^{\infty} \frac{1}{n!} \left(x \frac{\left\langle p_{\alpha lm} \left| v^{ps}_{\alpha l} v^{ps}_{\alpha l} \right| p_{\alpha lm} \right\rangle}{\left\langle p_{\alpha lm} \left| v^{ps}_{\alpha l} \right| p_{\alpha lm} \right\rangle} \right)^n \right] \left\langle p_{\alpha lm} \right| v^{ps}_{\alpha l}}{\left\langle p_{\alpha lm} \left| v^{ps}_{\alpha l} v^{ps}_{\alpha l} \right| p_{\alpha lm} \right\rangle} \tag{2.77}$$

The infinite sum in the above equation can be written as

$$\exp\left(x \frac{\left\langle p_{\alpha lm} \left| v^{ps}_{\alpha l} v^{ps}_{\alpha l} \right| p_{\alpha lm} \right\rangle}{\left\langle p_{\alpha lm} \left| v^{ps}_{\alpha l} \right| p_{\alpha lm} \right\rangle} \right) = 1 + \sum_{n=1}^{\infty} \frac{1}{n!} \left(x \frac{\left\langle p_{\alpha lm} \left| v^{ps}_{\alpha l} v^{ps}_{\alpha l} \right| p_{\alpha lm} \right\rangle}{\left\langle p_{\alpha lm} \left| v^{ps}_{\alpha l} \right| p_{\alpha lm} \right\rangle} \right)^n . \tag{2.78}$$

One may substitute (2.78) into (2.77) in order to obtain the following expression

$$\exp\left(x v^{nl}_{\alpha lm} \right) = 1 + \frac{v^{ps}_{\alpha l} \left| p_{\alpha lm} \right\rangle \left[\exp\left(x \frac{\left\langle p_{\alpha lm} \left| v^{ps}_{\alpha l} v^{ps}_{\alpha l} \right| p_{\alpha lm} \right\rangle}{\left\langle p_{\alpha lm} \left| v^{ps}_{\alpha l} \right| p_{\alpha lm} \right\rangle} \right) - 1 \right] \left\langle p_{\alpha lm} \right| v^{ps}_{\alpha l}}{\left\langle p_{\alpha lm} \left| v^{ps}_{\alpha l} v^{ps}_{\alpha l} \right| p_{\alpha lm} \right\rangle} . \tag{2.79}$$

When applying the above equation in a split operator calculation, both the projectors, $v_{\alpha l}^{ps}\left| p_{\alpha lm} \right\rangle$, and the matrix elements, $\left\langle p_{\alpha lm} \right| v_{\alpha l}^{ps} v_{\alpha l}^{ps} \left| p_{\alpha lm} \right\rangle$ and $\left\langle p_{\alpha lm} \right| v_{\alpha l}^{ps} \left| p_{\alpha lm} \right\rangle$, must be calculated in the same representation (i.e. real space or reciprocal space). Otherwise, the propagator is not be unitary according to Sugino and Miyamoto [33].

Finally, an expression for the 2nd order Suzuki-Trotter split operator propagator can be written as

$$S_2(\Delta) = e^{-i\frac{\Delta}{2}\hat{T}} \left\{ \prod_{\alpha lm}^{ascending} e^{-i\frac{\Delta}{2} v_{\alpha lm}^{nl}} \right\} e^{-i\Delta v_{total}^{loc}} \left\{ \prod_{\alpha lm}^{descending} e^{-i\frac{\Delta}{2} v_{\alpha lm}^{nl}} \right\} e^{-i\frac{\Delta}{2}\hat{T}}, \tag{2.80}$$

where the exponentiated nonlocal pseudopotentials on one side are applied in the reverse order as on the other side (thus maintaining the symmetry of the operation).

The split-operator method as described above is unitary and unconditionally stable. However, there is an additional cost in order to achieve unitarity and stability that is discussed below. The method is not time symmetric in general because the system is propagated using the potential at the current time step. However, Sugino and Miyamoto [33] suggested a self-consistent technique based on the railway interpolation scheme [34] that introduces time symmetry by approximating the potential at the half time step between the current time step and the next step.

As mentioned above, one can apply this split-operator scheme to any desired (even) order of accuracy using the method described by Suzuki. However, according to Sugino and Miyamoto [33], the fourth order decomposition appears to provide the optimal combination of performance and accuracy.

There is some subtlety in the analysis of the efficiency of the split operator method. In addition to the requirement described above that the nonlocal pseudopotential matrix elements and the projection operation take place in the same space, it is also necessary to include the full representation of the wavefunctions in order for this method to be unitary [35]. To understand why this is important, it is necessary to understand some of the subtler details of modern plane-wave DFT implementations. Because of the relation between the wavefunctions and the density (2.11), the maximum frequency required to represent the density is twice that of the wavefunctions [36]. Therefore, most modern dual-space (i.e. plane-wave) DFT implementations store the density on the full grid but store only the components of the reciprocal-space representation of the wavefunctions that are inscribed within a sphere in the reciprocal-space grid with the radius of the sphere equal to the wavefunction cutoff. In Figure 2.1, the light blue cube represents the full reciprocal space grid on which the density is

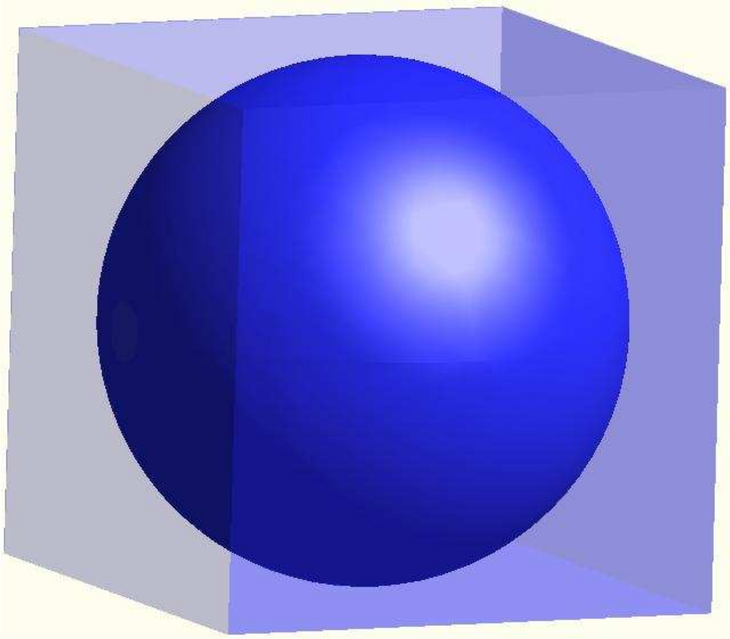

Figure 2.1: The light blue cube represents the full reciprocal space grid. The dark blue sphere centered inside the cube represents the reduced grid on which the wavefunctions are represented.

represented. The dark blue sphere centered in the cube has a radius equal to the cutoff density for the wavefunctions and the wavefunctions themselves are represented in reciprocal space with only those grid points that fall within this sphere.

Note that even if one sets the cutoff frequency for the wavefunctions equal to the cutoff frequency for the density (i.e. let the sphere be perfectly inscribed in the cube), the number of grid points inside the sphere is roughly half the number of points in the full grid. This result follows from the fact that the density of grid points in reciprocal space is constant and the volume of a sphere inscribed in a cube is roughly half that of the cube itself. In a typical calculation, the wavefunction cutoff is half that of the density cutoff and, therefore, the number of points required to store the wavefunctions is only $\frac{1}{16}$ that required to store the density! [37]

There is, therefore, a substantial cost in both memory and performance due to the fact that the wavefunctions must be represented on the full grid. This feature is unique among the time-evolution schemes described here. Moreover, although the method is unitary and stable, the accuracy of the method is limited, in practice [33], to 4th order.

2.2.7. Short Iterative Lanczos Method

Introduced in 1950, the Lanczos algorithm [38, 39] has been implemented in a variety of fields. Park and Light first applied the Short Iterative Lanczos (SIL) scheme to propagating the TDSE in 1986 [5]. The method takes the form of a polynomial expansion of the exact operator – just as is the case for the Crude Euler or the Chebychev methods (2.59). The basic idea of the SIL method is to create an Arnoldi basis from some finite order Krylov subspace of the Hamiltonian, diagonalize this basis and then propagate the wavefunction in the diagonalized basis. The following derivation follows the convention of Leforestier et al. and Yousef Saad [12, 40].

A Krylov subspace is defined by a vector, ψ, and an operator, $\hat{H}$. Consider the following following set of vectors $\{u_0, u_1, \ldots, u_{N-1}\}$ where the vectors u_j are defined as

$$u_j \equiv \hat{H}^j \psi . \tag{2.81}$$

The subspace spanned by these vectors is an order (N–1) Krylov subspace. In principle, one could project the Hamiltonian directly onto this space, diagonalize the resulting matrix, and propagate the wavefunctions in the new basis.

However, it turns out to be more efficient to form a new basis such that the projection of the Hamiltonian on this new basis is tri-diagonal. Let $\{v_0, v_1, \ldots, v_{N-1}\}$ be a set of vectors that forms a basis such that the projection of the Hamiltonian on this basis is a symmetric tri-diagonal matrix. Note also this basis spans the Krylov subspace of order (N–1). Given v_j, then the projection of the Hamiltonian onto the basis formed by the set of these vectors yields the following tri-diagonal matrix

$$\mathbf{H}_N = \begin{bmatrix} \alpha_0 & \beta_0 & & & & & & \\ \beta_0 & \alpha_1 & \beta_1 & & & & & \\ & \beta_1 & \alpha_2 & \beta_2 & & & & \\ & & \beta_2 & \alpha_3 & \beta_3 & & & \\ & & & \beta_3 & \ddots & & & \\ & & & & & \alpha_{N-3} & \beta_{N-3} & \\ & & & & & \beta_{N-3} & \alpha_{N-2} & \beta_{N-2} \\ & & & & & & \beta_{N-2} & \alpha_{N-1} \end{bmatrix}, \tag{2.82}$$

where the coefficients in the above matrix are given by

$$\begin{aligned} \alpha_j &= \left\langle \upsilon_j \middle| \hat{H} \middle| \upsilon_j \right\rangle \\ \beta_j &= \left\langle \upsilon_j \middle| \hat{H} \middle| \upsilon_{j+1} \right\rangle. \end{aligned} \tag{2.83}$$

The basis $\{\upsilon_0, \upsilon_1, \ldots, \upsilon_{N-1}\}$ and the matrix $\mathbf{H}_N$ are constructed simultaneously and recursively. The zeroth vector in the basis is initialized to be the wavefunction at the current time step

$$\upsilon_0 = \psi(t). \tag{2.84}$$

When applying the Hamiltonian to a vector in this basis one obtains the following relation

$$\hat{H}v_j = \beta_{j-1}\upsilon_{j-1} + \alpha_j \upsilon_j + \beta_j \upsilon_{j+1}, \tag{2.85}$$

where $\beta_{-1} = \beta_N = 0$. The algorithm for constructing the tri-diagonal matrix and basis is given below using (2.83), (2.84), and (2.85)

```
$\upsilon_0 = \psi(t)$
$for \;\; j = 0, \; N$
    $\upsilon_{j+1} = \hat{H}\upsilon_j - \beta_{j-1}\upsilon_{j-1}$
    $\alpha_j = \langle \upsilon_j | \upsilon_{j+1} \rangle$
    $\upsilon_{j+1} = \upsilon_{j+1} - \alpha_j \upsilon_j$
    $\beta_j = \sqrt{\langle \upsilon_{j+1} | \upsilon_{j+1} \rangle}$
    $\upsilon_{j+1} = \frac{\upsilon_{j+1}}{\beta_j}$
$end$
```

(2.86)

Here *N* is the order to which the calculation is allowed to proceed (also determined by the user). The specific criterion for determining *N* is discussed below.

The next step is to diagonalize the projected Hamiltonian tri-diagonal matrix. There are very efficient algorithms available for diagonalizing tri-diagonal matrices (see, e.g. LAPACK [41]). Let $\{w_0, w_1, \ldots, w_{N-1}\}$ be the basis that diagonalizes the tri-diagonal Hamiltonian (2.82).

$$\mathbf{H}_N w_j = \varepsilon_j w_j\,. \tag{2.87}$$

Note that w_j is the j^{th} eigenvector and is of length N and ε_j is the j^{th} eigenvalue. Given that the wavefunction at the current time step is equal to υ_0 (2.84), it is equal to the zero$^{\text{th}}$ element of each of the vectors in the $\{w_0, w_1, \ldots, w_{N-1}\}$ basis,

$$\psi(t) = \sum_{j=0}^{N-1} w_j(0)\,\upsilon_j\,. \tag{2.88}$$

Note that the wavefunction at the current time step is now a linear combination of eigenstates of the Hamiltonian. The wavefunction at the next time step is then simply

$$\psi(t+\Delta) = \sum_{j=0}^{N-1} w_j(0)\,e^{-i\varepsilon_j\Delta}\upsilon_j\,. \tag{2.89}$$

Given a technique for approximating the error, the order of the expansion, N, can be determined during the calculation itself. The error is related to how well the basis spans the space of the time propagator (or perhaps equivalently the propagated wavefunction). The error can then be approximated as the magnitude of the coefficient of the first vector outside of the basis,

$$error \approx \left|w_N(0)\right|. \tag{2.90}$$

Park and Light [5] estimated the error using the following technique. Approximate the propagated wavefunction in the reduced basis with a Taylor series expansion,

$$w(t+\Delta) \approx \sum_{j=0}^{N-1} \frac{(-i\Delta)^j}{j!}\{\mathbf{H}_N\}^j\, w(t)\,. \tag{2.91}$$

Given that H_N is a tri-diagonal matrix, the magnitude of the N^{th} component can be approximated by the following expression

$$w_N(0) \approx \frac{(-i\Delta)^{N-1}}{(N-1)!} \prod_{j=0}^{N-1} \beta_j \,, \tag{2.92}$$

where β_j are the off-diagonal elements of the reduced Hamiltonian, (2.82). One may use (2.92) as an error estimate to determine the order of the expansion, i.e., exit the loop in (2.86) when the error estimate given above is below some threshold.

The SIL method is unitary by construction. Moreover, it is unconditionally stable. The accuracy of the method is determined by a user-defined error tolerance. Often one chooses the error tolerance to be small compared to the machine precision. The efficiency of the SIL method is related to the number of $\hat{H}\psi$ operations (i.e. the order, N, of the approximation). It has been reported that the number of $\hat{H}\psi$ operations to achieve an arbitrary accuracy is typically less than for a Chebychev expansion [12, 42]. On the other hand, the SIL method is not very memory efficient. It is necessary to have N wavefunction-sized data structures for an order N SIL expansion.

2.2.8 Remarks and Conclusions

We found that only the Chebychev and SIL methods were able to achieve an acceptable balance of accuracy and efficiency. For typical applications, we generally used the Chebychev method when the calculation was memory limited and the SIL method when memory was not a constraint.

2.3. Freespace Boundary Conditions

2.3.1. Introduction

When performing calculations using a plane-wave basis, the boundary conditions are periodic. For systems where periodicity is not desired (e.g. isolated molecules, slab calculations etc…), it is still possible to use a plane-wave basis using a method first described by Hockney [43, 44, 45]. The so-called "Hockney Method" explicitly removes any long-range contribution from neighboring image cells. For a Hamiltonian in a typical norm-conserving pseudopotential DFT calculation, only the Hartree potential and the ion potential are long range (i.e. the Coulomb terms). The remaining terms in the Hamiltonian are local in real space and therefore do not contribute to neighboring cells.

There have been several excellent reviews [46, 47, 48, 49] of Hockney-like methods for implementing freespace boundary conditions in a plane-wave code. The following derivation follows these conventions of these reviews.

2.3.2. Hartree Potential

One may use a dual-space calculation to solve Poisson's Equation for the Hartree potential using the convolution theorem. Poisson's Equation in differential form is

$$\nabla^2 \upsilon_H = -4\pi\rho \,, \tag{2.93}$$

where υ_H is the Hartree potential and ρ is the charge density. The solution to this equation has the form:

$$\upsilon_H(\mathbf{r}) = \int\limits_{\substack{all\\space}} d\mathbf{r}' \, \rho(\mathbf{r}') \, g(\mathbf{r}-\mathbf{r}') \,, \tag{2.94}$$

where g is the Green's function kernel for the Poisson Equation:

$$g(\mathbf{r}) = \frac{1}{|\mathbf{r}|}. \tag{2.95}$$

The convolution theorem (a.k.a. the Faltung theorem), states that any equation of the form shown in (2.94) in real space has the following simple form in reciprocal space

$$\tilde{\upsilon}_H(\mathbf{G}) = \tilde{\rho}(\mathbf{G})\,\tilde{g}(\mathbf{G}). \tag{2.96}$$

Periodic boundary conditions are implicitly enforced for any function that is represented in a plane-wave basis. Therefore, in order to perform a dual-space calculation without periodic boundary conditions, one must extend the supercell and modify the Green's function kernel. Assume that the original supercell, Ω, is cubic and of length L on a side. The new supercell, Ω′, contains the original supercell and is of length $2L$ on a side. It is assumed that the density is zero everywhere outside of Ω and therefore the density is set to zero everywhere outside of Ω. The non-periodicity is then enforced by modifying the Green's Function kernel so that it is strictly zero except when its two points both lie

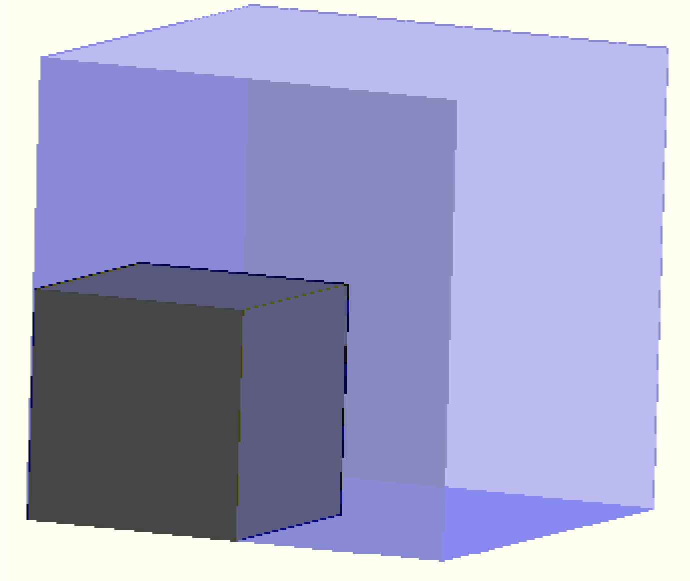

Figure 2.2: Original and Extended Supercells

inside of Ω'.

$$g(\mathbf{r}-\mathbf{r}')=\begin{cases}\dfrac{1}{|\mathbf{r}-\mathbf{r}'|} & , \ \mathbf{r}-\mathbf{r}'\in\Omega' \\ 0 & , \ else\end{cases} \tag{2.97}$$

This scheme is sometimes referred to as the finite Coulomb tail method because the Coulomb tail is abruptly set to zero outside Ω'. The analytic transform of this equation is given by:

$$\tilde{g}(\mathbf{G})=\int_{\Omega'} d\mathbf{r}\,\frac{e^{-i\mathbf{G}\cdot\mathbf{r}}}{r}. \tag{2.98}$$

It is possible to evaluate this integral numerically but the singularity at the origin requires special treatment in order to get sufficient accuracy. Instead, the region of integration, Ω', is broken up into two parts: inside and outside a sphere inscribed in Ω' (see Figure 2.3),

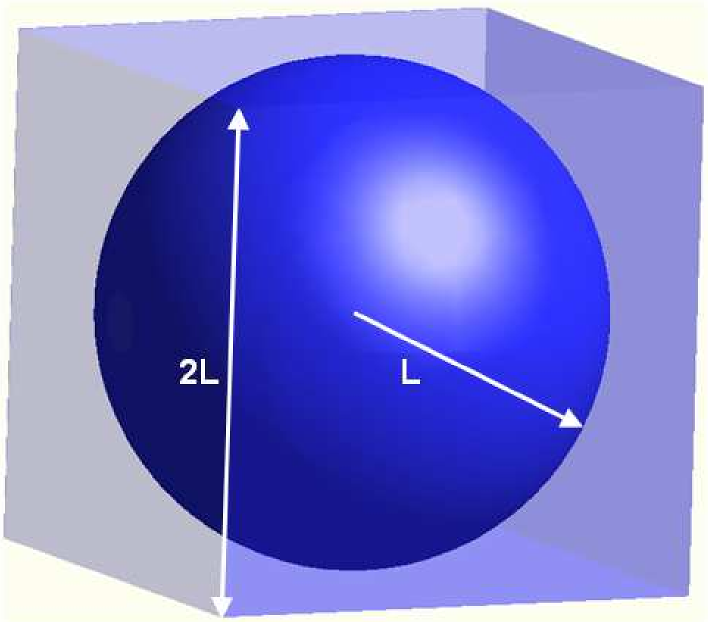

Figure 2.3: There are two regions of integration: inside the sphere inscribed inside the box and outside the sphere but inside the box

$$\tilde{g}(\mathbf{G}) = \int_{\substack{inside\\ sphere}} d\mathbf{r}\,\frac{e^{-i\mathbf{G}\cdot\mathbf{r}}}{r} + \int_{\substack{outside\\ sphere}} d\mathbf{r}\,\frac{e^{-i\mathbf{G}\cdot\mathbf{r}}}{r}. \tag{2.99}$$

Note that the total region of integration is a box is of length $2L$ on a side. The sphere inscribed inside this box has a radius of length L.

Assuming that the big supercell is chosen so that the origin is at the center of the box (and thus the sphere), the integral over the inside of the sphere can be evaluated analytically using spherical coordinates.

$$\tilde{g}_{in}(\mathbf{G}) = \int_0^{2\pi} d\phi \int_0^L dr\, r^2 \int_0^{\pi} d\theta \sin\theta\, \frac{e^{-i\mathbf{G}\cdot\mathbf{r}}}{r}. \tag{2.100}$$

Since this region is centro-symmetric, the axes of integration are arbitrary and one may always orient the axes so that $\mathbf{G} = G\,\hat{z}$ and therefore $\mathbf{G}\cdot\mathbf{r} = Gr\cos\theta$

$$\tilde{g}_{in}(\mathbf{G}) = 2\pi \int_0^L dr\, r \int_0^{\pi} d\theta \sin\theta\, e^{-iGr\cos\theta}. \tag{2.101}$$

Evaluate the integral over the polar angle,

$$\int_0^{\pi} d\theta \sin\theta\, e^{-iGr\cos\theta} = \left.\frac{e^{-iGr\cos\theta}}{iGr}\right|_0^{\pi} = \frac{1}{iGr}\left(e^{iGr} - e^{-iGr}\right) = \frac{2\sin(Gr)}{Gr}. \tag{2.102}$$

Finally, evaluate the radial integral ,

$$\tilde{g}_{in}(\mathbf{G}) = \frac{4\pi}{G}\int_0^L dr\, \sin(Gr) = -\frac{4\pi}{G^2}\cos(Gr)\Big|_0^L = \frac{4\pi}{G^2}\left[1 - \cos(GL)\right]. \tag{2.103}$$

The integral over the region outside the sphere, $\tilde{g}_{out}(\mathbf{G})$, is calculated numerically by simple quadrature:

$$\tilde{g}_{out}(\mathbf{G}) = \Delta \sum_{\mathbf{r}_{out}} \frac{\exp(-i\mathbf{G}\cdot\mathbf{r}_{out})}{r_{out}}, \tag{2.104}$$

where r_{out} are the grid points that lie outside of the sphere and Δ is the volume of the of a single volume element,

$$\Delta = \frac{\Omega}{N}, \tag{2.105}$$

where Ω is the total volume of the simulation cell and N is the total number of grid points.

2.3.3. The Local Pseudopontial

The Norm Conserving Pseudopotential (NCP) treatment of the ion-electron interaction implemented in many DFT codes uses the Kleinmann Bylander formalism for separable nonlocal pseudopotentials. For a default periodic calculation, the local pseudopotential is handled in the following manner. First, an analytic expression for the local pseudopotential in reciprocal space can be used to tabulate the local pseudopotential on a reciprocal space grid. The reciprocal space expression for the local pseudopotential due to atom α is given by:

$$\tilde{\upsilon}_{loc}^{\alpha}(\mathbf{G}) = \tilde{\upsilon}_{tail}^{\alpha}(\mathbf{G}) + \tilde{\upsilon}_{tab}^{\alpha}(\mathbf{G}), \tag{2.106}$$

where $\tilde{\upsilon}_{tail}$ is an analytic term that describes the long range (in real space) contribution

$$\tilde{\upsilon}_{tail}^{\alpha}(\mathbf{G}) = \begin{cases} \dfrac{\pi Z_{\alpha} e^2}{\Omega a} & ,G = 0 \\ \dfrac{-4\pi Z_{\alpha} e^2}{\Omega} \dfrac{\exp\left(-\dfrac{G^2}{4a}\right)}{G^2} & ,G > 0, \end{cases} \tag{2.107}$$

where Ω is the volume of the supercell, Z_{α} is the net charge of the core electrons plus the nucleus of atom α, and e^2 is the square of the elementary charge. The constant a is determined by the user. The second term in (2.106), $\tilde{v}_{tab}$, is the tabulated contribution to the local pseudopotential.

$$\tilde{v}_{tab}^{\alpha}(\mathbf{G}) = \frac{1}{\Omega}\sum_{i} v_{tab}^{\alpha}(r_i)\, j_0(Gr_i)\,, \tag{2.108}$$

where v_{tab}^{α} is a tabulated radial function read in from the pseudopotential file. Finally, j_0 is a Bessel function of the first kind.

The total local potential is calculated by summing the translated local potential of each atom and applying the translation operator in order to center the local pseudopotential at the position of the atom:

$$\tilde{v}_{loc}(\mathbf{G}) = \sum_{\alpha} \tilde{v}_{loc}^{\alpha}(\mathbf{G})\, e^{-i\mathbf{G}\cdot\mathbf{R}_{\alpha}}\,, \tag{2.109}$$

where R_{α} is the position of atom α. Since $\tilde{v}_{loc}$ is a diagonal operator in real space, the local potential is FFT'd to real space and added to the total potential. It should be noted that by performing a discrete Fourier transform from a grid that only contains reciprocal lattice vectors of the supercell, the periodic images of the potential are automatically aliased into the real space representation. This is an artifact of the transform that enforces periodic boundary conditions.

2.3.4. Freespace Local Potential

In order to perform a calculation that has free space boundary conditions, one must remove the contribution from images of the local potentials in other supercells. The easiest way to do this is to simply tabulate the local pseudopotentials of the atoms in the original supercell (i.e. not in neighboring image supercells) on the real space grid directly without transforming from reciprocal space. An analytic expression for the tail portion of the local potential (2.107) in real space is then needed so as to be able to tabulate the local potential directly on the real space grid.

To find an analytic expression for $\tilde{v}_{tail}$ for atom α in real space, transform (2.107) to real space. One may use the convolution theorem to derive an expression for this term in real space. The convolution theorem guarantees that a product of two functions in reciprocal space corresponds to a convolution of those two functions in real space:

$$\tilde{S}(\mathbf{G}) = \tilde{P}(\mathbf{G})\tilde{Q}(\mathbf{G}) \quad \Leftrightarrow \quad s(\mathbf{r}) = \int p(\mathbf{r}')q(\mathbf{r}-\mathbf{r}')d\mathbf{r}'. \tag{2.110}$$

One may rewrite $\tilde{v}_{tail}$ as:

$$\tilde{v}^{\alpha}_{tail}(\mathbf{G}) = \tilde{P}(\mathbf{G})\tilde{Q}(\mathbf{G}), \tag{2.111}$$

where

$$\begin{aligned} \tilde{P}(\mathbf{G}) &\equiv -\frac{4\pi}{G^2} \\ \tilde{Q}(\mathbf{G}) &\equiv Z_\alpha e^2 \exp\left(-\frac{G^2}{4a}\right). \end{aligned} \tag{2.112}$$

Note that the factor of $\frac{1}{\Omega}$ has been removed since the transform takes place by integrating over all space and not just the volume of the supercell. The transform of P is well-known as it is the Green's function kernel for the 1/r operator

$$p(\mathbf{r}) = (2\pi)^{-3}\int d\mathbf{G}\left(-\frac{4\pi}{G^2}\right)e^{-i\mathbf{G}\cdot\mathbf{r}} = \frac{1}{r}. \tag{2.113}$$

The transform of Q, which is Gaussian, is given by

$$q(\mathbf{r}) = (2\pi)^{-3}\int d\mathbf{G}\left[Z_\alpha e^2 \exp\left(-\frac{G^2}{4a}\right)\right]\exp(i\mathbf{G}\cdot\mathbf{r}) = Z_\alpha e^2\left(\frac{a}{\pi}\right)^{\frac{3}{2}}\exp\left(-ar^2\right). \tag{2.114}$$

Employing the convolution theorem, V_{tail} in real space may be written as

$$\upsilon_{tail}^{\alpha}(\mathbf{r}) = Z_\alpha e^2 \left(\frac{a}{\pi}\right)^{\frac{3}{2}} \int d\mathbf{r}' \frac{\exp\left[-a\left|\mathbf{r}-\mathbf{r}'\right|^2\right]}{r'}. \tag{2.115}$$

To evaluate this expression, use the law of cosines and evaluate the integral in spherical coordinates:

$$\begin{aligned}
v_{tail}^{\alpha}(\mathbf{r}) &= Z_\alpha e^2 \left(\frac{a}{\pi}\right)^{\frac{3}{2}} 2\pi \int_0^{\infty} dr'\, r'^2 \int_0^{\pi} d\theta \sin\theta \frac{\exp\left[-a\left(r^2 + r'^2 - 2rr'\cos\theta\right)\right]}{r'} \\
&= 2\pi Z_\alpha e^2 \left(\frac{a}{\pi}\right)^{\frac{3}{2}} \exp\left(-ar^2\right) \int_0^{\infty} dr'\, r' \exp\left(-ar'^2\right) \int_1^{-1} dx \exp\left(2arr'x\right) \\
&= -2\pi Z_\alpha e^2 \left(\frac{a}{\pi}\right)^{\frac{3}{2}} \frac{\exp\left(-ar^2\right)}{ar} \int_0^{\infty} dr' \exp\left(-ar'^2\right) \sinh\left(2arr'\right) \\
&= -2Z_\alpha e^2 \sqrt{\frac{a}{\pi}} \frac{\exp\left(-ar^2\right)}{r} \left(\frac{1}{2}\sqrt{\frac{\pi}{a}} \exp\left(ar^2\right) erf\left(r\sqrt{a}\right)\right) \\
&= -Z_\alpha e^2 \frac{erf\left(r\sqrt{a}\right)}{r}.
\end{aligned} \tag{2.116}$$

Next the tabulated portion of the local potential, V_{tab}, is placed on a real space grid. This term depends on a function that is tabulated on a radial grid in real space but not at the grid points of the supercell. King-Smith, Payne, and Lin [50] showed that the most accurate way to interpolate such a function onto a grid for a dual-space calculation is by transforming to a reciprocal space grid that is double the size (in each dimension). If the original real-space grid is a cube of length L on a side (with volume L^3) and has N points in each direction (N^3), then the grid to which (2.108) will be tabulated will be a cube of length $2L$ on a side with $2N$ points in each direction. The corresponding reciprocal space grids will have the same frequency cutoff but the sampling rate of the bigger grid will be double that of the original reciprocal space grid. The reciprocal space representation of the tabulated portion of the local potential on the large grid is transformed to real space via the inverse Fourier transform

$$v_{tab}^{\alpha}(\mathbf{r}) = \int d\mathbf{G}\, \tilde{v}_{tab}^{\alpha}(\mathbf{G})\, e^{i\mathbf{G}\cdot(\mathbf{r}-\mathbf{R}_{\alpha})} \, . \tag{2.117}$$

Notice that unlike the case for the tail potential, the expression above for the tabulated potential already has the potentials centered correctly on the atom positions. The next and final step is to transform this potential back to real space and add it to the total local potential,

$$v_{loc}(\mathbf{r}) = \sum_{\alpha} \left[v_{tail}^{\alpha}(\mathbf{r}-\mathbf{R}_{\alpha}) + v_{tab}^{\alpha}(\mathbf{r}) \right] . \tag{2.118}$$

2.3.5. Freespace Local Pseudopotential Forces

The next step is to derive expressions for the force on the nuclei due to the local pseudopotentials. From the Helmann-Feynman force theorem we have the following expression for the force on nucleus α due to the local pseudopotential:

$$\mathbf{F}_{loc}^{\alpha} = -\int_{\Omega} d\mathbf{r}\, n(\mathbf{r}) \frac{\partial v_{loc}(\mathbf{r})}{\partial \mathbf{R}_{\alpha}} , \tag{2.119}$$

where $n(\mathbf{r})$ is the electron density. In a discrete calculation, the integral becomes a sum

$$\mathbf{F}_{loc}^{\alpha} = -\sum_{\mathbf{r}} \Delta\, n(\mathbf{r}) \frac{\partial v_{loc}(\mathbf{r})}{\partial \mathbf{R}_{\alpha}} , \tag{2.120}$$

where $\Delta \equiv \Omega / N$ is the volume of each volume element and N is the number of grid points in the supercell. The force on a given atom can written as the sum of contributions from the tail and tabulated forces corresponding to the tail and tabulated contributions to the local potential defined in (2.118)

$$\mathbf{F}_{loc}^{\alpha} = \mathbf{F}_{tail}^{\alpha} + \mathbf{F}_{tab}^{\alpha}. \tag{2.121}$$

The tail force, $\mathbf{F}_{tail}^{\alpha}$, is given by:

$$\mathbf{F}_{tail}^{\alpha} = -\Delta \sum_{\mathbf{r}} n(\mathbf{r}) \frac{\partial}{\partial \mathbf{R}_{\alpha}} \sum_{\alpha'} \upsilon_{tail}^{\alpha'}(\mathbf{r} - \mathbf{R}_{\alpha'}). \tag{2.122}$$

Clearly, the partial derivative collapses the sum over α'. Substituting (2.116) into (2.122) yields:

$$\begin{aligned} \mathbf{F}_{tail}^{\alpha} &= Z_{\alpha} e^{2} \Delta \sum_{\mathbf{r}} n(\mathbf{r}) \frac{\partial}{\partial \mathbf{R}_{\alpha}} \frac{\operatorname{erf}\left(\sqrt{a}\left|\mathbf{r}-\mathbf{R}_{\alpha}\right|\right)}{\left|\mathbf{r}-\mathbf{R}_{\alpha}\right|} \\ &= Z_{\alpha} e^{2} \Delta \sum_{\mathbf{r}} n(\mathbf{r}) \left[-2\sqrt{\frac{a}{\pi}} \frac{\exp\left(-a\left|\mathbf{r}-\mathbf{R}_{\alpha}\right|^{2}\right)}{\left|\mathbf{r}-\mathbf{R}_{\alpha}\right|^{2}} + \frac{\operatorname{erf}\left(\sqrt{a}\left|\mathbf{r}-\mathbf{R}_{\alpha}\right|\right)}{\left|\mathbf{r}-\mathbf{R}_{\alpha}\right|^{3}} \right] (\mathbf{r}-\mathbf{R}_{\alpha}). \end{aligned} \tag{2.123}$$

In the limit as the $\left|\mathbf{r}-\mathbf{R}_{\alpha}\right| \rightarrow 0$, the quantity in brackets times (r – R$_{\alpha}$) vanishes

$$\mathbf{F}_{tail}^{\alpha} = \begin{cases} 0 & , \left|\mathbf{r}-\mathbf{R}_{\alpha}\right| = 0 \\ Z_{\alpha} e^{2} \Delta \sum_{\mathbf{r}} n(\mathbf{r}) \left[-2\sqrt{\frac{a}{\pi}} \frac{\exp\left(-a\left|\mathbf{r}-\mathbf{R}_{\alpha}\right|^{2}\right)}{\left|\mathbf{r}-\mathbf{R}_{\alpha}\right|^{2}} + \frac{\operatorname{erf}\left(\sqrt{a}\left|\mathbf{r}-\mathbf{R}_{\alpha}\right|\right)}{\left|\mathbf{r}-\mathbf{R}_{\alpha}\right|^{3}} \right] (\mathbf{r}-\mathbf{R}_{\alpha}) & , \left|\mathbf{r}-\mathbf{R}_{\alpha}\right| > 0. \end{cases} \tag{2.124}$$

The tabulated force, $\mathbf{F}_{tab}^{\alpha}$, is given by

$$\begin{aligned} \mathbf{F}_{tab}^{\alpha} &= -\Delta \sum_{\mathbf{r}} n(\mathbf{r}) \frac{\partial}{\partial \mathbf{R}_{\alpha}} \sum_{\alpha'} \upsilon_{tab}^{\alpha'}(\mathbf{r}) \\ &= -\Delta \sum_{\mathbf{r}} n(\mathbf{r}) \frac{\partial}{\partial \mathbf{R}_{\alpha}} \sum_{\alpha'} \int d\mathbf{G}\, \tilde{\upsilon}_{tab}^{\alpha'}(\mathbf{G}) e^{i\mathbf{G}\cdot(\mathbf{r}-\mathbf{R}_{\alpha'})}. \end{aligned} \tag{2.125}$$

As was the case for the tail force, the sum over the atoms in the expression above

$$\mathbf{F}_{tab}^{\alpha} = -\Delta \sum_{\mathbf{r}} n(\mathbf{r}) \frac{\partial}{\partial \mathbf{R}_{\alpha}} \int d\mathbf{G}\, \tilde{\upsilon}_{tab}^{\alpha}(\mathbf{G}) e^{i\mathbf{G}\cdot(\mathbf{r}-\mathbf{R}_{\alpha})}. \tag{2.126}$$

Applying the partial derivative yields:

$$\mathbf{F}_{tab}^{\alpha} = \Delta \sum_{\mathbf{r}} n(\mathbf{r}) \int d\mathbf{G}\, i\mathbf{G}\, \tilde{\upsilon}_{tab}^{\alpha}(\mathbf{G}) e^{i\mathbf{G}\cdot(\mathbf{r}-\mathbf{R}_{\alpha})}. \tag{2.127}$$

For a discrete calculation, the inverse fourier transform above is a discrete inverse Fourier transform,

$$\mathbf{F}_{tab}^{\alpha} = \Delta \sum_{\mathbf{r}} n(\mathbf{r}) \sum_{\mathbf{G}} i\mathbf{G}\, \tilde{v}_{tab}^{\alpha}(\mathbf{G}) e^{i\mathbf{G}\cdot(\mathbf{r}-\mathbf{R}_{\alpha})} . \tag{2.128}$$

Substituting the Fourier transform of the electron density yields:

$$\mathbf{F}_{tab}^{\alpha} = \Delta \sum_{\mathbf{r}} \sum_{\mathbf{G}'} \tilde{n}(\mathbf{G}') e^{i\mathbf{G}'\cdot\mathbf{r}} \sum_{\mathbf{G}} i\mathbf{G}\, \tilde{v}_{tab}^{\alpha}(\mathbf{G}) e^{i\mathbf{G}\cdot(\mathbf{r}-\mathbf{R}_{\alpha})} . \tag{2.129}$$

Rearranging the sums yields:

$$\mathbf{F}_{tab}^{\alpha} = \Delta \sum_{\mathbf{G}\mathbf{G}'} \tilde{n}(\mathbf{G}') i\mathbf{G}\, \tilde{v}_{tab}^{\alpha}(\mathbf{G}) e^{-i\mathbf{G}\cdot\mathbf{R}_{\alpha}} \sum_{\mathbf{r}} e^{i(\mathbf{G}+\mathbf{G}')\cdot\mathbf{r}} . \tag{2.130}$$

Using the identity $\sum_{\mathbf{r}} e^{i(\mathbf{G}+\mathbf{G}')\cdot\mathbf{r}} = N\delta_{-\mathbf{G},\mathbf{G}'}$ leaves

$$\mathbf{F}_{tab}^{\alpha} = \Delta \sum_{\mathbf{G}\mathbf{G}'} \tilde{n}(\mathbf{G}') i\mathbf{G}\, \tilde{v}_{tab}^{\alpha}(\mathbf{G}) e^{-i\mathbf{G}\cdot\mathbf{R}_{\alpha}} \left(N\delta_{-\mathbf{G},\mathbf{G}'}\right) . \tag{2.131}$$

Since v_{tab}^{α} is a radial function, $\tilde{v}_{tab}^{\alpha}(-\mathbf{G}) = \tilde{v}_{tab}^{\alpha}(\mathbf{G})$

$$\mathbf{F}_{tab}^{\alpha} = -\Omega \sum_{\mathbf{G}} \tilde{n}(\mathbf{G}) i\mathbf{G}\, \tilde{v}_{tab}^{\alpha}(\mathbf{G}) e^{i\mathbf{G}\cdot\mathbf{R}_{\alpha}} . \tag{2.132}$$

The force is a real quantity, therefore one may rewrite the above expression using the following identity for some complex number c, $\mathrm{Re}[ic] = -\mathrm{Im}[c]$

$$\mathbf{F}_{tab}^{\alpha} = \Omega \sum_{\mathbf{G}} \mathrm{Im}\left[\tilde{n}(\mathbf{G}) \tilde{v}_{tab}^{\alpha}(\mathbf{G}) e^{i\mathbf{G}\cdot\mathbf{R}_{\alpha}}\right] \mathbf{G} . \tag{2.133}$$

2.3.6. Remarks and Conclusions

We use freespace boundary conditions for applications where the long range Coulomb interactions from neighboring cells have a non-negligible effect on the calculation. For example, consider the groundstate of a diatomic molecule in the presence of a constant electric field. The electrons will respond by shifting and a dipole will form. The long range tail of a dipole falls off as $\frac{1}{r^3}$. With periodic boundary conditions, one must choose the dimensions of the simulation cell so that the potential from neighboring cells effectively vanishes. However, with the freespace method described above, one may still use a dual-space planewave basis and choose the dimensions of the simulation cell to only be large enough that the density of the electrons vanishes at the boundaries (not the potential).

2.4. References

[1] E.A. McCullough, Jr. and R.E. Wyatt, *J. Chem. Phys.* **51**, 1253 (1969).

[2] E.A. McCullough, Jr. and R.E. Wyatt, *J. Chem. Phys.* **54**, 3592 (1971).

[3] H. Tal-Ezer and R. Kosloff, *J. Chem. Phys.* **81**, 3967 (1984).

[4] A. Askar and A.S. Cakmak, *J. Chem. Phys.* **68**, 2794 (1978).

[5] T.J. Park and J.C. Light, *J. Chem. Phys.* **85**, 5870 (1986).

[6] M.D. Feit and J.A. Fleck, Jr., *Applied Optics*, **17**, 3990 (1978).

[7] T. Iitaka, *Phys. Rev. E.* **49**, 4684 (1994).

[8] A. Goldberg, H.M. Schey, and J.L. McCullough, Jr. and R.E. Wyatt, *J. Chem. Phys.* **51**, 1253 (1969).

[8] E.A. McCullough, Jr. and R.E. Wyatt, *J. Chem. Phys.* **54**, 3592 (1971).

[8] H. Tal-Ezer and R. Kosloff, *J. Chem. Phys.* **81**, 3967 (1984).

[8] A. Askar and A.S. Cakmak, *J. Chem. Phys.* **68**, 2794 (1978).

[8] T.J. Park and J.C. Light, *J. Chem. Phys.* **85**, 5870 (1986).

[8] M.D. Feit and J.A. Fleck, Jr., *Applied Optics*, **17**, 3990 (1978).

[8] T. Iitaka, *Phys. Rev. E.* **49**, 4684 (1994).Schwartz, *Am. J. Phys.* **35**, 177 (1967).

[9] W.H. Press, S.A. Teukolsky, W.T. Vetterling and B.P. Flannery. *Numerical Recipes in C.* Cambridge University Press, Cambridge, 1992.

[10] M.W. Choptuik, personal communication to the Binary Black Hole Grand Challenge Alliance (1996).

[11] S.A. Teukolsky. *Phys. Rev. D.* **61**. 87501 (2000).

[12] C. Leforestier, et al., *J. Comput. Phys.* **94**, 59 (1991).

[13] M.D. Feit and J.A. Fleck, Jr., *Applied Optics*, **18**, 2843 (1979).

[14] M.D. Feit and J.A. Fleck, Jr., *Applied Optics*, **19**, 1154 (1980).

[15] M.D. Feit and J.A. Fleck, Jr., *Applied Optics*, **19**, 2240 (1980).

[16] M.D. Feit and J.A. Fleck, Jr., *Applied Optics*, **19**, 3140 (1980).

[17] M.D. Feit and J.A. Fleck, Jr. *J Chem Phys*, **78**, 301 (1982).

[18] M.D. Feit, J.A. Fleck, Jr. and A. Steiger, *J Comput Phys*, **47**, 412 (1982).

[19] H.F. Trotter, *Proc Ann Math Soc*, **10**, 545 (1959).

[20] This can be shown by Taylor expanding the exponentials and noting that if the terms constituent operators commute, one may split the operators an arbitrary number of times and the expression will remain exact. That is, if $\left[\hat{A},\hat{B}\right]=0$, then $e^{a\left(\hat{A}+\hat{B}\right)}=e^{a\hat{A}}e^{a\hat{B}}=e^{a\hat{B}}e^{a\hat{A}}=e^{\frac{a}{2}\hat{B}}e^{\frac{a}{2}\hat{A}}e^{\frac{a}{2}\hat{B}}e^{\frac{a}{2}\hat{A}}=\ldots$

[21] M. Suzuki, *Commun Math Phys*, **51**, 183 (1976).

[22] M. Suzuki, S. Miyashita, and A. Kuroda, *Prog Theor Phys*, **58**, 1377 (1977).

[23] M. Suzuki, *J Math Phys*, **32**, 400 (1991).

[24] N. Hatano and M. Suzuki, *Prog Theor Phys*, **85**, 481 (1991).

[25] M. Suzuki, *J Phys Soc Jpn*, **61**, L3015 (1992).

[26] M. Suzuki and T. Yamauchi, *J Math Phys*, **34**, 4892 (1993).

[27] D Vanderbilt, *Phys Rev B*. **41** (Rapid Communications), 7892 (1990).

[28] K. Laasonen, R. Car, C. Lee, and D. Vanderbilt, *Phys Rev B*, **43** (Rapid Communications), 6796 (1991).

[29] K. Laasonen, A. Pasquarello, C. Lee, R. Car, and D. Vanderbilt, *Phys Rev B*, **47**, 10142 (1993).

[30] P.E. Blöchl, *Phys Rev B* **50**, 17953 (1994).

[31] L. Kleinmann and D.M. Bylander, *Phys Rev Lett* **48** 1425 (1982).

[32] J. Theilhaber, *Phys Rev B*, **46** 12990 (1992).

[33] O. Sugino and Y. Miyamoto, *Phys Rev B*, **59** 2579 (1999).

[34] H. Akima, *J Assoc Comput Mach*, **17** 589 (1970).

[35] Y. Miyamoto, personal communication to the author (2003).

[36] To show this, let $\psi = \sin(kx)$, then in order to represent this function, one needs a grid with a maximum frequency, $f_{\psi}^{\max} \geq 2\pi k$. The density corresponding to this wavefunction is $n = \psi^{*}\psi = \sin^{2}(kx) = \frac{1}{2}\left[1-\cos(2kx)\right]$. Note that the maximum frequency required to represent this function is given by $f_{n}^{\max} \geq 4\pi k$. Therefore $f_{n}^{\max} = 2 f_{\psi}^{\max}$.

[37] Many implementation only keep the components of the reciprocal space representation of the density that lie within the sphere inscribed in the grid. This allows one to apply FFT routines that are optimized for such data layouts. However, even for this case, the number of points used to represent the density in a typical calculation is still 8 times that required to represent the wavefunctions in reciprocal space.

[38] C.J. Lanczos, *J Res Natl Bur Stand*, **45** 255 (1950).

[39] R. Haydock, *Solid State Phys*, **35** 216 (1980).

[40] Y. Saad, *Iterative Methods for Sparse Linear Systems (2nd Edition)*, Society for Industrial and Applied Mathematics (SIAM), Philadelphia (2003).

[41] http://www.netlib.org/lapack/lug/index.html

[42] A. Castro, M.A.L. Marques, and A. Rubio, *J Chem Phys*, **121** 3425 (2004).

[43] R.W. Hockney, *Methods Comput Phys*. **9** 135 (1970).

[44] J.W. Eastwood and D.R.K. Brownrigg, *J Comput Phys*, **32** 24 (1979).

[45] R.W. Hockney and J.W. Eastwood, *Computer Simulations Using Particles*. McGraw-Hill, New York, 1981.

[46] A. Castro, A. Rubio, and M.J. Stott, *Can J Phys*. **81** 1151 (2003).

[47] G.J. Martyna and M.E. Tuckerman, *J Chem Phys*. **110** 2810 (1999).

[48] M.R. Jarvis, I.D. White, R.W. Godby, and M.C. Payne, *Phys Rev B*, **56** 14972 (1997).

[49] R.N. Barnett and U. Landman, *Phys Rev B*. **48** 2081 (1993).

[50] R.D. King-Smith, M.C. Payne, and J.S. Lin, *Phys Rev B*, **44** 13063 (1991).

CHAPTER III

DYNAMICAL EFFECTS IN THE INTERACTION OF ENERGETIC IONS AND MATTER

3.1. Introduction

The behavior of ions moving through materials is of significant interest in several disciplines of physics (particle, nuclear, condensed matter), materials science (radiation damage in devices, ion implantation for fabrication) and medicine (diagnostic and therapeutic radiology). Interest in this topic began at least a century ago with the discovery of radioactivity. Marie Curie suggested that alpha rays were particles that were likely to lose speed in matter:

> Les rayons alpha sont des projectiles materials susceptibles de perdre de leur vitesse en traversant la matiere. [1]

The stopping power (SP), *S*, defined as the mean energy lost by the ion per unit path length, is a key quantity that characterizes the process of an ion traveling through matter

$$S = -\frac{dE}{dx} \tag{3.1}$$

(this quantity is actually the stopping force, but it is historically called the stopping power). For example, the SP can be used to estimate the damage along an ion track in some material or determine how long an ion will travel through a material before it is captured. The fluctuation of the SP is referred to as energy-loss straggling. The range of an ion at a certain energy is defined as the penetration depth with its fluctuation referred to as range straggling.

Historically, different theories were developed to treat specific energy ranges, projectile types, material types etc… (see [2, 3, 4] for excellent reviews of the various theories of ion radiation in materials). When differentiating by the energy of the projectile, there are three energy regimes for the ion – slow, intermediate and swift. An ion is considered "slow" if its velocity is smaller than the velocity of the valence electrons in the material. The velocity of valence electrons in materials is approximately the Bohr velocity, $\upsilon_0 \equiv \alpha c \approx 2.2\times 10^8\, cm\, s^{-1}$. Alternatively, in terms of energy, an ion is slow if $E < 25\frac{keV}{amu}$. A "swift" or "fast" ion has a velocity $\upsilon > \upsilon_0 Z_1^{\frac{2}{3}}$, where Z_1 is the nuclear charge of the projectile ion [5]. An "intermediate" ion has a velocity in the range $\upsilon_0 < \upsilon < \upsilon_0 Z_1^{\frac{2}{3}}$.

The projectile ions can be further classified by weight. Hydrogen, helium, and lithium are considered "light ions" and ions with Z>3 are considered to be "heavy ions". This particular classification is not absolute – however, it is commonly accepted in the ion radiation literature.

The target material can be differentiated by the species of atoms as well as the phase (i.e. gas, liquid, solid). If the target material is a solid, then it can be further differentiated as amorphous or crystalline. Figs. 3.1 and 3.2 show examples of amorphous silicon and crystalline silicon, respectively.

We will use TDDFT to model the SP of slow heavy ions that are channeled through a silicon crystal (see Fig. 3.2).

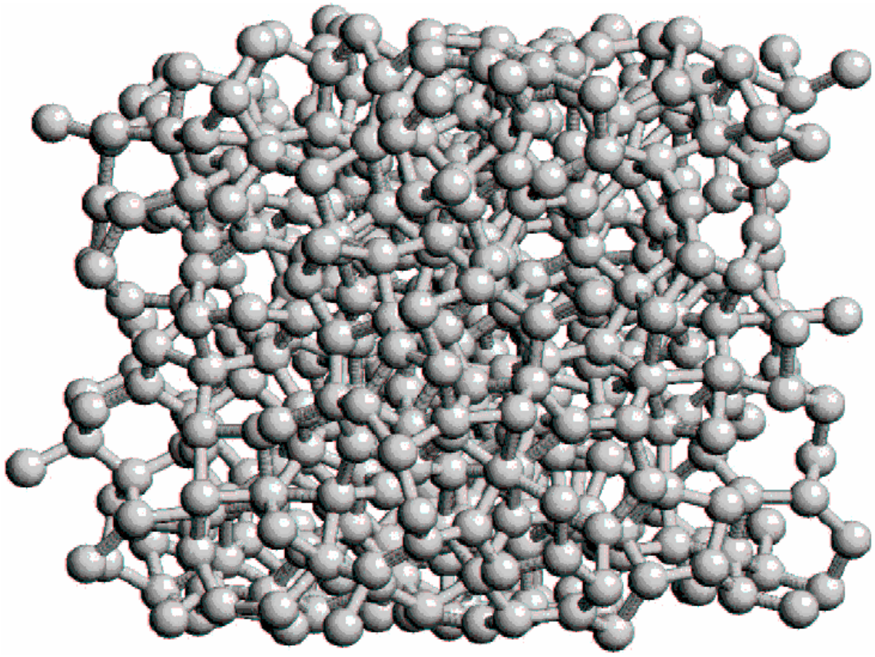

Figure 3.1: Example of amorphous Silicon [3]

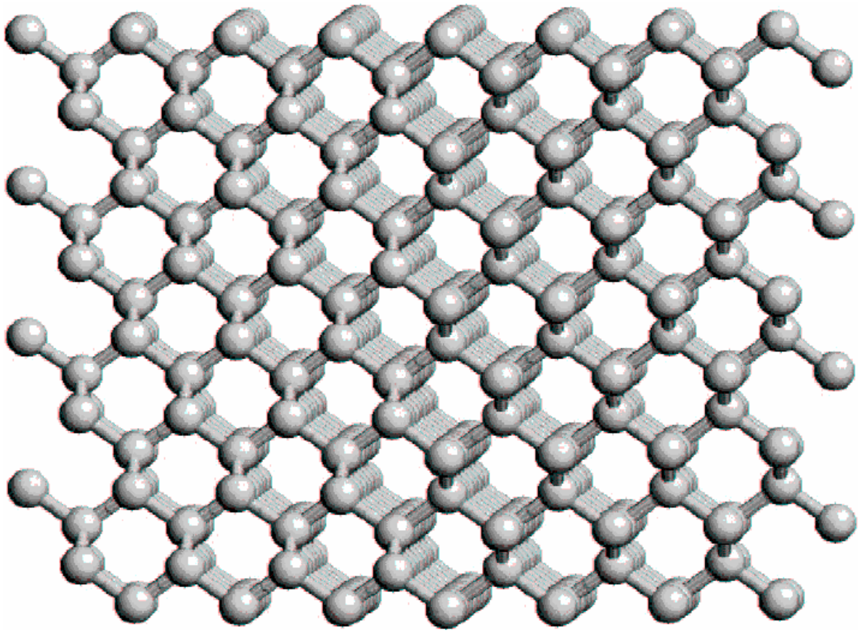

Figure 3.2: Silicon crystal viewed along <110> direction [3]. The <110> "channels" are visible.

3.2. Total Stopping Power

As mentioned above, interest in particle radiation in matter was sparked by the discovery of radioactivity at the very beginning of the 20th century – well before the structure of the atom was known. Niels Bohr is credited with the first stopping theory of ions in matter [6, 7] based on the nuclear theory of the atom in 1913. Bohr wrote the total SP as the sum of the electronic SP and the nuclear SP

$$S_{total} = S_{nuclear} + S_{electronic}, \tag{3.2}$$

where the nuclear SP, $S_{nuclear}$, is due to the interaction of the projectile ions with the nuclei of the target atoms and the electronic SP, $S_{electronic}$, is due to the interaction of the projectile ions with the electrons in the target materials. Bohr postulated (correctly) that $S_{electronic}$ dominates as the energy of the projectile gets large (see Fig. 3.3). In general, $S_{electronic}$ dominates when the projectile energy $\gtrsim 1\frac{keV}{AMU}$.

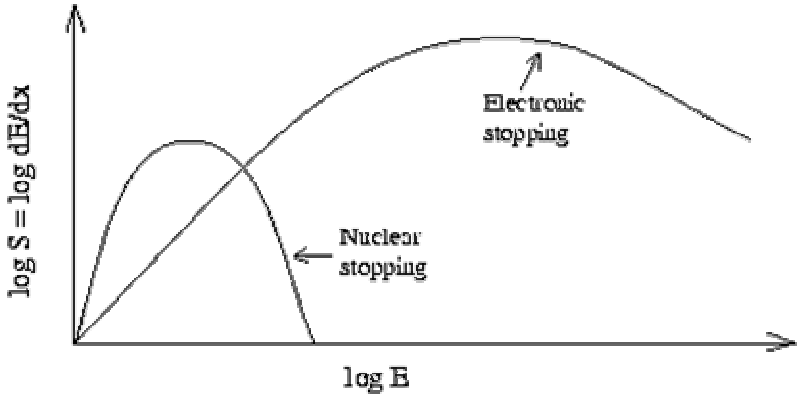

Figure 3.3: Relative electronic and nuclear SP's as a function of projectile energy for a typical projectile and target material. The peak of the nuclear SP is at about $1\frac{keV}{amu}$ and the peak of the electronic SP is at about $100\frac{keV}{amu}$ [8]

Bohr argued that the nuclear stopping dominates at low velocities and electronic stopping dominates at large velocities because of recoil kinematics of massive nuclei and light electrons. Note that the energy range in which we are interested (i.e. $\sim 25\frac{keV}{AMU}$) is large enough that electronic stopping dominates. Moreover, the channeling condition further reduces the effect of the nuclear SP so that nuclear SP is negligible.

3.3. Electronic Stopping Power – Review of Theory

3.3.1. Introduction

Bethe [9, 10] and Bloch [11, 12] reformulated Bohr's theory for $S_{electronic}$ using quantum mechanics. The Bethe-Bloch equations are still in use for high velocity light projectile ions, $10\frac{MeV}{amu} < E < 2\frac{GeV}{amu}$ [4]. Again, the systems that are of interest for our treatment consist of heavy low-velocity projectile ions where the Bethe-Bloch formalism is not applicable and thus does not agree with experimentally observed values for the SP. One of the Bethe-Bloch assumptions is that the projectiles are fully stripped. For projectile energies below about $10\frac{MeV}{amu}$, this assumption does not apply and therefore the Bethe-Bloch result diverges from experimentally observed SP's.

For low-velocity heavy projectile ions, the theory is somewhat more complicated. It is generally accepted that Fermi and Teller [13] derived the first theory for low-velocity particle radiation in matter. Most of the subsequent literature on low-velocity SP can be grouped into one of three approaches: Firsov's method, linear response, and the phase-shift formalism from static quantum mechanical scattering theory (see Fig. 3.4). A description of each approach is given in the following subsections.

Fermi and Teller published a theory for the electronic SP of a material for slow muons in 1947 [13]. Their goal was to derive an expression that could be used to predict whether a slow muon, $\upsilon << \upsilon_F$, emitted from a nuclear reaction would be captured before it decays. Fermi and Teller employed classical recoil kinematics to estimate the change in velocity of a fast target electron due to a collision with a slow, relatively heavy projectile

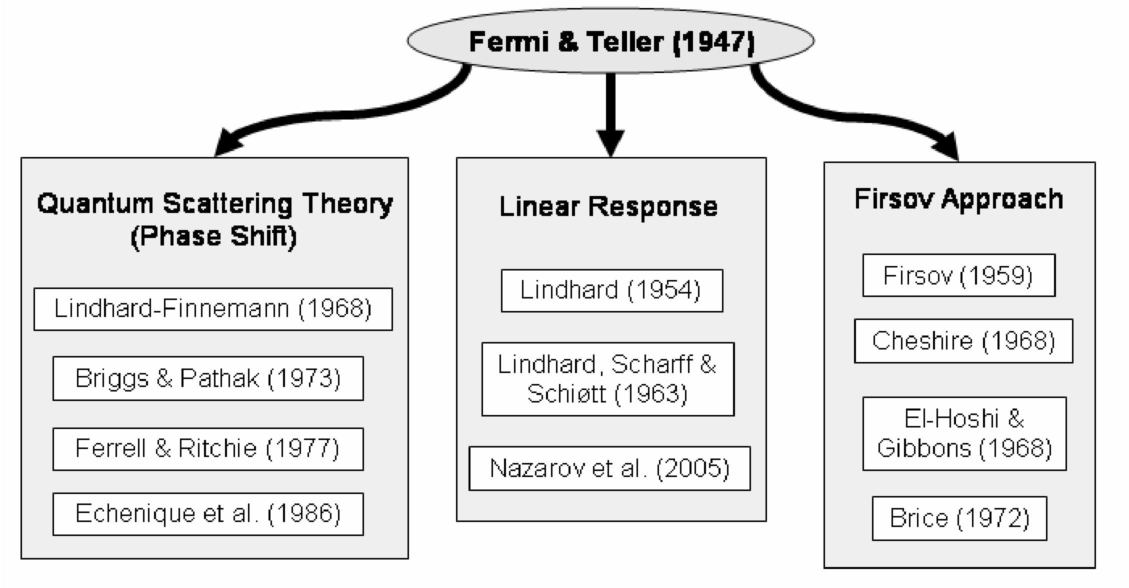

Figure 3.4: Low-velocity particle radiation SP theories all stem from the Fermi-Teller theory and can be grouped into one of three approaches. The above figure includes several of the most seminal papers on SP theory for each group.

to be on the order of υ (a head-on collision would result in the magnitude of the velocity of the electron changing by only 2υ). Assuming that the electrons in the target behave like a degenerate Fermi gas, then any collision that results in a velocity less than the Fermi velocity $\upsilon < \upsilon_F$ is disallowed due to the Pauli Exclusion Principle. Therefore only those electrons with velocities within about υ of υ_F will be allowed to participate in the slowing down of the projectile. The electronic SP is then

$$S_{electronic}^{FT} = \frac{2\upsilon}{3\pi} \ln\left(\frac{1}{\alpha r_s}\right), \tag{3.3}$$

where $\alpha \equiv \left(\frac{4}{9\pi}\right)^{1/3}$ and $r_s = \left(\frac{3}{4\pi n}\right)^{1/3}$ is the one-electron or Wigner-Seitz radius. The linear dependence of the SP on the velocity of the projectile in (3.3) is similar to Stokes law for the viscous force on a sphere in a liquid. This result is in agreement with experimentally observed data indicating that the SP is proportional to the velocity of the ion in the low velocity regime.

In the late 1960's, a series of experiments at low and intermediate velocities provided evidence that the SP has a complicated dependence on the atomic number of the projectile (Z_1). There were characteristic oscillations in the SP as a function of Z_1, which became known as Z_1 oscillations. This result was not predicted by any of the current theories and significant effort was put into modifying existing theories and developing new theories to account for these Z_1 oscillations.

3.3.2. Firsov's Approach

In this approach, one calculates the momentum transferred from the projectile electrons to the target electrons. Firsov [14] modeled the SP as a series of binary interactions (one projectile ion scattering off one target atom). In the Firsov model, a plane is defined halfway between the target and projectile (see Fig. 3.5).

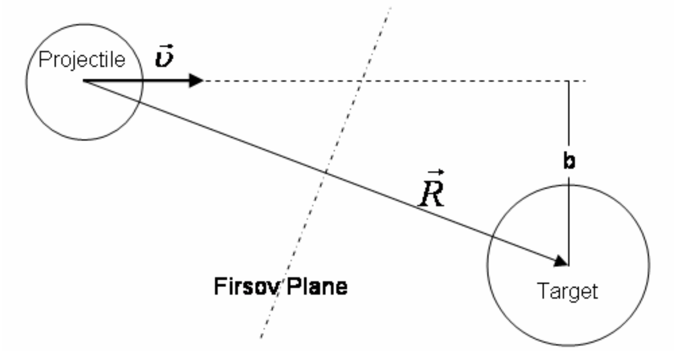

Figure 3.5: Geometry of the Firsov model.

Electrons on the projectile side of the plane are assumed to have the same average net velocity, v, of the projectile ion and electrons on the target side of the plane have zero net velocity. Any electron that crosses the plane will then experience a change in momentum equal to $\pm m_e\vec{v}$ depending on whether the electron moves from (to) the projectile side of the plane to (from) the target side of the plane. From conservation of momentum, there is a change of momentum in the opposite direction of either the target or projectile ion. Assuming a continuous distribution of electron density, then the flux across the Firsov plane from the target side to the projectile side can be defined as ϕ_t. The time rate of change of momentum (i.e. the force) on the projectile atom is

$$\mathbf{F}_p = -\phi_t m_e \vec{v}\,. \tag{3.4}$$

Conversely, the force on the target atom due to the flux from the target side to the projectile side is

$$\mathbf{F}_t = \phi_p m_e \vec{v}\,. \tag{3.5}$$

Firsov assumed that $\phi = \phi_t = \phi_p$. The infinitesimal work done on the projectile and target atoms is given by

$$\begin{aligned} dW_p &= -\phi m_e \vec{v} \cdot d\mathbf{R}_p \\ dW_t &= \phi m_e \vec{v} \cdot d\mathbf{R}_t\,. \end{aligned} \tag{3.6}$$

The total infinitesimal work done on the projectile and target ions is

$$dW = \phi m_e \vec{v} \cdot \left(d\mathbf{R}_t - d\mathbf{R}_p \right) = \phi m_e \vec{v} \cdot d\mathbf{R}\,, \tag{3.7}$$

where $d\mathbf{R}$ is the change in the relative position vector from the projectile to the target. The total work as a function of the impact parameter, b, can be calculated by integrating along the path of the projectile

$$W(b) = m_e \int_{z=b} \phi(\mathbf{R})\, \vec{v} \cdot d\mathbf{R}\,. \tag{3.8}$$

The work done by the change of momentum of the electrons given above in the Firsov model at some impact parameter, *b*, is assumed to be the inelastic energy loss of the collision. The stopping cross section, S_e, can be calculated from (3.8)

$$S_e = 2\pi \int_{b_0}^{\infty} db\, b\, W(b)\,, \tag{3.9}$$

where b_0 is the minimum impact parameter which is either set to zero or can be used as an adjustable parameter.

The key to this approach is then the method in which the electron flux, ϕ, across the Firsov plane is calculated. Originally, Firsov obtained the density, *n*, from the Thomas-Fermi model of the atoms. The infinitesimal flux, $d\phi$, across an infinitesimal area, dA, is

$$d\phi = \tfrac{1}{4} n \langle v \rangle dA\,, \tag{3.10}$$

where $\langle v \rangle$ is the average speed of the electrons. With this simple model, Firsov was able to reproduce the gross structure of the SP as a function of projectile velocity and the atomic number of the projectile and or target ions.

The Firsov model was modified by several groups [15, 16, 17, 18, 19] in order to reproduce the Z_1 oscillations These modifications fall into one of two categories: the semi-classical approximation first described by Cheshire et al [15] and Brice's [16] fully quantum mechanical partial wave function (PWF) approach. Brief descriptions of each of the two approaches are given below.

Cheshire [15] used Hartree-Fock orbitals to calculate the density and average velocity. The density is

$$n(\mathbf{r}) = \sum_m f_m\, \psi_m^* \,\psi_m \,, \tag{3.11}$$

where f_m are the occupation coefficients and ψ_m are the Hartree-Fock wavefunctions. The velocity is calculated from the expectation value of the kinetic energy operator, $\hat{T}$

$$\langle v \rangle = \sum_k f_k \sqrt{\frac{2}{m}\left\langle \psi_k \middle| \hat{T} \middle| \psi_k \right\rangle} \,. \tag{3.12}$$

Finally, Cheshire chose the position of the plane to be at that point where the contributions to the potential from both atoms are equal.

Brice [16] modified the Firsov method by calculating the electron flux from one-electron orbitals using the partial wavefunction (PWF) method. The PWF, ψ_+, corresponding to a one-electron wavefunction, ψ, is defined as the part of the wavefunction with a minimum momentum equal to k_0 across the Firsov plane. Orient the axes in Fig. 3.5 so that the $\hat{z}$ direction is parallel to $\vec{R}$. The PWF is then calculated from the reciprocal space representation of the one-electron orbital, $\tilde{\psi}(\mathbf{k})$

$$\psi_+(\mathbf{r}) = \left(\frac{1}{2\pi}\right)^{\frac{3}{2}} \int_{-\infty}^{\infty} dk_x \int_{-\infty}^{\infty} dk_y \int_{k_0}^{\infty} dk_z \,\tilde{\psi}(\mathbf{k})\, e^{i\mathbf{k}\cdot\mathbf{r}} \,. \tag{3.13}$$

The minimum momentum, k_0, is equal to the momentum of an electron traveling at the z-component of the velocity of the Firsov plane. It should be stressed that the PWF picks out only those electrons that have a momentum that can cross the Firsov plane in the frame of reference of the frame itself. The flux across the Firsov plane is then just the surface integral on the Firsov plane of the perpendicular component of the current density due to the PWF in the rest frame of the Firsov plane

$$\phi = \int_{\substack{Firsov \\ Plane}} \left[\mathrm{Re}\left(\psi_+^* \, i \frac{\partial}{\partial z} \psi_+ \right) - 2k_0 \, \psi_+^* \, \psi_+ \right] dA \, . \tag{3.14}$$

Brice applied the approach described above using hydrogenic wavefunctions to obtain a closed form expression (with some simplification [20]) for the stopping cross section

$$S_e = -128\left(N_t + N_p\right) \frac{\upsilon}{15 Z_{eff}} \, , \tag{3.15}$$

where Z_{eff} is either an adjustable parameter determined from experiment or from more first principles calculations.

The Firsov approach along with the subsequent modifications yielded results that were in fair agreement with the experimentally observed values. Nevertheless, none of the various flavors of this method were able to achieve parameter-free calculations that would agree with experiment better than a factor of 2 or so across a range of velocities (in the low-velocity regime) and across atomic species [20].

3.3.3. Linear Response

In 1954, Lindhard [21] described a method to calculate the SP of a material via the dielectric function of the target material. Lindhard treated particle radiation in a material as a perturbation to a classical electron gas. The dielectric function can be calculated from Poisson's equation

$$\varepsilon(\mathbf{k},\omega) \, k^2 \, \tilde{V}(\mathbf{k},\omega) = 4\pi \, \tilde{n}(\mathbf{k},\omega) \, , \tag{3.16}$$

where $\tilde{V}(\mathbf{k},\omega)$ is the reciprocal-space and frequency-domain electrical potential and $\tilde{n}(\mathbf{k},\omega)$ is the reciprocal-space frequency-domain electron density. The SP is calculated from the dielectric function

$$\frac{dE}{dx}=\frac{2Z_1^2}{\pi v^2}\int_0^{\infty}d\omega\,\omega\int_{\omega/v}^{\infty}dk\,\frac{1}{k}\mathrm{Im}\left[-\frac{1}{\varepsilon(\mathbf{k},\omega)}\right]. \tag{3.17}$$

Lindhard derived an expression for the dielectric function in the low-velocity limit (i.e. $v \ll v_F$) using the full Random Phase Approximation (RPA). By substituting this expression for the dielectric function into (3.17) one obtains the SP in the low velocity limit

$$\frac{dE}{dx}=\frac{2}{3\pi}Z_1^2 v\left[\ln\left(1+\frac{\pi}{\alpha r_s}\right)-\frac{1}{1+\frac{\alpha r_s}{\pi}}\right]. \tag{3.18}$$

Note α and r_s are defined after (3.3). This result was in better quantitative agreement with experiment than Fermi and Teller's model.

Whereas the Firsov approach depends greatly on how one calculates the electron flux across the Firsov plane, the Lindhard linear-response approach depends heavily on how the dielectric function is calculated. Recently, TDDFT linear-response calculations of the dielectric function have been used to calculate SP's with some success [22, 23].

3.3.4. Quantum Scattering Theory – Phase Shifts

Lindhard derived an alternative approach for calculating the SP of an ion in a material but he did not publish it. Instead, Finnemann was the first to report Lindhard's result in his 1968 Masters Thesis [24]. In this approach, the electronic SP is assumed to be due to the electrons in the material scattering off the potential of the ion. It is also assumed that the potential of the ion is spherically symmetric. The following derivation is reproduced from Refs. [25-27].

In the rest frame of the ion, the electrons in the material appear to have an average net momentum equal to

$$p = m_e \upsilon , \tag{3.19}$$

where it is assumed that the velocity of the ion in the rest frame of the material, υ, is small compared to speed of light so that the non-relativistic approximation to the momentum is valid. The corresponding wave number for the electron is

$$k = \frac{m_e \upsilon}{\hbar} . \tag{3.20}$$

Approximating the energy of the scattering solutions as that of a free electron

$$E = \frac{k^2}{2m_e} , \tag{3.21}$$

solutions to the Schrödinger equation with a spherically symmetric potential can be separated into radial and angular components that are eigenstates of the total angular momentum and the z-component of the angular momentum. The solutions take the following form

$$\psi_{lm}(\mathbf{r}) = R_l(r)\, Y_{lm}(\hat{\mathbf{r}}) , \tag{3.22}$$

where l and m are quantum numbers corresponding to the total angular momentum and z-component of the angular momentum, respectively. The angular functions in (3.22) are given by the spherical harmonics $Y_{lm}(\hat{\mathbf{r}})$. The radial functions, $R_l(r)$, are solutions of the radial Schrödinger equation. Defining $U(r) \equiv 2m_e V(r)$ and $u_l(r) \equiv rR_l(r)$, one may write the radial Schrödinger equation as

$$\left[\frac{d^2}{dr^2} - \frac{l(l+1)}{r^2} + k^2 - U(r)\right] u_l(r) = 0. \tag{3.23}$$

With the above equation, one can solve for the radial equation given the spherically symmetric potential.

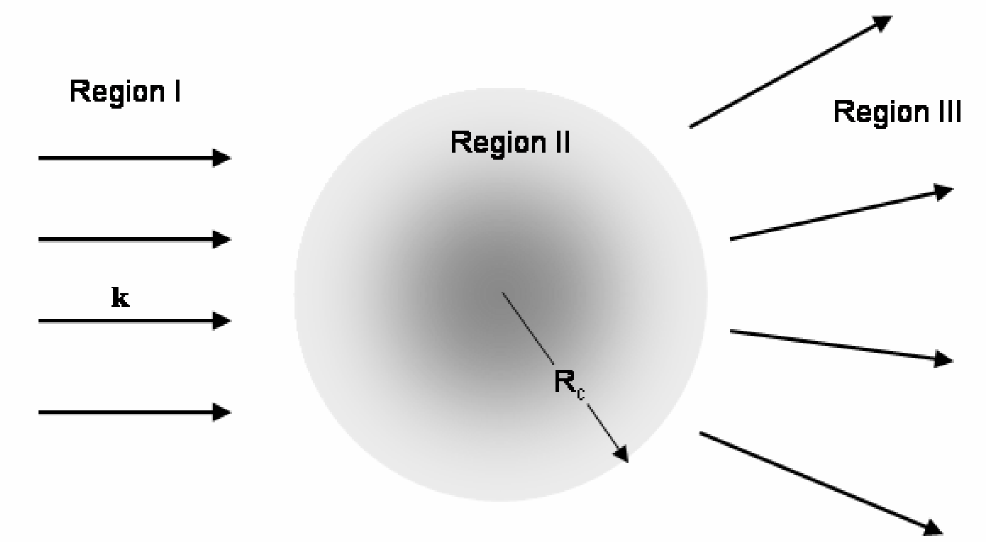

Figure 3.6: Schematic of a scattering event. Outside a sphere of radius R_c, the potential is zero. In Region I, the electron is just an incoming plane wave with momentum k. In Region II, the spherically symmetric potential is not zero and the radial Schrödinger equation must be solved for the eigenstates. In Region III, the potential is zero and the solution is a phase shifted spherically decomposed plane wave.

The next step is to analyze solutions of (3.23) more carefully. First, consider the case where the potential is zero. Solutions to (3.23) where $U(r) = 0$ must have the form of plane waves since this is the equivalent of a free electron. A plane wave decomposed in radial and angular components is just the product of spherical Bessel functions and spherical harmonics

$$e^{i\mathbf{k}\cdot\mathbf{r}} = 4\pi \sum_{lm} i^l j_l(kr)\, Y_{lm}(\hat{\mathbf{r}})\, Y_{lm}^*(\hat{\mathbf{k}}). \tag{3.24}$$

Note that **k** is pointing in an arbitrary direction. It is further assumed that the potential effectively vanishes beyond some cutoff radius. Consider the solution in three regions. Region I is far away from the scattering center when it the electron is just an incoming plane wave (i.e. the incoming wave). Region II is near the scattering center where the potential is not negligible. Region III is far away from the scattering center but after the electron has been scattered (i.e. the outgoing wave).

It is assumed that the incoming wavefunction is a plane wave. Therefore, the radial solutions to the Schrödinger equation in Region I are

$$R_l^I(r) = i^l j_l(kr). \tag{3.25}$$

In region II, one must solve the radial Schrödinger equation (3.23) restricted by the boundary conditions that the solutions and the first derivative of the solutions must match at the interface between region I and region II (i.e. $R_l^I(R_c) = R_l^{II}(R_c)$). In region III, again, the solution is similar to that given by (3.25) except that it is modified such that it is still a solution to the radial Schrödinger equation with zero potential but is able to match the boundary conditions at the interface between region II and region III (i.e. $R_l^{II}(R_c) = R_l^{III}(R_c)$),

$$R_l^{III}(r) = i^l c_l j_l(kr + \delta_l). \tag{3.26}$$

The radial solution in region I, $R_l^I(r)$, is similar to the radial solution in region III, $R_l^{III}(r)$, except for the coefficients, c_l, and the phase factors, δ_l (also referred to as scattering phase offsets). The coefficients, c_l, are chosen so that the boundary conditions are satisfied. The phase offsets, δ_l, can be physically interpreted as a measure of how the scattering potential affects the *l*-th component of the free particle (i.e. the part of the free particle with angular momentum *l*). Moreover, one may choose c_l so that δ_l are real.

It is often more convenient to solve for the radial wavefunction by recasting the radial Schrödinger equation in integral form. This approach allows one to include the boundary conditions [25],

$$R_l(r) = j_l(kr) - ik\int_0^\infty dr'\, r'^2 j_l(kr_<)\, h_l(kr_>)\, U(r')\, R_l(r'), \tag{3.27}$$

where h_l are spherical Hankel functions and $r_<$ and $r_>$ are defined such that

$$\begin{array}{ll} if \;\; r < r' & \begin{cases} r_< = r \\ r_> = r' \end{cases} \\ else \;\; r > r' & \begin{cases} r_< = r' \\ r_> = r \end{cases} \end{array}. \tag{3.28}$$

There are two methods that can be used to calculate the scattering phase offsets given a spherically symmetric potential. In the first method, the phase offsets are calculated from the radial wavefunctions and the potential using the relation

$$e^{i\delta_l}\sin(\delta_l) = -k\int_0^\infty dr\, r^2 j_l(kr)\, U(r)\, R_l(r). \tag{3.29}$$

Alternatively, Calogero [28] derived a method to calculate the phase offsets without the radial solutions. The result is a first-order nonlinear differential equation for the phase offsets as a function of the radius, $\delta_l(r)$,

$$\frac{d\delta_l(r)}{dr} + \frac{V(r)}{k}\left\{J_l(kr)\cos\left[\delta_l(r)\right] - N_l(kr)\sin\left[\delta_l(r)\right]\right\}^2 = 0, \tag{3.30}$$

where J_l are Riccati-Bessel functions of the first kind and N_l are Riccati-Neumann functions (i.e. Riccati-Bessel functions of the second kind). The above equation is subject to the boundary condition $\delta_l(0) = 0$. Once the potential vanishes, the radial derivative of the phase shifts must also vanish in order to satisfy (3.30) and therefore the phase shifts will not change for $r > R_c$, i.e., the phase shifts will approach their long range values as $r \to R_c$.

The phase shifts can be used to calculate useful quantities such as the scattering amplitude, the total scattering cross section, the transport cross section and the SP. Taking the initial direction of the incoming planewave to be along the z axis, the scattering amplitude, $f(\theta,\phi)$, can be written in terms of the phase shifts as

$$f(\theta,\phi) = \frac{1}{k}\sum_l (2l+1) e^{i\delta_l} \sin(\delta_l)\, P_l(\cos\theta), \tag{3.31}$$

where $P_l(x)$ are Legendre polynomials. Given the scattering amplitude, the total cross section can found by integrating the product of the scattering amplitude with its complex conjugate over all angles

$$\sigma_{tot} = \int d\Omega \left|f(\theta,\phi)\right|^2 = \frac{1}{k^2}\sum_{ll'} (2l+1)(2l'+1)\sin\delta_l \sin\delta_{l'} \int d\Omega\, P_l(\cos\theta)\, P_{l'}(\cos\theta). \tag{3.32}$$

The Legendre polynomials have the following orthogonality property,

$$\int_{-1}^{1} dx\, P_l(x)\, P_{l'}(x) = \frac{2\delta_{ll'}}{2l+1}. \tag{3.33}$$

The delta function in the above equation collapses one of the sums in (3.32) yielding the following expression for the total cross section

$$\sigma_{tot} = \frac{4\pi}{k^2}\sum_l (2l+1)\sin^2(\delta_l). \tag{3.34}$$

Massey and Burhop [29] derived an expression for the transport cross section as a function of the phase shifts and the electron wave number

$$\sigma_{tr} = \frac{4\pi}{k^2}\sum_l (l+1)\sin^2(\delta_l - \delta_{l+1}) . \qquad (3.35)$$

The transport cross section is also referred to as the momentum transfer cross section or the diffusion cross section. It is a measure of how much momentum is transferred to an object due to scattering. It is defined by the elastic differential scattering cross section

$$\sigma_{tr} \equiv 2\pi \int_0^{\pi} \frac{d\sigma}{d\Omega}_{el} (1-\cos\theta)\, d\theta \sin\theta \ . \qquad (3.36)$$

The factor of $(1-\cos\theta)$ accounts for the larger momentum transferred to the particle at larger scattering angles (i.e. the maximum momentum is transferred when the scattering angle is 180°). The transport cross section is related to the SP by

$$S = n\, m_e\, v^2\, \sigma_{tr} , \qquad (3.37)$$

where n is the density of the electrons in the material. Substituting (3.35) and (3.20) into (3.37) and assuming atomic units yields an expression for the SP in terms of the density and the phase shifts,

$$S = 4\pi n \sum_l (l+1) \sin^2(\delta_l - \delta_{l+1}) . \qquad (3.38)$$

Several groups have used the above approach to calculate the SP for ion radiation in materials. Briggs and Pathak [30] were the first to publish SP's using this technique in 1973. They calculated the phase shifts by using a Molière form for the potential of an atom, derived from the Thomas-Fermi model of the atom

$$V(r) = \frac{1}{r}\sum_{j=1}^{3} a_j e^{-b_j r} \ . \qquad (3.39)$$

Where a_j and b_j are fit parameters to the potential using the Thomas-Fermi model for the ion.

In 1977, Ferrell and Ritchie [31] calculated the phase shifts by approximating the potential as a Yukawa screened Coulomb potential

$$V(r)=\frac{Z_1}{r}e^{-\kappa r}\,. \tag{3.40}$$

The screening length, κ; and the phase shifts are determined self-consistently by satisfying (3.30), (3.40) and the Friedel sum rule (see [32] for an excellent derivation)

$$Z_1=\frac{2}{\pi}\sum_l(2l+1)\delta_l\,. \tag{3.41}$$

Echenique et al. [33] calculated the SP by modifying the quantum scattering approach described above in the following way. First, the potential of the projectile in a homogeneous electron gas (HEG) is calculated using DFT. In the second part of this method, the phase shifts are calculated from the solutions of the SE for electrons scattering off this potential. They used the Friedel sum rule to check that they had included enough terms in the expansion. The theory has a free parameter, namely the constant electron density of the homogeneous electron gas. The parameter was fitted by requiring the calculated stopping power for boron to match the experimental value. Agreement with experimental results is good for well-channeled ions along the <110> direction in silicon, except for high-Z values. Agreement with experimental values for the <111> channel, random orientations and channeling in aluminum is not as good.

Kumar and Pathak [34] approximated the inhomogeneity of the electrons in the target material using the shell model [35,36] for the axial charge. In the shell model, the electron density in the channel is cylindrically symmetric about the axis of the channel. They approximated the electron density as

$$n(r) = ae^{br^2} + c, \tag{3.42}$$

where r is the distance to the axis of the channel running down the center of the channel, a = 0.000154, b = 0.727563, and c = 0.012289. The momentum transfer cross section, σ_{tr}, is calculated from the phase shifts of the static scattering states off of a parameterized Moliere potential for each projectile species as described above. The SP is then calculated from (3.38). The density is found by averaging the expression for the density given by (3.42) over the an area of radius R_s

$$n_{avg} = \frac{1}{\pi R_s^2} \int_0^{R_s} dr \, 2\pi \, n(r), \tag{3.43}$$

where R_s is the radius that is equal to the position of the maximum density of the outermost orbital of the projectile in its most likely charge state. For example, a sodium ion is assumed to be singly ionized so R_s would be the distance to the maximum density of the 2p orbitals. Again, n_{avg} is plugged into (3.38) to obtain the SP's.

The Shell model of Kumar and Pathak produced good qualitative agreement with experiment. These authors were the first to incorporate a method to account for the inhomogeneity of the target electron gas into the Quantum Scattering Theory approach. However, they were unable to achieve good quantitative agreement because of the lack of accurate and self-consistent potentials in the calculations of the phase shifts.

Finally, the last significant improvement to this approach was made by Calera-Rubio, Gras-Marti and Arista in 1994 [37]. They suggested a method to improve the theory so that it would give better general agreement with experiment (e.g. <111>

channel in silicon and aluminum targets). They approximated the scattering potential with the Yukawa potential (following Ferrell and Ritchie [31]). Using the FSR, they calculated a set of self-consistent phase shifts for a mesh of possible target electron densities, $\delta_l(r_s)$. From the scattering phase shifts, the SP can be calculated from (3.38). Finally, they treated the target electron gas as the sum of spherically symmetric density distributions, $n(r)$. The total SP is found by integrating over the volume of each atomic cell

$$S_e^{avg} = 4\pi N_a \int_0^{r_a} dr\, r^2\, S(r), \tag{3.44}$$

where N_a is the number of atoms per unit volume, r_a is the atomic radius, and $S_e(r)$ is the SP as a function of the density at radius r. With this basic approach, they were able to account in a rough way for the inhomogeneity of the target electron gas although they had to introduce an additional parameter, r_a, for each ion.

Further improvements were made to this approach using the Extended Friedel Sum Rule (EFSR) to account for the velocity of the projectile when enforcing the self-consistent screening of the projectile [38]. However, there was no significant improvement in the agreement of the theory with experiment.

3.3.5. Calculations of Stopping Power using TDDFT+MD

All of the approached for SP calculations described above entail ad hoc assumptions about the form of potentials or electron densities and/or free parameters that are fit to the data. We now describe the present application of TDDFT+MD, the method described in Chapters I and II, to the calculation of the SP. The method has no free parameter that need to be fitted to the data. In this formulation, the electrons propagate by integrating the time-dependent Kohn-Sham equation using the adiabatic local-density approximation for exchange-correlation while the nuclei are treated as classical point charges that evolve by integrating the classical equations of motion. In general, when applying this approach, there can be a problem due to quantum effects that are neglected by the semi-classical treatment of the nuclei [39,40]. However, it is known that this so-called branching problem is negligible when this method is applied to systems with energetic ions [41] because the quantum fluctuations of the forces on the ions being too small to appreciably alter the relatively large momenta of the ions. For example, TDDFT+MD has been successfully applied to the study of the collision of alkali-metal clusters [42,43].

3.4. Binary Atomic Collisions

Before we describe the results of SP calculations, we apply TDDFT+MD to study the collision of two atoms in order to assess the methods capabilities and limitations in a simpler case. The simulation cell at the beginning of the calculation is shown in Fig. 3.7. Initially, a DFT ground-state calculation takes place for two isolated silicon atoms separated by 8Å. At the beginning of the time-dependent part of the calculation, one atom is held fixed and the other is given an initial velocity, $\upsilon = 2\frac{\text{Å}}{\text{fs}}$ directed so that it scatters off the first atom with an impact parameter, $b = 2\text{Å}$.

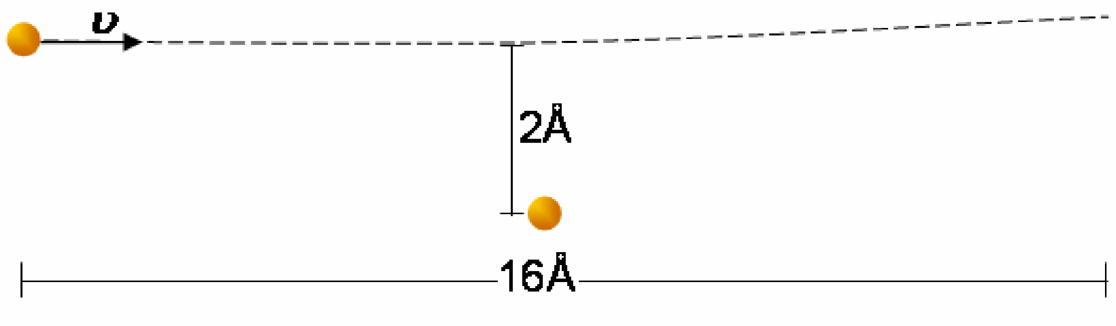

Figure 3.7: Initial state of a binary atomic scattering TDDFT+MD calculation.

As the calculation proceeds, the projectile ion moves across the simulation cell and scatters off the stationary ion, which is free to move. As mentioned in Chapter I, the total energy of the TDDFT+MD system is conserved

$$E_{tot} = E_{nuc} + E_{instant} = constant \, . \tag{3.45}$$

The instantaneous energy and the kinetic energy of the nuclei for this system are shown as a function of the position of the projectile in Fig. 3.8 (a) and 3.8 (b), respectively.

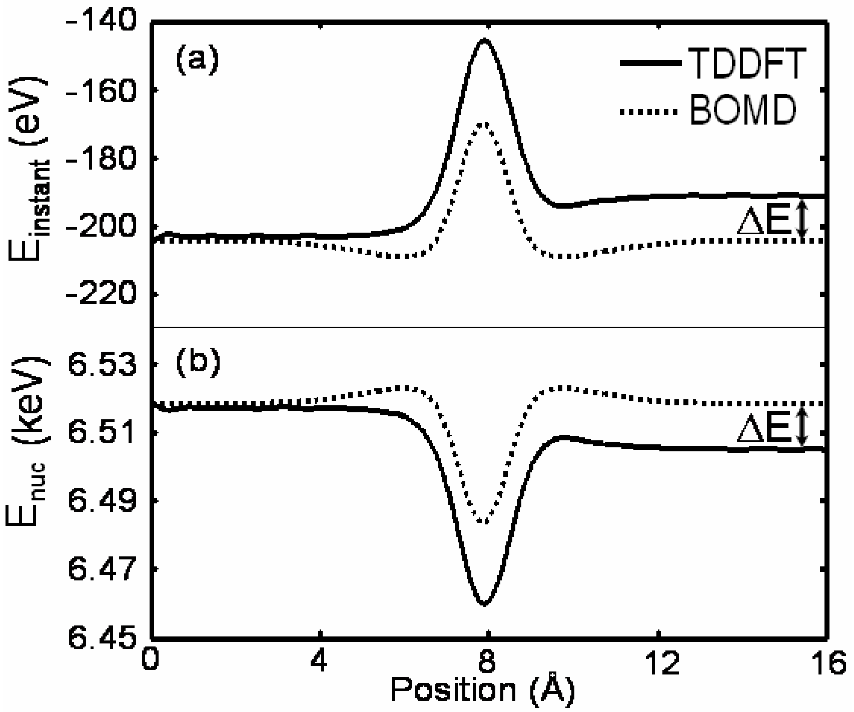

Figure 3.8: (a) Instanteous and (b) kinetic energy for TDDFT (solid line) and BOMD (dotted line) calculations of silicon-silicon scattering described in Fig. 3.7.

From Fig. 3.8, for a TDDFT+MD calculation, the total energy is conserved with energy being transferred back and forth between the electrons (instantaneous energy) and kinetic energy of the projectile. As the projectile passes the target atom, the instantaneous energy increases to a maximum and then declines to some asymptotic value equal to the initial value plus ΔE. Conversely, the nuclear kinetic energy decreases to a minimum at the point of nearest approach and the then increases asymptotically to a value that is equal to the initial kinetic energy less ΔE. The overall effect of the collision is to transfer ΔE to the excitation of the electrons from the kinetic energy of the projectile. From the density plots in Figs. 3.9, it can be seen that a transitory bond forms between the atoms when they are near one another. For this collision, the impact parameter is 1Å, which results in a repulsive force when the atoms are near the distance of closest approach. Thus the kinetic energy of the projectile dips to a minimum and the instantaneous energy is at a maximum when the projectile is at the distance of closest approach.

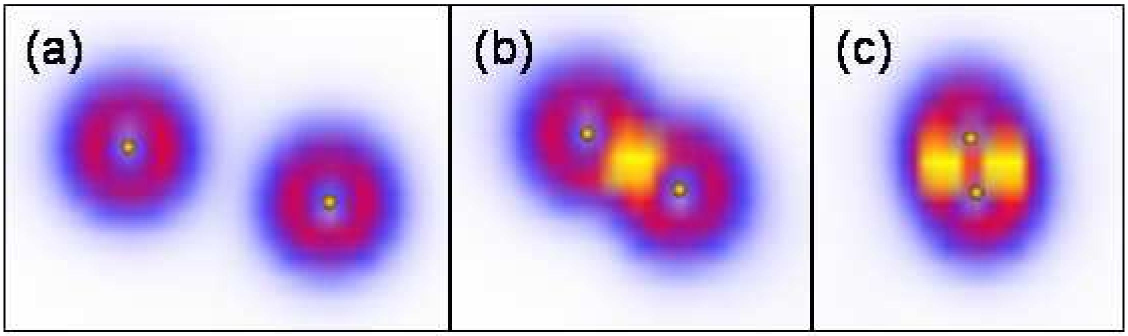

Figure 3.9: The electron density before (a), and during (b),(c) the collision between two silicon atoms. A transitory bond forms between the atoms when they are near enough. The impact parameter is 1Å.

The results for a Born-Oppenheimer Molecular Dynamics (BOMD) calculation of the same event (see Chapter I for a description of BOMD) are also shown in Fig. 3.8. However, since the instantaneous energy in a BOMD calculation is just the instantaneous ground-state energy of the system, both the instantaneous and nuclear kinetic energies return to their respective initial values after the collision (i.e. the ground-state energy is just a function of the inter-atomic distance).

It is clear from this simple example that the use TDDFT+MD is a powerful tool to study systems that entail *energy transfer from nuclei to electrons*. For such systems, the BOMD approach is not suitable because of the fundamental underlying assumption does not permit the electrons to ever be excited. A good example of such a system is the movement of projectile ions through channels in silicon crystal, which will be described in the next section.

3.5. Stopping Power of channeled ions

3.5.1. Introduction

We have considered the case of channeled ions moving at intermediate velocities through silicon. There are several reasons why channeling conditions are ideal for the TDDFT+MD approach. First, a channeled ion is guaranteed not to violate the restrictions of a pseudo-potential based calculation (i.e. one ion cannot be within the projector radius of another) as it moves through the channel. Second, the SP exhibits a characteristic oscillatory dependence on the atomic number of the projectile (Z_1) in the intermediate-velocity regime that is exaggerated when the ions are channeled compared to non-channeled ions. These Z_1 oscillations had not been predicted by the stopping theory that was current at the time they were originally observed. Indeed, Z_1 oscillations remain a challenging result to reproduce theoretically, relying on the detailed quantum mechanical behavior of a projectile interacting with a target system. Thus, reproducing Z_1 oscillations provides a useful benchmark for the ability of a method to capture the physics of ion radiation in materials. Finally, ions in the intermediate-velocity regime are well-suited for TDDFT+MD calculations because the projectile is able to move through a typical sized simulation cell (on the order of 10's of Angstroms) in a few femto-seconds – well within the limits of available computational power.

3.5.2. Experimental Observations

Z_1 oscillations were first observed experimentally in a variety of target materials where the beams were oriented in random directions with respect to the orientation of the target crystal [44, 45, 46]. The amplitudes of these Z_1 oscillations for a given material were observed to increase when the ions were channeled [47, 48, 49]. We focus on the experimental observations by Eisen in 1968 [48] of the SP for ions moving through the <110> and <111> channels of thin films of silicon. The results of Eisen are shown in Fig. 3.10. In this experimental setup, the target material is a thin film of silicon a few microns thick oriented so that the projectiles move through either the <111> or <110> channels. The end on view of the <111> and <110> channels are shown as insets in Fig. 3.10 illustrating how much larger the <110> channels are compared to the <111> channels. The projectile ions are initially accelerated to a constant velocity equal to $1.5\text{x}10^8$ cm/s or 12 keV/nucleon. Since it is the initial velocity that is held constant for the various projectile species, the initial kinetic energy varies with the mass of the projectile.

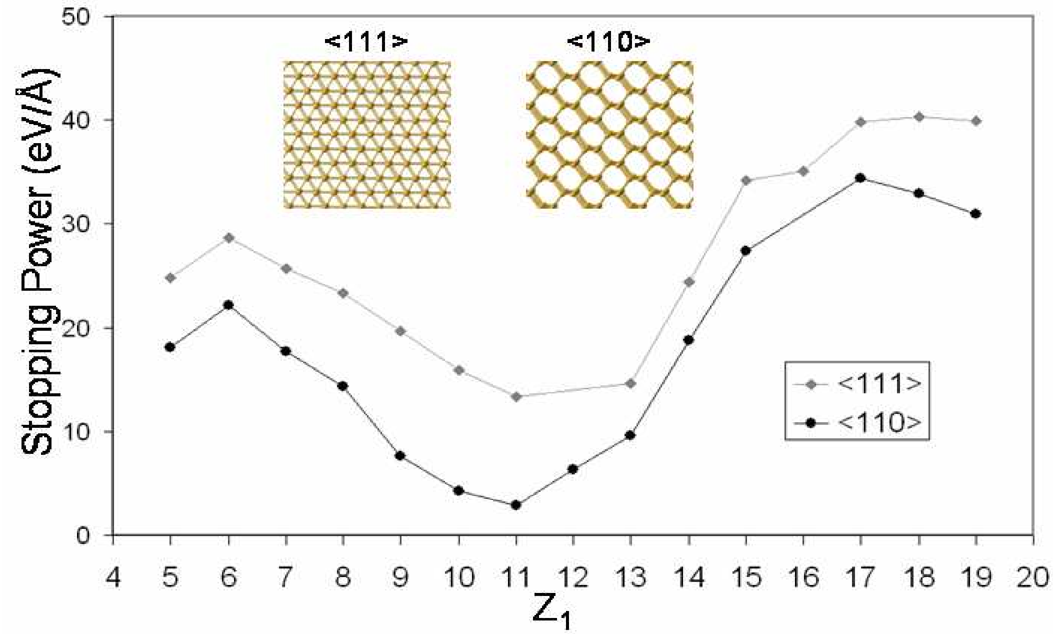

Figure 3.10: The experimentally observed SP's as a function of the atomic number of the projectile (Z_1) for ions moving through the <111> and <110> channels of silicon [48]. The end-on view of the channels is shown in the inset to illustrate the difference in size. The effect of this difference in channel size is that the SP is greater along the <111> direction compared to the <110> direction although the qualitative structure of the two curves is very similar.

The Z_1 oscillations are not not very intuitive. One might expect that the SP would steadily decline as Z_1 increases since the atom itself is getting bigger. However, the SP is observed to decline across most of the second period from carbon to neon then it increases across most of the third period from sodium to argon. Moreover, the group of the projectile does not seem to have much impact on the Z_1 structure. For example, while carbon and silicon are both group IV projectiles – each with four valence electrons – carbon is a local maximum in the curve and silicon is far away from both a local maximum and local minimum. As another example, consider neon and argon, two noble gases with similar electronic properties, have SP's that differ almost by an order of magnitude (for the <110> case). Moreover, neon is near the local minimum whereas argon is near a local maximum.

3.5.3. TDDFT+MD Calculation Details

The electronic ground-state of a simulation cell similar to that shown in Fig. 3.11 is taken to be the initial state of the system. For the case of a <110> run, the target material consists of 72 silicon atoms in an un-relaxed bulk structure oriented so that the projectile atom will move through a <110> channel. The periodic boundary conditions imply that the target is an infinite thin film. After the groundstate is found, the time-dependent part of the calculation begins where the projectile ion is given an initial velocity, $\upsilon = 1.5\times10^{8} cm\ s^{-1}$, equal to that reported by Eisen [48]. As described above, the electrons evolve by integrating the TDKS equation while the nuclei propagate by integrating the classical equations of motion.

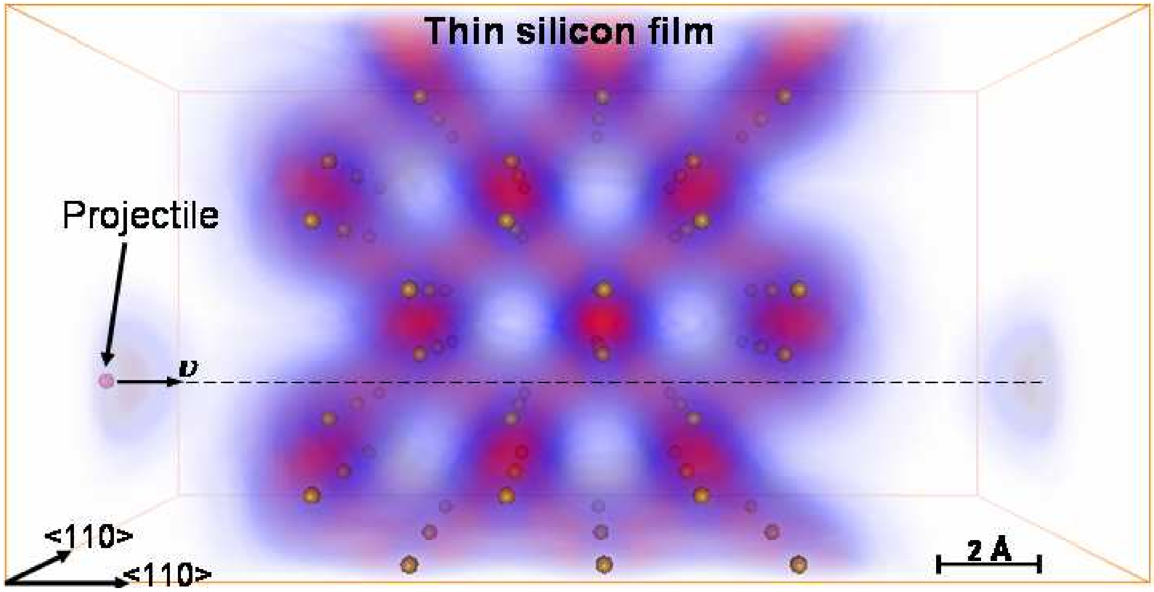

Figure 3.11: Initial state of the simulation cell for the SP calculation for projectiles moving through a <110> channel in silicon. The target consists of 72 silicon atoms in unrelaxed bulk crystal structure (periodic boundary conditions are applied in the directions perpendicular to the projectile motion).

3.5.4. Method for Calculating the SP

The SP can be determined directly by averaging the force on the projectile while in the crystal. For example, the force on a Mg projectile is shown as a function of position in the simulation cell in Fig. 3.12. The average force in the crystal is shown as a gray dashed line. The grid lines indicate when the projectile is in one of the planes of atoms as it moves through the channel.

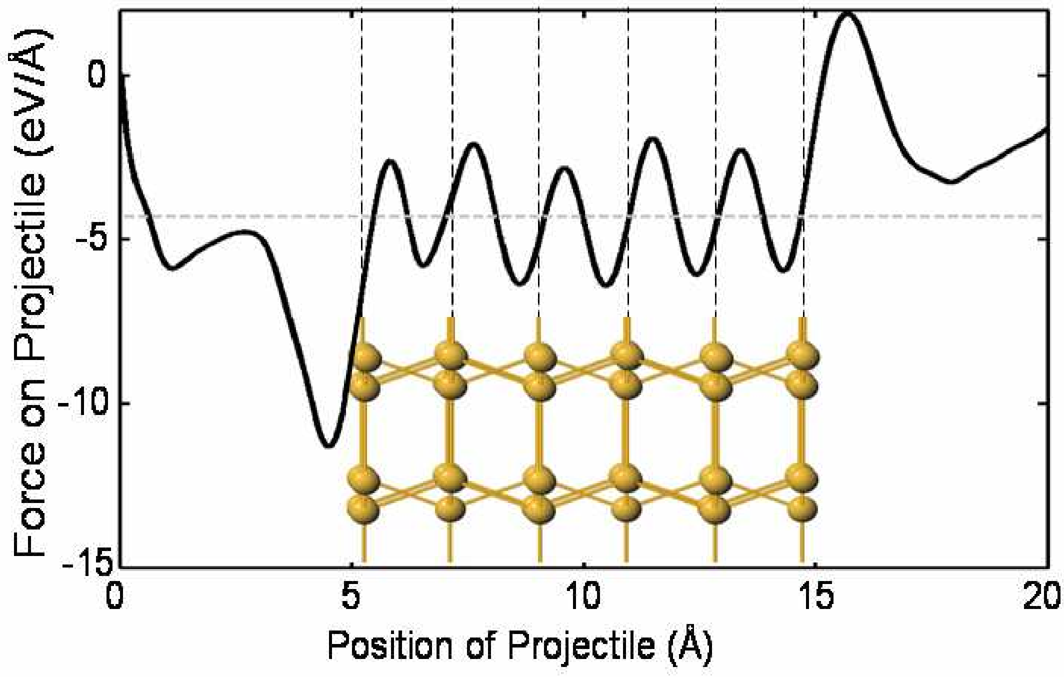

Figure 3.12: The force on a Mg projectile as it moves through the simulation cell. The horizontal dashed gray line indicates the average value of the force, -4.89 eV/Å, while *in* the crystal. The positions of the planes of atoms in the crystal are shown by the vertical dashed lines.

Alternatively, the SP can be calculated from the kinetic energy of the projectile using Eq. (3.1). For example, the kinetic energy of a Mg projectile is shown in Fig. 3.13. The best linear fit to the kinetic energy is given by the dashed line. The slope of this line is the SP. The six vertical dotted lines in Fig. 3.13 correspond to when the projectile is in one of the [110] planes of atoms (i.e. it is at its point of closest approach to neighboring atoms). The inset is the difference between the kinetic energy and the linear fit to the kinetic energy while the projectile is in the crystal. Note that the scale of the inset is eV versus keV for the bigger plot. The variation in the kinetic energy as it moves from one plane of atoms to the next in the crystal indicates the formation and dissolution of transitory bonds with the nearest neighbors. This approach is equivalent to that described above for averaging the forces directly since the velocity of the ions in the TDDFT+MD

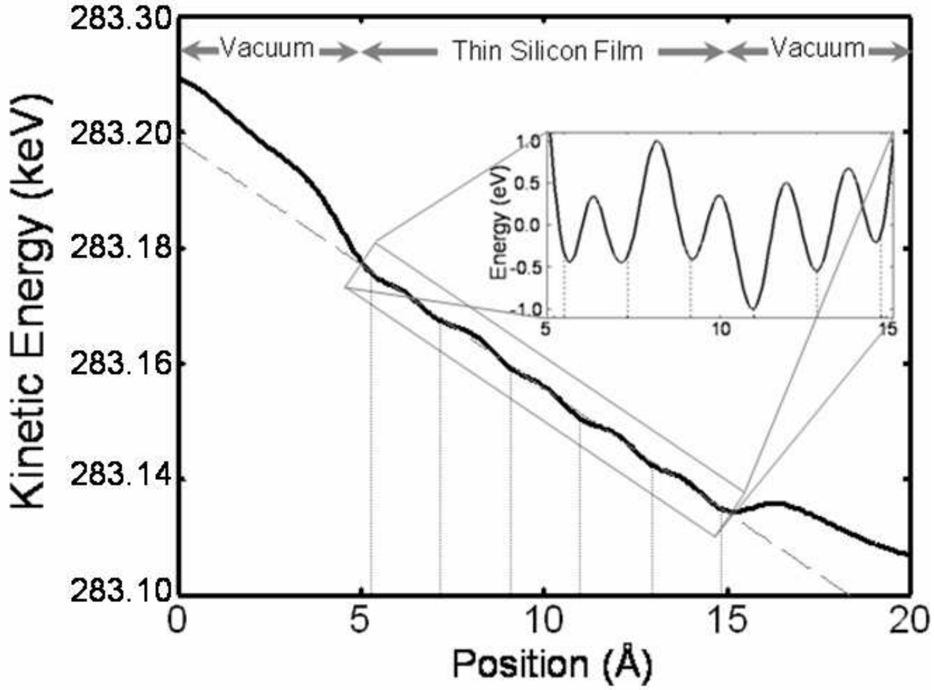

Figure 3.13: The kinetic energy of a Mg ion channeling through a thin film of silicon. The dashed line is a fit to the portion of the kinetic energy of the ion while in the thin film. The SP is found from the slope of the fit. The inset is the difference between the kinetic energy and the fit.

formulation are calculated by integrating the forces. In practice, the time step sizes are sufficiently small that the SP calculated from both methods are equal.

Although the two approaches described above are equivalent, the second approach suggests a third alternative method for calculating the SP. From (3.45), the time rate of change for the instantaneous energy must be equal and opposite the time rate of change of the nuclear kinetic energy

$$\frac{dE_{instant}}{dt} = -\frac{dE_{nuc}}{dt}. \tag{3.46}$$

Dividing both sides by the velocity and applying the chain rule yields an expression for the SP directly

$$S = -\frac{dE_{nuc}}{dx} = \frac{dE_{instant}}{dx}. \tag{3.47}$$

From this expression, one can calculate the SP from the change in the instantaneous energy. The instantaneous energy, nuclear kinetic energy and total energy are shown in Fig. 3.14 for a magnesium projectile moving through silicon crystal.

Note that the total energy is not perfectly conserved. This is an artifact due to numerical instability and can be controlled by reducing the time step size. As is usual in electronic-structure calculations, one focuses on the convergence of the quantity of interest, namely the SP in the present case. Once the SP is converged, smaller time steps improve overall energy conservation but have no appreciable effect on the SP value.

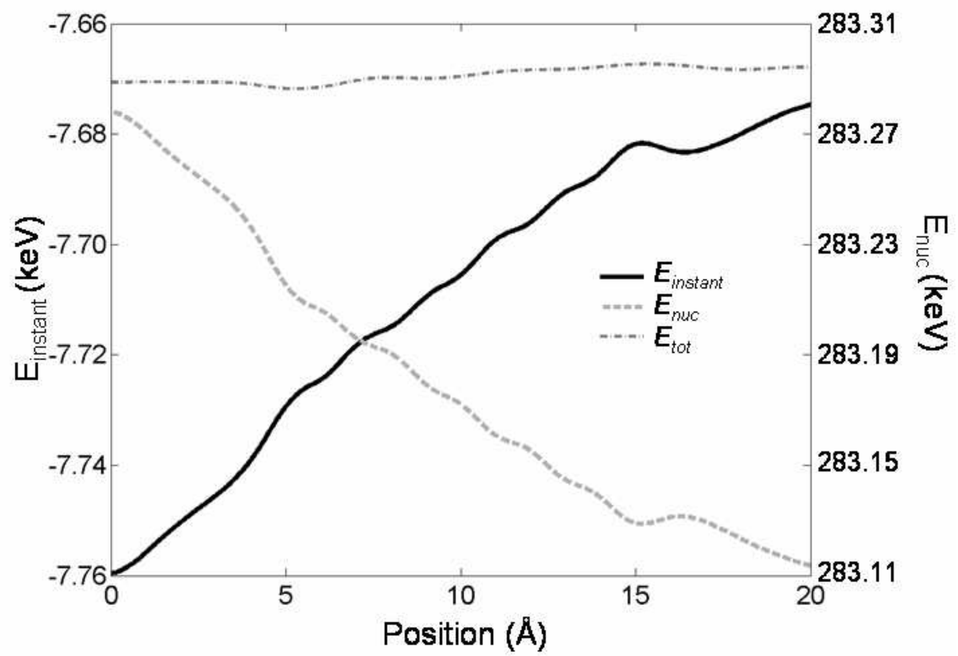

Figure 3.14: The instantaneous, nuclear kinetic and total energies as a function of the position of a Mg projectile moving through a silicon thin film. Note that the total energy is not perfectly conserved. Energy conservation is improved with smaller time steps.

To analyze the relation between time step size and the error in SP as calculated from the instantaneous energy versus the nuclear kinetic energy, both $E_{instant}$ and E_{nuc} are shown as a function of the dt^{-1} in Fig. 3.15.

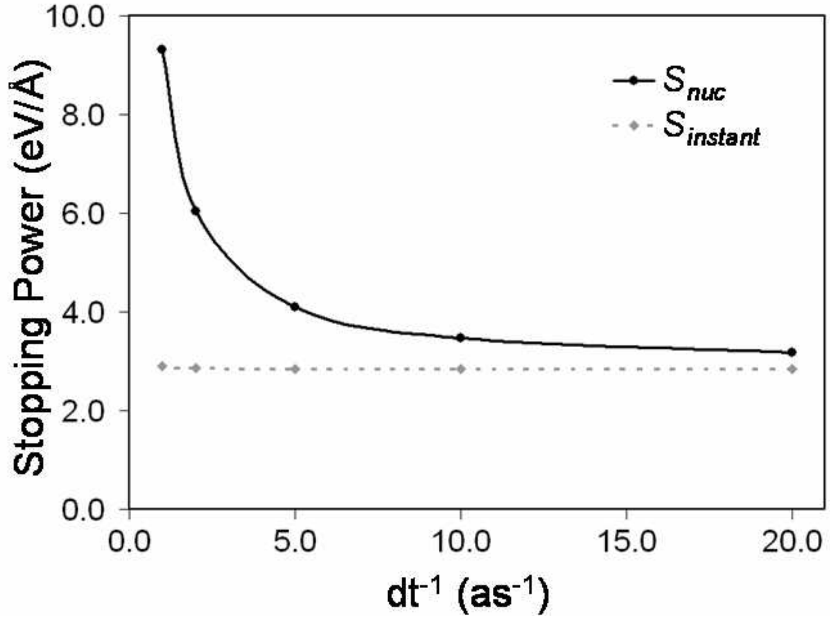

Figure 3.15: SP's for a Na projectile calculated from the instantaneous energy, S_{nuc}, and the nuclear kinetic energy, $S_{instant}$, as a function of the inverse of the time step size (dt^{-1}). Note that the units are inverse atto-seconds, where $1as = 10^{-18}s$

From Fig. 3.15, the convergence of the SP calculated from the nuclear kinetic energy, S_{nuc}, is much more sensitive to the size of the time step than the $S_{instant}$, the SP calculated from the instantaneous energy. Thus, one can use larger time steps (i.e. better computational efficiency) by calculating the SP from the instantaneous energy instead of the nuclear kinetic energy. It should be noted that the error in the nuclear kinetic energy does not affect the rest of the calculation because the only effect that the nuclear kinetic energy has on the rest of the calculation is that the velocity of the ion determines where it will be at each time step. Since the forces (i.e. the SP's) are too small to appreciably alter the velocity, the error in nuclear kinetic energy does not have any significant effect on the rest of the calculation. For example, of the projectile species in this study, carbon feels the most deceleration due to its relatively low mass and large SP. The velocity of the carbon projectile exiting the crystal is equal to 99.95% of the initial velocity. Even a relatively large error in the force will have little impact on the actual position of the projectile in the cell at any given time. Therefore, in practice, we report the $S_{instant}$ as the SP. If $S_{instant}$ varies from S_{nuc} by a significant amount, we run simulations with smaller time steps in order to verify that it has converged.

3.5.5. Stopping Power Error Analysis

The source of inaccuracy in the S_{nuc} calculations is due to the calculation of the forces. The expression for the forces on the ions was derived from the Lagrangian for the TDDFT+MD formulation as described in Chapter I (note that an equivalent expression can be derived for *time-dependent* quantum mechanical systems from the Hellmann-Feynman theorem [50]). The expression for the force on the I^{th} nucleus is

$$\mathbf{F}_I = -\nabla_I \sum_j \left\langle \psi_j \middle| \hat{H}_e \middle| \psi_j \right\rangle . \tag{3.48}$$

Note that the gradient is taken with respect to the I^{th} set of nuclear coordinates. Since the wavefunctions do not depend explicitly on the nuclear positions, the gradient can be applied directly to the Hamiltonian. Since the nuclear kinetic energy operator commutes with the *electronic* positions, (3.48) may be written as

$$\mathbf{F}_I = \mathbf{F}_I^{nn} - \int d\mathbf{r}\, n(\mathbf{r})\, \nabla_I v_{ne}^I\left(\left|\mathbf{r} - \mathbf{R}_I\right|\right), \tag{3.49}$$

where $\mathbf{F}_I^{nn}$ is the contribution to the force on the I^{th} nucleus due to Coulomb repulsion from the other nuclei. For free-space boundary conditions the nuclear-nuclear Coulomb force on any given nucleus is the sum over the Coulomb forces due to the other nuclei in the simulation cell. For periodic boundary conditions, the sum must be over an infinite number of nuclei in the periodic images (this can be implemented efficiently via an Ewald Summation [51]). The second term in (3.49) includes $\upsilon_{ne}^I(|\mathbf{r}-\mathbf{R}_I|)$, which is the nuclear-electron contribution to the Hamiltonian. It is often approximated with pseudopotentials [52] for the sake of numerical efficiency. In practice, this expression is evaluated in reciprocal space where the gradient is a diagonal operator. Following the same derivation as given in Chapter II, the force is

$$\mathbf{F}_I = \mathbf{F}_I^{nn} - \Omega \int d\mathbf{G}\, \tilde{n}(\mathbf{G})\, i\mathbf{G}\, \tilde{\upsilon}_{ne}^I(\mathbf{G})\, e^{i\mathbf{G}\cdot\mathbf{R}_I}, \tag{3.50}$$

where $\tilde{n}(\mathbf{G})$ and $\tilde{\upsilon}_{ne}^I(\mathbf{G})$ are the reciprocal space representations of the density and the potential of the I^{th} nuclei, respectively. It is likely that the factor of **G** in eq. (3.50) contributes to the error in S_{nuc} because a factor of **G** results in the higher momentum (i.e. **G**) components of the electron density contributing more to the forces. For a converged ground-state calculation, the electron density vanishes for large **G** values so their contribution to the forces is negligible even with the factor **G**. However, for time-dependent runs in the TDDFT+MD formalism, electrons can be excited and therefore there could non-vanishing values of the density at large **G**. Since any error in the propagation of the wavefunctions is exaggerated by the factor **G**, the calculation of the forces is more sensitive to time-step size. The instantaneous energy does not have this factor of **G**. Although we have not rigorously proved this mechanism as the cause of the error, there are two findings that support this hypothesis. First, we have observed that for a fixed time-step size the error in the SP increases as the wavefunction and density cutoffs increase, which would suggest that additional high-**G** components are disproportionately responsible for the error. Second, Sugino and Miyamoto [53] found that they could maintain numerical stability at larger time steps by imposing a cutoff on the high momentum components of *both* the kinetic energy operator and electron density. Note, however, that such a cutoff prescription introduces an unacceptable error into the calculation even though the total energy appears conserved.

3.5.6. Initial Charge State

Obtaining the correct charge state of the projectile while inside the crystal presented difficulty for previous theories until Ferrell and Richie [31] suggested applying the Friedel Sum Rule to ensure that the effective scattering potential was self-consistent. For the approach of Echenique et al. [33], DFT was used to calculate the self-consistent potential of the projectile in the HEG and therefore the self-consistency was ensured by the method (although they verified self-consistency via the Friedel Sum Rule). For TDDFT+MD calculations, the charge state of the projectile is determined by the quantum mechanical time-evolution operator and therefore it is not necessary to check the charge state with the Friedel Sum Rule.

However, it is possible that the initial charge state of the projectile while *outside* the crystal (see Fig. 3.11) may affect SP. In order to check for the effect of the initial charge state, an external bias was applied to the initial ground-state calculation in order to force a desired charge on the projectile. The bias was removed at the start of the time dependent portion of the calculation. We found that the initial charge state has almost *no* affect on the SP. This result is consistent with the experimental observations of Jiang et al. [54].

3.5.7. Theoretical Results

The SP calculation described above was performed for projectile species ranging from boron (Z_1=5) to potassium (Z_1=19). The results for the TDDFT+MD calculation, experimental observation [48] and the quantum-scattering-theory results of Echenique et al [33] are shown in Fig. 3.16 for projectiles moving through <110> channels in silicon crystal.

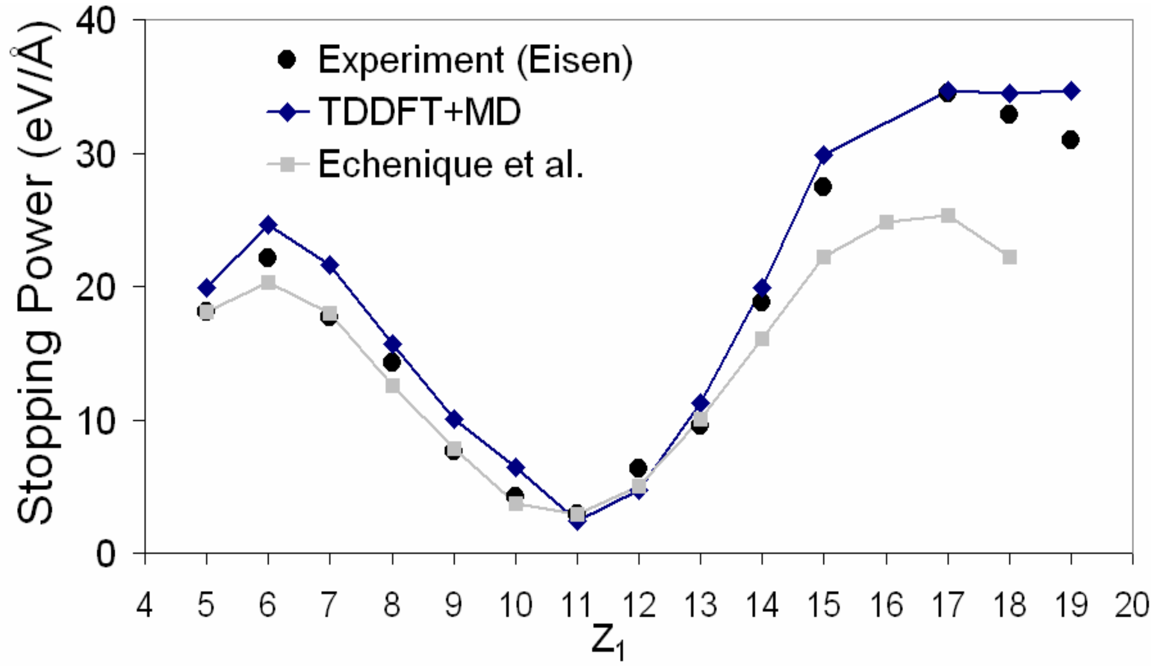

Figure 3.16: The <110> channeling SP as a function of projectile species (Z_1) for TDDFT+MD, experiment by Eisen [48], and the quantum scattering theory by Echenique et al. [33]

The TDDFT+MD results are generally in excellent quantitative agreement with experiment for the entire range of projectile species. Moreover, the TDDFT+MD calculations do not require any parameters to be fit to experiment. The results of Echenique et al. are in excellent agreement with experiment for the smaller species of projectiles ($Z_1 < 14$) but systematically underestimate the SP for the larger species starting with silicon ($Z_1 \geq 14$). It is also necessary to include at least one parameter for this method. In this case, Echenique et al. adjusted the density of the HEG so that the SP they calculated for boron ($Z_1=5$) was equal to the experimentally observed value.

It has been suggested that the limited agreement between the theory by Echenique et al [33] and the data is due to the approximation of the electron gas in the solid as a homogeneous electron gas of constant density. We will now present calculations that demonstrate that both the inhomogeneities in the electron density in silicon and dynamical effects (changes in the electron density associated with the projectile and corresponding feedback on the crystal electrons) are essential in obtaining quantitative SP values without free parameters.

Consider Fig. 3.17 which shows 2-D views of the electronic density centered on the projectile as the latter moves through the channel from one atomic plane (a) to a position equidistant from the two nearest atomic planes (b) to the next atomic plane (c). The inset in the bottom right of the figure shows the positions of these slices as seen from the side. The 1-D plots in (d) correspond to the density along the color-coded lines in the 2-D plots. The solid and dotted light gray horizontal lines correspond to densities of $r_s=2.23$ and $r_s=2.38$, respectively. Later we will compare with HEG SP theories that assume densities corresponding to $r_s=2.23$ and $r_s=2.38$. Note that *the density varies by* *about an order of magnitude from the center of the channel to the nearest bond center.* As the projectile gets bigger it "sees" a higher average density and therefore the HEG density that is fitted to measured SP values for small-Z projectiles is not as good for larger-Z projectiles, as indeed is the case with the results by Echenique et al [33].

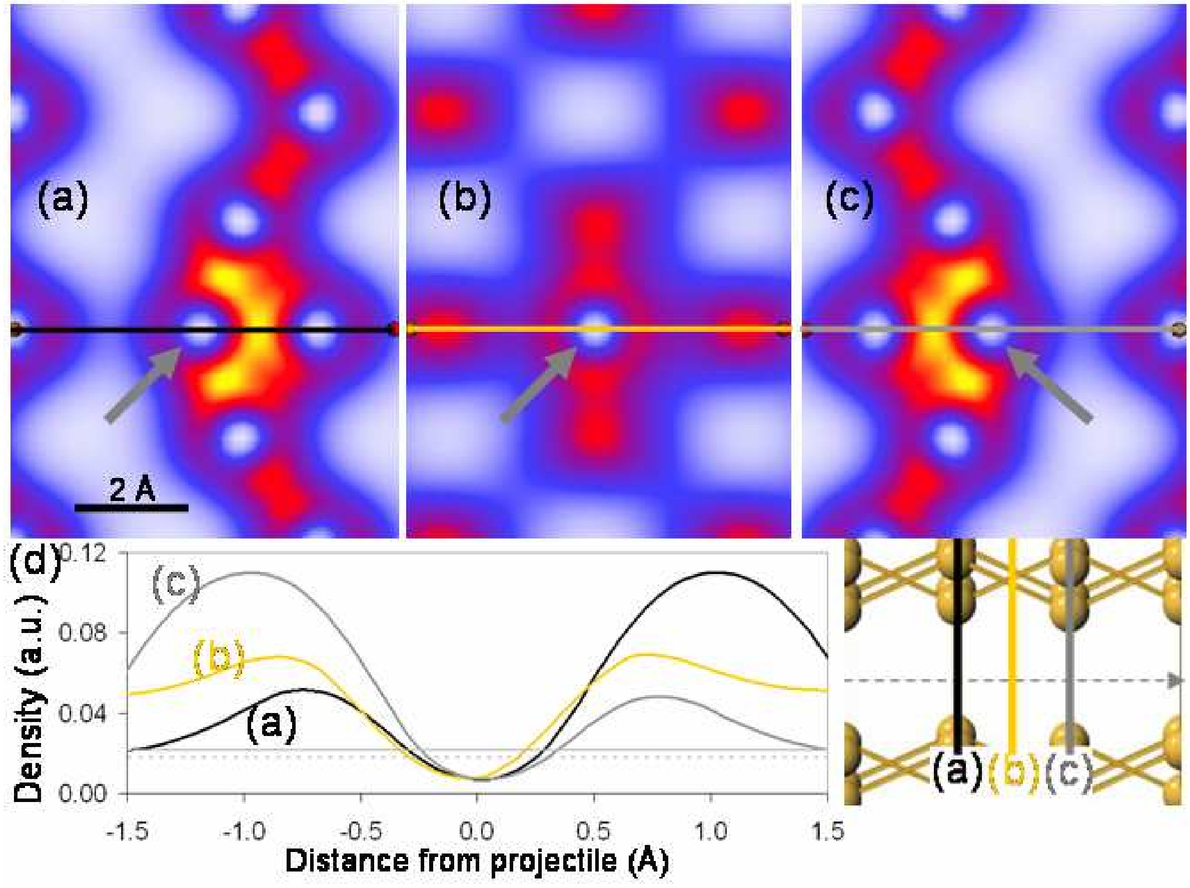

Figure 3.17: Plots of the valence electron density in the [110] plane centered on the projectile as it moves from one plane of atoms (a), to a distance equidistant from planes of atoms (b), to the next plane of atoms (c) through a <110> channel. The middle plot corresponds to when the projectile is half way between the planes of atoms. The density is calculated from the pseudo-wavefunctions and is therefore negligible in the ion core. The gray arrows point to the projectile. The 1-D plots of the density through the projectile are also shown in (d). The solid horizontal gray line corresponds to a constant density r_s=2.23 and the dotted horizontal gray line corresponds to a constant density, r_s=2.38.

In contrast to prior methods, the TDDFT+MD approach includes the full electronic structure of the target lattice. In order to test the role of these inhomogeneities in the electron density in determining SP values, we performed TDDFT+MD SP calculations for projectiles moving through a HEG. Such a calculation includes the full dynamical response of the electrons (both in the target and associated with the projectile) but does not account for the inhomogeneity in the target electron density. In a first set of calculations, we used the electron density used by Echenique et al [33] in order to examine the effect of dynamical response. The results are shown as open red diamonds in Fig. 3.18 (a), It is clear that the differences from the results of Echenique et al. are substantial, demonstrating that dynamical response is not negligible. Furthermore, what should be an improvement in the calculation (inclusion of dynamical response that is neglected by Echenique et al.) worsens the agreement with the data. In a second set of calculations, we adjusted the density of the HEG until the calculated SP agreed with the experiment value for boron (Z_1=5) and then used that density for the rest of the projectiles. This density corresponds to a Seitz radius, r_s=2.23. The results of these calculations are shown in Fig. 3.18 (a) as open blue diamonds. Once more, agreement with the data is not very good. In fact the two sets of results show that changing the constant electron density of the HEG seems to shift the overall curve rigidly, demonstrated that there is no value of a constant electron density that can reproduce the experimental SP values if full dynamical response is included. The net conclusion is that both electron-density inhomogeneities and dynamical response are needed to obtain quantitative agreement with the data without free parameters.

In order to further corroborate the above conclusion we performed SP calculations for ions moving through the <111> channel of a Si lattice [48]. The experimental data, the present results using TDDFT+MD, and the results from the quantum-scattering-

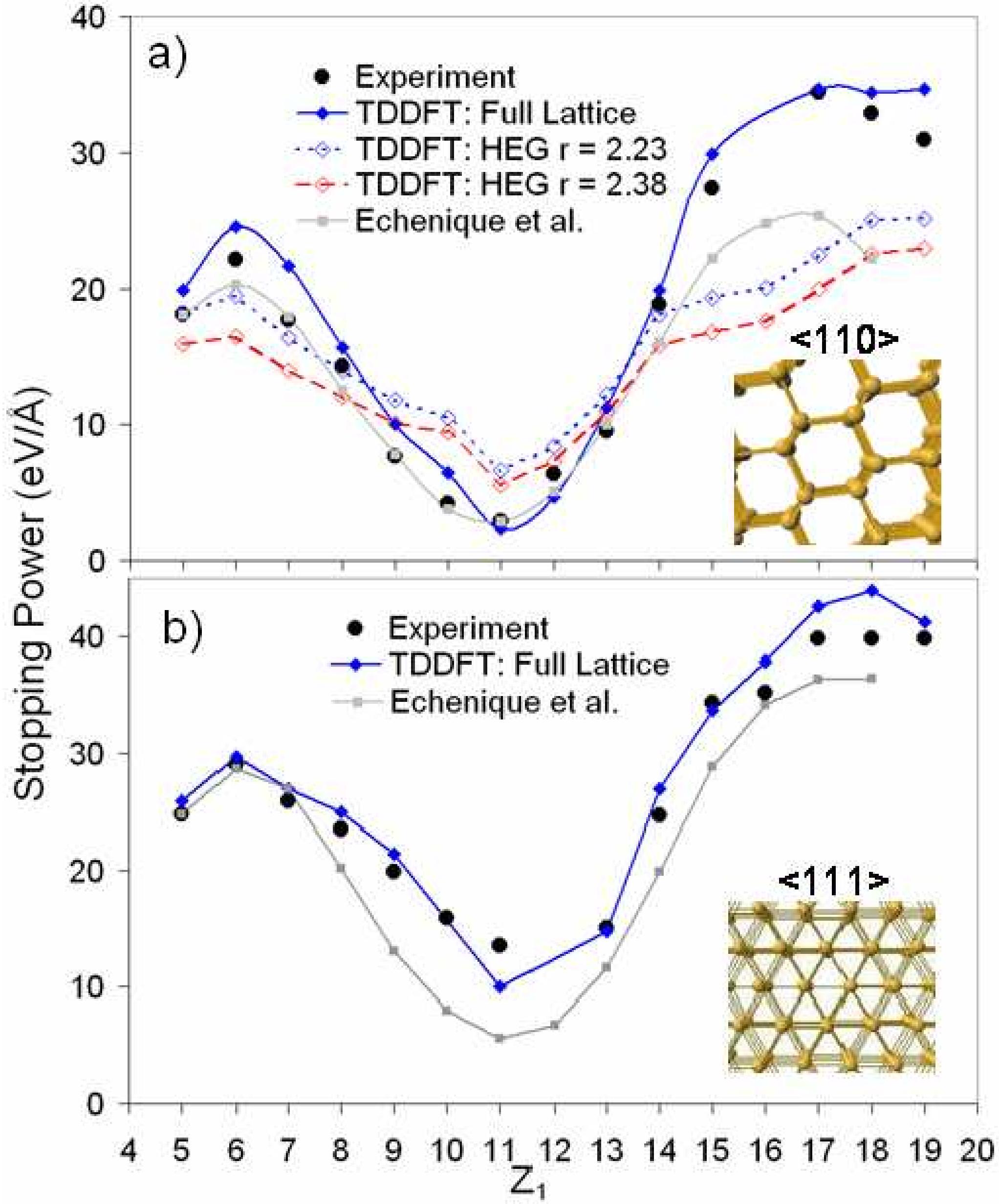

Figure 3.18: (a) Comparison of measured and calculated <110> SP's. (b) <111> measured and calculated SP's. The insets show the relative sizes of the <110> and <111> channels.

theory of Echenique et al. are shown in Fig. 3.18 (b). The insets show the relative sizes of the <110> and <111> channels.

As for the <110> case, the TDDFT+MD calculated SP's for <111> channeling are in good quantitative agreement with the experimental data across the whole range of projectile species while the quantum scattering theory results of Echenique et al [33] systematically underestimate the SP for the larger projectile species. The difference between the <111> and <110> results is that this systematic underestimation of the SP begins at oxygen (Z_1=8) for <111>. Since the <111> channel has a smaller cross section, the range of species for which the HEG approximation works is smaller than for the <110> channel. Because the projectiles in a <111> channel are more constricted, they feel non-uniformity of the target electron density more acutely than projectiles in a <110> channel.

3.5.8. Conclusions

We have demonstrated that the TDDFT+MD approach can be used to obtain *quantitative* agreement with experiment for the SP's of low-velocity projectiles moving through a non-uniform electron density such as those found in real materials *without* any parameters. We chose to study channeling projectiles in a silicon crystal because (a) the amplitude of the Z_1 oscillations are larger for channeling conditions (b) there are experimentally observed values against one can measure the accuracy of the theory and (c) channeling projectiles are guaranteed to have some minimum impact parameter with respect to nearest target atoms that is greater than the projector radius of the underlying pseudo-potential representation that is used in our implementation of TDDFT. We found that the SP can be calculated from the instantaneous energy more accurately for a given time step size than by calculating SP directly from the force on the projectile. We also found that the initial charge state of the projectile *before* it enters the crystal has almost no measurable affect on the final calculated SP. Therefore the charge state of the projectile once inside the crystal is only dependent on its atomic number (Z_1), velocity, and the target material – not on the initial state before entering the crystal. This is consistent with experimental observation. Finally, the TDDFT+MD approach allows one to avoid the HEG approximation that is implicit to the quantum scattering theory that is currently most often cited for low-velocity SP calculations.

3.6. References

[1] M. Pierre Curie, *Comptes Rendus*, **130** 76 (1900).

[2] P. Sigmund, *Stopping of Heavy Ions A Theoretical Approach*, Springer Tracts in Modern Physics Volume 204. Springer, Berlin, Germany (2004)

[3] J. Peltola, *Stopping Power for Ions and Clusters in Crystalline Solids*, University of Helsinki Report Series in Physics, Helsinki, Finland, 2003.

[4] J.F. Zeigler, *J Appl Phys / Rev Appl Phys*, **85** 1249 (1999).

[5] In order to be consistent with the literature, Z_1 is the atomic number of the projectile and Z_2 is the atomic number of the target material.

[6] N. Bohr, *Philos Mag*, **25** 10 (1913).

[7] N. Bohr, *Philos Mag*, **30** 581 (1915).

[8] K. Nordlund, PhD Dissertation, University of Helsinki, Finnish Academy of Technology, Helsinki, Finland (1995).

[9] H. Bethe, *Ann Physik*, **5** 325 (1930).

[10] H. Bethe, *Z Phys*, **76** 293 (1932).

[11] F. Bloch, *Ann Physik*, **16** 285 (1933).

[12] F. Bloch, *Z Phys*, **81** 363 (1933).

[13] E. Fermi and E. Teller, *Phys Rev* **72** 399 (1947).

[14] O.B. Firsov, *Zh. Eksp. Teor. Fiz.* **36** 1517 (1959) [*Sov. Phys. – JETP*, **9** 1076 (1959)].

[15] I.M. Cheshire, G. Dearnaley, and J.M Poate, *Phys Lett*, **27** 304 (1968).

[16] D.K. Brice, *Phys Rev A*, **6** 1791 (1972).

[17] C.P. Bhalla and J.N. Bradford, *Phys Lett A*, **27** 318 (1968).

[18] K.B. Winterbon, *Can J Phys*, **46** 2429 (1968).

[19] A.H. El-Hoshy and J.F. Gibbons, *Phys Rev*, **173** 454 (1968).

[20] S.A. Cruz, C. Vargas-Aburto, D.K. Brice, E.V. Alonso and D.G. Armour, *Phys Rev A*, **27** 2403 (1983).

[21] J. Lindhard, *Mat Fys Medd Dan Vid Selsk*, **28 no. 8** p1 (1954).

[22] V.U. Nazarov, J.M. Pitarke, C.S. Kim, and Y. Takada, J. Phys Cond Matt, **16** 8621 (2004).

[23] V.U. Nazarov, J.M. Pitarke, C.S. Kim, and Y. Takada, *Phys Rev B*, **71** 121106(R) (2005).

[24] J. Finnemann. En redegørelse for resultaterne af beregninger over spredning af elektroner med lav energi på afskærmede Coulombfelter, Masters Thesis, Aarhus University (1968).

[25] E.S. Abers. *Quantum Mechanics*, 265ff. Pearson Education Inc, New Jersey (2004)

[26] R. Shankar. *Principles of Quantum Mechanics*, 523ff. Plenum Press, New York (1994).

[27] L.I. Schiff, *Quantum Mechanics*, 100ff, McGraw-Hill Book Company, New York (1968).

[28] F. Calogero, *Variable Phase Approach to Potential Scattering*, Academic Press, New York (1967).

[29] H.S.W. Massey and E.H.S. Burhop, *Electronic and Ionic Impact Phenomenon vol I*, Clarendon Press, Oxford (1969).

[30] J.S. Briggs and A.P. Pathak. *J Phys Can: Solid State Phys*. **6** L153. (1973).

[31] T.L. Ferrell and R.H. Ritchie, *Phys Rev B*, **16** 115 (1977).

[32] C. Kittel, *Quantum Theory of Solids*, Wiley, New York (1963).

[33] P.M. Echenique, R.M. Nieminen, J.C. Ashley and R.H. Ritchie, *Phys Rev A*. **33** 897 (1986).

[34] V.H. Kumar and A.P. Pathak. *J. Phys. Condens. Matter* **5**, 3163 (1993).

[35] A.P. Pathak, *Phys. Status Solidi*, b **86** 751 (1978).

[36] R. Agnihotri and A.P. Pathak *Nucl. Instrum. Methods*. B **67** 39 (1992).

[37] J. Calera-Rubio, A. Gras-Marti, N.R. Arista. *Nucl. Instrum. Methods.* B **93** 137 (1994).

[38] A.F. Lifschitz, N.R. Arista. *Phys Rev A.* **58**, 2168 (1998).

[39] J.B. Delos and W.R. Thorson. *Phys Rev A*. **6** 720 (1972).

[40] O.V. Prezhdo and P.J. Rossky. *J. Chem Phys*. **107** 825 (1997).

[41] J.C. Tully and R.K. Preston. *J Chem Phys*. **55** 217 (1991).

[42] U. Saalmann and R. Schmidt. *Z Phys D*. **38** 153 (1996).

[43] U. Saalmann and R. Schmidt. *Phys Rev Lett.* **80** 3213 (1998).

[44] Y.A. Teplova, V.S. Nikolaev, I.S. Dmitriev and L.N. Fateeva. *Sov. Phys. JETP*. **15** 31 (1962).

[45] B. Fastrup, P. Hvelplund and C.A. Sautter, *K. danske Vidensk. Selsk., Math-fys. Meddr*. **35** 10 (1966).

[46] J.H. Ormrod, J.R. MacDonald and H.E. Duckworth. *Can. J. Phys.* **43** 275 (1965).

[47] L. Eriksson, J.A. Davies and P. Jespersgaard. *Phys Rev.* **161** 219 (1967).

[48] F.H. Eisen. *Can. J. Phys.* **46** 561 (1968).

[49] J. Bøttiger and F. Bason, *Radiat. Effects*. **2** 105 (1970).

[50] M. DiVentra and S.T. Pantelides. *Phys. Rev. B.* **61**, 16207 (2000).

[51] P. Ewald. *Ann. Phys.* **64**, 253 (1921).

[52] L. Kleinman and D.M. Bylander, *Phys Rev Lett.* **48** 1425 (1982).

[53] O. Sugino and Y. Miyamoto, *Phys Rev B*, **59** 2579 (1999).

[54] W. Jiang, R. Grötzschel, W. Pilz, B. Schmidt, and W. Möller, *Phys Rev B*, **59**, 226 (1999).

CHAPTER IV

INTERACTIONS OF ELECTROMAGNETIC RADIATION WITH MATTER

4.1. Introduction

In this chapter, we employ TDDFT to examine the interaction of electromagnetic radiation with matter. In the TDDFT formulation, electromagnetic radiation is *not* quantized. Instead, electromagnetic radiation is represented by classical fields, which is a fundamental limitation of the formalism. The goal is to find systems of interest where this particular approximation does not inhibit the ability of TDDFT to capture the underlying physics.

We will explore two distinct cases. First we will investigate the absorption of electromagnetic radiation. In the second case we examine emission. We represent the external perturbing electromagnetic field as a classical 4-vector potential which couples to the electronic system via the canonical momentum and scalar potential. The canonical momentum is defined as

$$\hat{\mathbf{p}}_{can} \equiv -i\nabla + q\mathbf{A} \, . \tag{4.1}$$

A is the 3-vector portion of the 4-vector potential representation of the external electromagnetic field. Note that TDDFT is only formally defined for longitudinal vector potentials [1]. Therefore we must use the long wavelength approximation (see below) to couple light to the system. In practice we choose to work in the Coulomb gauge where the gauge constraint is given by

$$\nabla \cdot \mathbf{A} = 0 \, . \tag{4.2}$$

The Coulomb gauge is numerically desirable for two reasons. First, it guarantees that the vector potential only represents the transverse component of the electromagnetic field (i.e. light). External electromagnetic radiation (e.g. laser light) is assumed to have sufficiently long wavelength so that at any given instant in time the electric field is constant everywhere in space (long wavelength approximation)

$$\mathbf{E}(\mathbf{r},t)=\mathbf{E}_0(t). \tag{4.3}$$

The reason why the Coulomb gauge is advantageous now becomes apparent for periodic systems. For any gauge where the external electric field is represented by a scalar potential, a constant electric field in a supercell is represented by a saw-tooth potential, which would result in a discontinuity at the boundaries. In contrast, in the Coulomb gauge, the electric field is the time derivative of the vector potential and the saw-tooth problem is avoided entirely

$$\mathbf{E}(t)=-\frac{\partial \mathbf{A}(t)}{\partial t}. \tag{4.4}$$

The second reason why the Coulomb gauge is convenient to implement is that the scalar potential is determined by solving Poisson's equation for the instantaneous charge density

$$\nabla^2 V=-4\pi\rho . \tag{4.5}$$

When adding TDDFT to an existing DFT code base, the existing machinery to calculate the scalar potential can be used to construct the TDDFT Hamiltonian.

In the above case, we have a time-dependent electron density. We already know that a time-dependent classical charge density emits classical radiation. Specifically, one may solve Maxwell's equations for the 4-vector potential describing the electromagnetic radiation emitted from a time-varying charge density. Often it is sufficient to apply the dipole approximation in conjunction with the power spectrum method to obtain the spectrum of the emitted radiation (i.e. we approximate the radiation emitted from this classical charge distribution as if it were an oscillating dipole) [2],

$$P(\omega) = \frac{\omega^4}{3}\left|\tilde{\mathbf{D}}(\omega)\right|^2 . \tag{4.6}$$

$P(\omega)$ is the power spectrum and $\tilde{\mathbf{D}}(\omega)$ is the frequency domain representation of the dipole moment. The real space, real time definition of the dipole moment is

$$\mathbf{D}(t) \equiv \int d\mathbf{r}\,\mathbf{r}\,\rho(\mathbf{r},t) . \tag{4.7}$$

One can derive the following relation between the dipole moment and the total current in the frequency domain from the continuity equation

$$\tilde{\mathbf{I}}(\omega) = i\omega\tilde{\mathbf{D}}(\omega) . \tag{4.8}$$

Substituting (4.8) into (4.6) yields an expression for the power spectrum as a function of the total current,

$$P(\omega) = \frac{\omega^2}{3}\left|\tilde{\mathbf{I}}(\omega)\right|^2 . \tag{4.9}$$

In practice, we report the power spectra from (4.9).

We explore the capabilities and limitations of TDDFT by examining the following two systems. First, we employ TDDFT to calculate the linear polarizability (and thus the absorption spectrum) of a system. Then we model the nonlinear optical response of a system to an ultra-short ultra-intense laser pulse. We compare the results to experiment in order to verify whether TDDFT can be used to study such systems.

4.2. Linear Polarizability

4.2.1. Introduction

Adler [3] and Wiser [4] suggested a method to calculate the linear polarizability in the early 1960's. This method was first adapted for DFT by Zangwill and Soven [5] in 1980. Methods stemming from this approach were applied to find the linear polarizability of various systems by many different groups (see e.g. [6-8]). The linear-response treatment of polarizability was described in Chapter 1. We implemented a method based on a real-time implementation of TDDFT. This method is described below.

4.2.2. TDDFT Calculations of Linear Polarizability

The linear polarizability, $\alpha(\omega)$, and corresponding oscillator strength, $S(\omega)$, may be calculated from TDDFT via the following real-time method. The derivation given below is based on the formulation by Tsolakidis et al [9]. The linear polarizability of a system in real time is a history-dependent function that relates the external electric field and the dipole moment of the system

$$D(t) = \int_{-\infty}^{t} dt' \, \alpha(t-t') \, E(t') \,. \tag{4.10}$$

This relation is normally shown in the frequency domain where, by the convolution theorem, it has the following form

$$\tilde{D}(\omega) = \alpha(\omega) \, \tilde{E}(\omega) \,. \tag{4.11}$$

Solving for the linear polarizability yields

$$\alpha(\omega) = \frac{\tilde{D}(\omega)}{\tilde{E}(\omega)}. \tag{4.12}$$

The equation above can be used to calculate the linear polarizability from a real-time simulation by introducing an external perturbing electric field and calculating the dipole response from the charge density (4.7). Both the external electric field and the dipole response are then Fourier transformed to the frequency domain and (4.12) is used to obtain the linear polarizability. Note that the external electric field, *E*, and the dipole moment, *D*, are real quantities in real time and therefore their frequency domain representations (i.e. $\tilde{D}$ and $\tilde{E}$) are complex quantities. For a practical calculation, we choose to apply an electric field with the following time dependence

$$E(t) = E_0\,\Theta(-t), \tag{4.13}$$

where E_0 is a constant electric field and $\Theta(-t)$ is the Heaviside function. This corresponds to a constant electric field, E_0 that is turned off at $t = 0$. We implement this by performing a ground-state calculation in the presence of a constant electric field, E_0, followed by a TDDFT calculation with the electric field turned off. The frequency domain representation of this electric field is

$$\tilde{E}(\omega) = E_0\left[\pi\,\delta(\omega) + \frac{i}{\omega}\right]. \tag{4.14}$$

Substituting this expression into (4.12) yields the following expression for the linear polarizability for positive frequencies $(\omega > 0)$

$$\alpha(\omega > 0) = -\frac{i\omega\tilde{D}(\omega)}{E_0}. \tag{4.15}$$

Invoking the relation between the total current and the dipole moment in the frequency domain (4.8), we write linear polarizability as a function of the electric field and the total current

$$\alpha(\omega > 0) = -\frac{\tilde{I}(\omega)}{E_0}. \tag{4.16}$$

Note that when extended to three dimensions, $\alpha(\omega)$ is a 3x3 tensor. If the system is rotationally invariant, one can find the average polarizability by taking the trace of the full polarizability tensor:

$$\langle \alpha(\omega) \rangle = \frac{1}{3} Tr\left[\alpha_{ij}(\omega)\right]. \tag{4.17}$$

To find the average polarizability, one calculates the polarizability along three orthogonal axes and averages the results.

The oscillator strength is related to the linear polarizability by the following equation [9]

$$\alpha(\omega) = P\int_0^{\infty} \frac{S(\omega')\,d\omega'}{\omega'^2 - \omega^2}, \tag{4.18}$$

where P indicates the principal part of the integral. One may apply the Cauchy Integral theorem to obtain the oscillator strength, $S(\omega)$, as a function of the imaginary part of the linear polarizability, $\alpha(\omega)$

$$S(\omega) = \frac{2}{\pi} \mathrm{Im}\left[\alpha(\omega)\right]. \tag{4.19}$$

The total cross section, $\sigma(\omega)$, is proportional to the oscillator strength $S(\omega)$. The total cross section can be measured experimentally so that a comparison between theory and experiment is possible.

4.2.3. Application: Sodium Clusters

Because the total cross section can be measured experimentally, it is possible to compare the experimentally observed photoabsorption spectrum with the calculated spectra (i.e. a large total cross section at a given frequency corresponds to a signal in the photoabsorption). The photoabsorption spectra of sodium clusters of various sizes were measured by Selby et al. [10,11] and Wang et al. [12,13]. Kümmel et al. [14] and Vasiliev et al. [15] calculated the photoabsorption spectra of sodium clusters with conventional linear-response theory based on DFT. The results from a linear-response calculation, a TDDFT calculation (as described above) and experiment are shown in Figure 4.1 Na_8 and Na_2 clusters. The results of the linear-response calculations along with the results from the TDDFT calculations by the method described above are compared

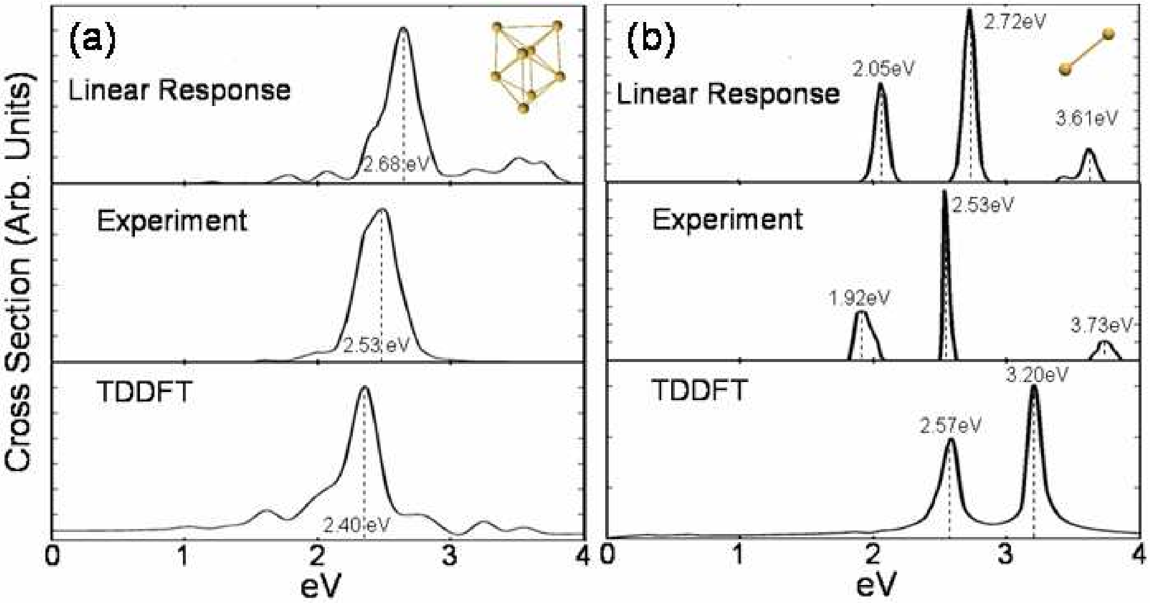

Figure 4.1: Experimentally observed and theoretically calculated cross sections for (a) Na_8 and (b) Na_2 clusters. Results from a linear response calculation [14] are given in the top panel, results from experiment [10-13] are shown in the middle panel and results from the real-time TDDFT calculation are given in the bottom panel.

with the experimental results given in Figure 4.1. For the Na_8 calculation, there is a single large feature in the experimentally observed spectrum. The TDDFT and linear-response results are both in good agreement with experiment. The peak in the TDDFT spectrum is at about 2.40 eV, which is slightly less than the measured peak at 2.53 eV. The linear-response spectrum has a peak at 2.68 eV that is slightly larger than experiment. Both the TDDFT and linear-response results include small features that are not observed experimentally – there is a small additional feature at about 1.7 eV in the TDDFT spectrum and at least three small features in the linear-response spectrum centered at about 3.6 eV. We conclude that for Na_8, both TDDFT and linear response are in good agreement with experiment and one method does not appear to offer any advantage over the other.

The TDDFT-calculated spectrum is not in good quantitative agreement with experiment for Na_2 clusters. The observed spectrum consists of three features: the largest peak at 2.53eV, a second smaller peak at 1.92eV and the smallest peak at 3.73eV. The TDDFT spectrum only has two peaks and they are blue-shifted by at least 0.6eV. The third smaller peak is missing altogether. Although the distance between the peaks and the relative sizes of the peaks are consistent with experiment, the overall agreement with experiment is quite poor.

The linear-response spectrum is still in good agreement with experiment slightly overestimating the first two features (2.05 eV and 2.72 eV) and slightly underestimating the third feature at 3.61 eV. The energy separation between the first two peaks in the linear-response calculation is about 0.67 eV slightly more than the observed 0.61 eV. The energy separation between the second and third peaks is about 0.9eV, which is significantly smaller than the 1.2 eV separation in the observed spectrum. In general, the agreement between linear-response theory and experiment is good.

Note that the spectrum for a linear-response calculation depends on the difference of eigenenergies of a DFT groundstate calculation (see Chapter I for a description of linear-response theory). On the other hand, the TDDFT-calculated spectrum depends on the natural frequencies of the physical oscillations of the electronic density when perturbed. Therefore a TDDFT calculation will only be consistent with a linear response calculation when the time-dependent density in the TDDFT calculation oscillates at frequencies that correspond to the difference in eigenvalues. We will examine the relation between the transition energies and the frequency of an electronic response in more detail in the next section.

4.3. Nonlinear Optical Response of Noble Gases to Ultra-short Laser Radiation

4.3.1. Introduction

A system that is exposed to sufficiently intense electromagnetic radiation will be driven far from equilibrium and exhibit nonlinear behavior. For example, odd harmonic generation (OHG) of light has been experimentally observed from noble gases subjected to intense infrared laser pulses [16-19]. We apply TDDFT to study OHG from the interaction of intense ultrashort (US) laser pulses with many of the noble gases. A laser pulse is considered US if it lasts less than about 1 ps (10^{-12}s). This time scale is well-suited for TDDFT calculations which have a practical upper limit of a few hundred fs (10^{-15} s).

4.3.2. Experimental Observations

Franken et al. first observed the harmonic generation of light in quartz from a ruby maser in 1961 [20]. The maser provided an intensity of about $2.7\text{x}10^{7}$ W/cm^2 with pulse length of about 1 ms and produced second harmonic generation. By 1987, McPherson et al. observed OHG in noble gases from a 248nm laser with a width of about 1 ps and a peak intensity 10^{15} W/cm^2 [16]. During the 1990's, several groups [17-19] continued to study OHG in noble gases with laser systems that could achieve larger intensities and shorter pulses (e.g. mode-locked Ti:Sapphire [21]). By about 2000, interest shifted from generating shorter pulses to elaborate phase matching techniques that can be used to manipulate the response [22,23]. For example, Bartels et al. were able to selectively excite the 27th harmonic in argon [22].

We focus on three qualitative trends that were experimentally observed. First, the number of harmonics decays rapidly and then reaches a plateau where the rate of emission is either close to constant or with a slight decay followed by another rapid fall off after which there is no measurable signal [16-19]. The results for neon for the first 17 harmonics are shown in Figure. 4.2. The scale is relative to the 5th harmonic. Notice the rapid decay followed by the slow decline.

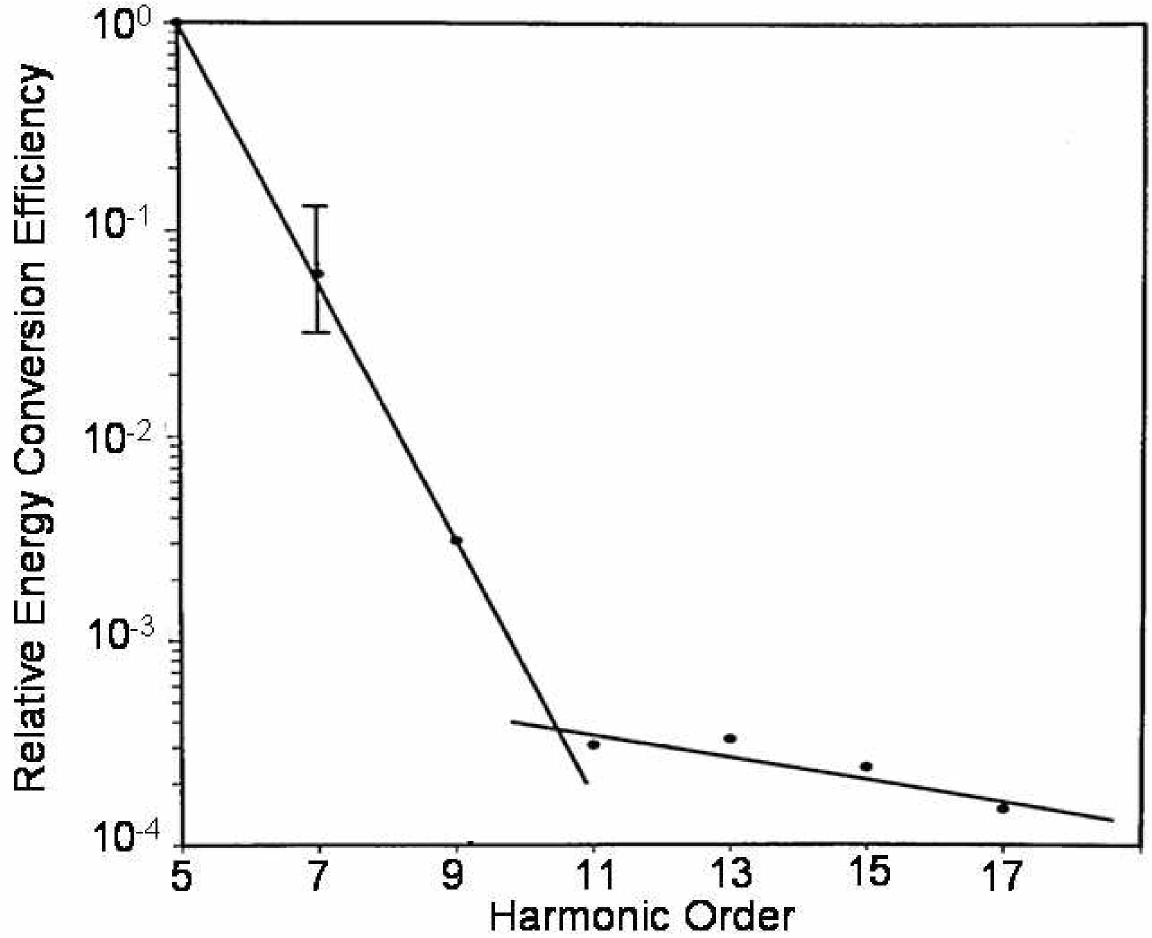

Figure 4.2: The emission strength of neon relative to the 5th harmonic [16].

A second trend confirmed by experiment was that fewer harmonics were produced as the atomic weight of the gas increased [17,18]. The OHG is shown for four of the noble gases in Figure. 4.3 for 25-fs, 805-nm pulses. Note that as the weight increases, the highest harmonic observed deceases: 105th for neon, 61st for argon, 41st for krypton and 29th for xenon [18].

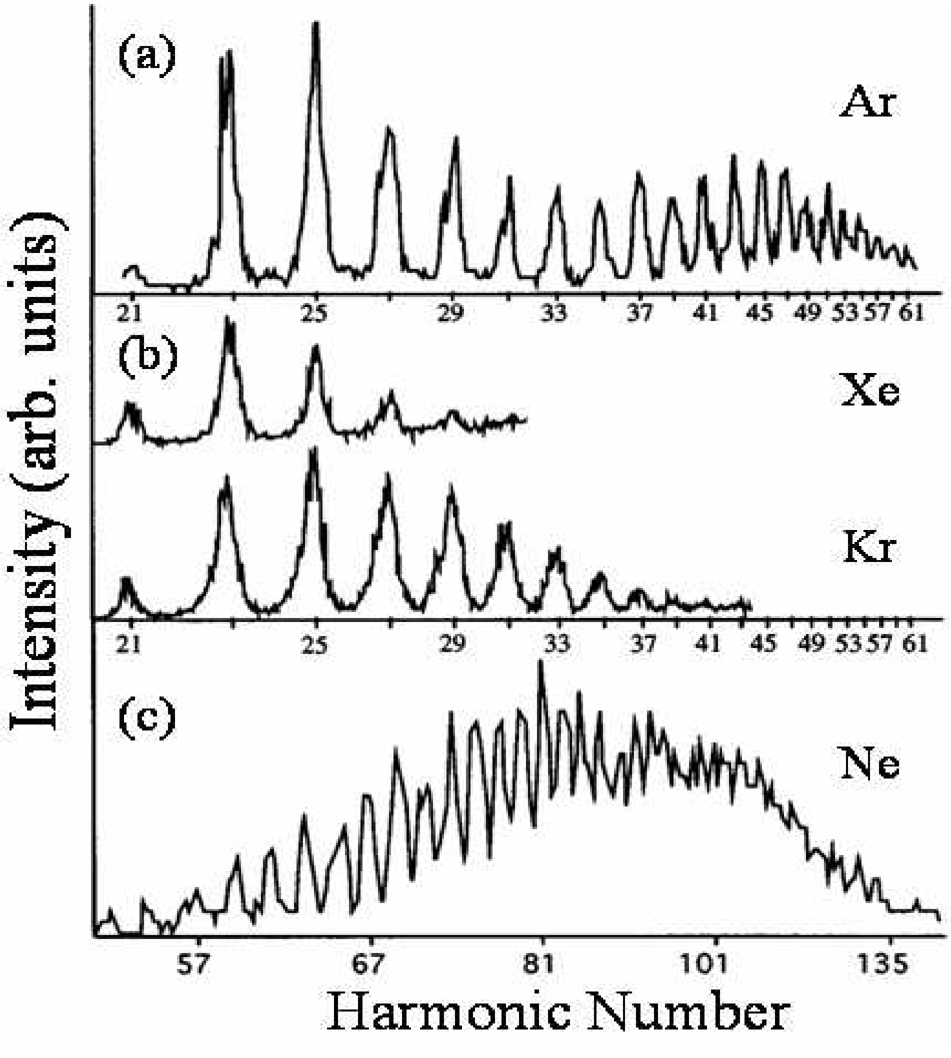

Figure 4.3: The harmonic spectra of four noble gases. The peak laser intensity for (a) and (b) was 4x10^{15}W/cm^{-2}. The peak laser intensity for (c) was 2x10^{15}W/cm^{-2}. The lower harmonic orders are artificially damped due to the grating on the spectrometer grating efficiency. [18]

Finally, the last trend of interest is that, for a given intensity, higher harmonics are produced as the pulse becomes shorter [19]. Figure 4.4 illustrates this effect for neon. The results are compiled from a number of different studies [16,19,24,25]. Note that there is also dependence on the fundamental frequency and the intensity of the pulse and the results displayed in Figure 4.4 are not due to the same intensity or fundamental frequency.

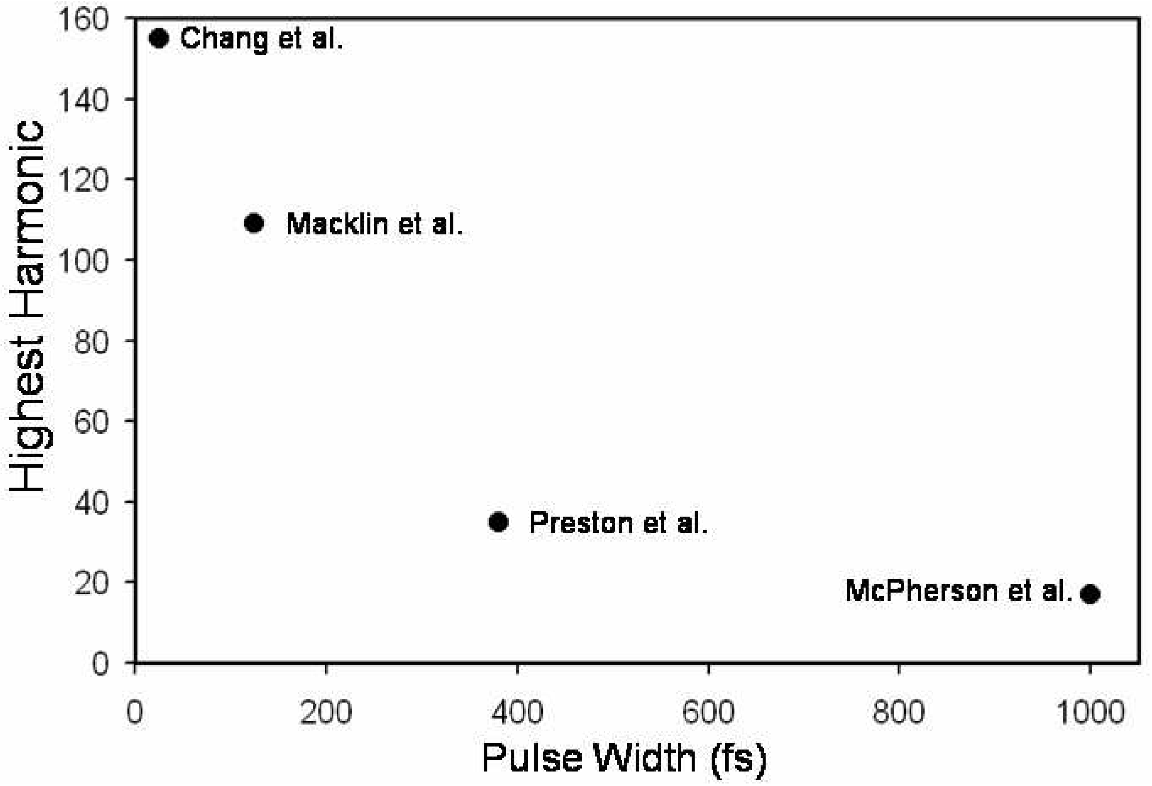

Figure 4.4: Highest harmonic observed in neon as a function of pulse width. The results are compiled from a number of different studies [16,19,24,25].

4.3.4. Theoretical Results

We pursued TDDFT calculations to study the nonlinear electronic response of noble gases under intense short laser pulses. As mentioned in the introduction to this section, light is treated as a classical field that couples to the Hamiltonian through the 3-vector potential in the canonical momentum (4.1). Moreover, we make the long wavelength approximation so that the electric field (and thus the 3-vector potential) is constant throughout space at every instant in time. We approximate an US pulse as a Gaussian-modulated electric field that varies harmonically at some frequency. The full width at half maximum (FWHM) of the pulse has the following simple relation to the standard deviation, σ, of the Gaussian:

$$FWHM = 2.35\,\sigma \tag{4.20}$$

Just as for the experiment, the pulse widths reported here are assumed to be FWHM. The magnitude of a 3-vector potential corresponding to a 21-fs pulse is shown in Figure 4.5.

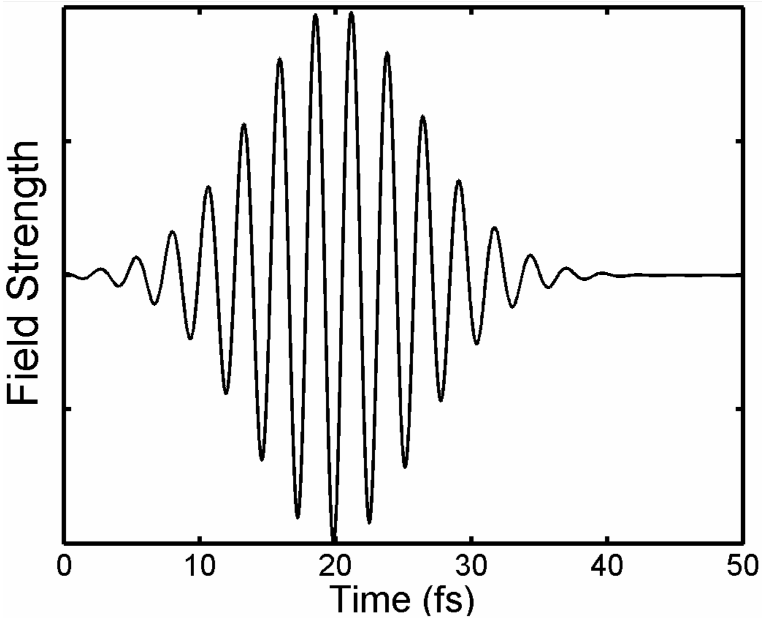

Figure 4.5: The magnitude of the 3-vector potential for a 21-fs, 800-nm pulse.

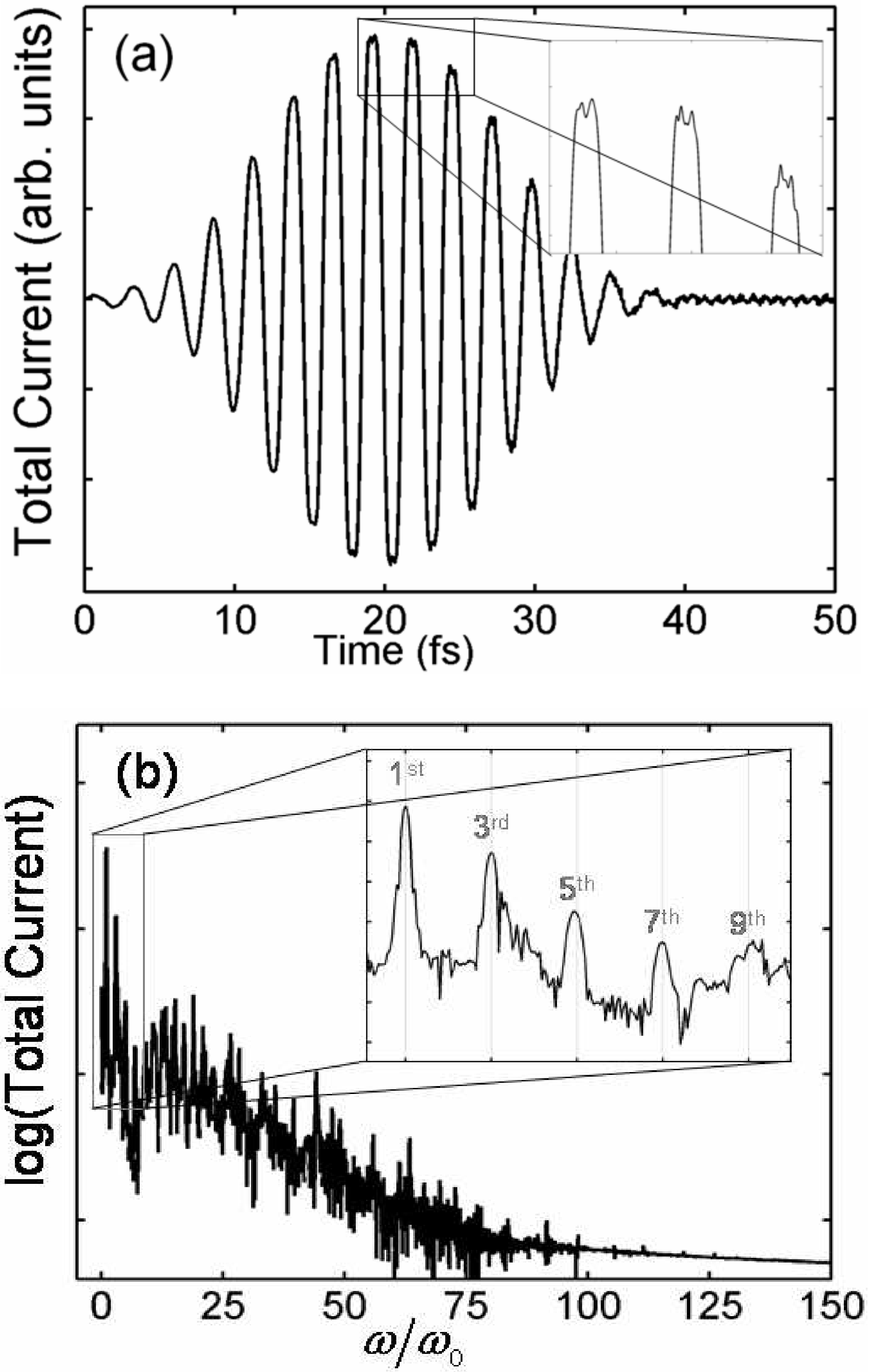

Figure 4.6: The total current response of a neon atom to a 21-fs, 800-nm pulse with an intensity of $2.7\text{x}10^{13}$W/cm^2. The first 50 fs of the total current in real time is shown in (a) and the log of the frequency space current response is shown in (b) for the first 150 harmonics of the fundamental frequency (ω_0 = 378 Thz). The inset in (a) magnifies the nonlinear-response of the current. The first 9 harmonics are shown in the inset in (b).

Figures. 4.6 (a) (b) show the total current response in real time and the log of the total current response in frequency space of an argon atom to a 21-fs, 800-nm pulse with a peak intensity of 2.7x10^{13}W/cm^2.

The power spectrum corresponding to the current response in Figure 4.6 is shown in Figure 4.7. The three black lines approximate the slope of the three regions. In the first region, there is a rapid decay in the response. The middle region consists of a long slower decay of the power spectrum. The power spectrum is flat in the last region. These features are in qualitative agreement with the experiment as reported in the previous section. There is one inset that magnifies a section of the spectrum from each region. The

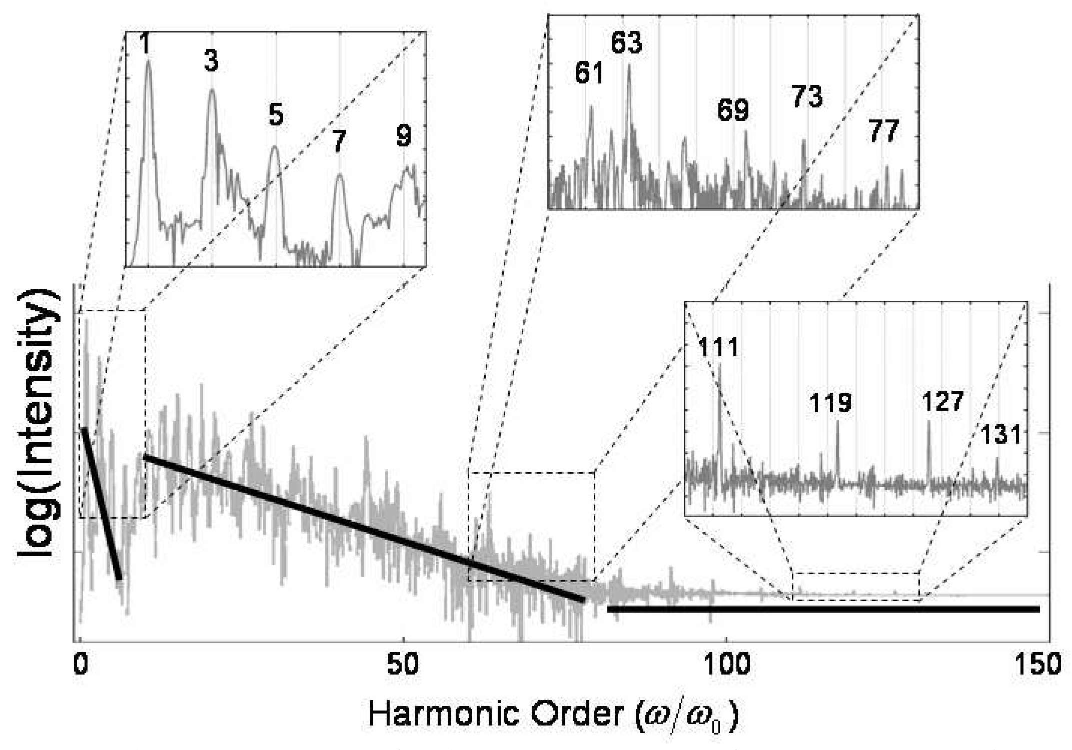

Figure 4.7: The power spectrum for the current response of an argon atom subject to an 800-nm, 21-fs pulse with an intensity 2.7x10^{13} W/cm^{-2}. There are three regions indicated by black lines. There is rapid decay in the first region up to and including the 9th harmonic. The second region consists of a long slower decay of the power spectrum. The power spectrum is flat in the third region. There are three insets that magnify sections from each region. The vertical lines in the insets correspond to the odd harmonics. The odd harmonics that can be associated with a signal are labeled.

vertical lines indicate the odd harmonics. When there is a peak in the spectrum near an odd harmonic, it is labeled.

Although there is general qualitative agreement with the observed spectra, there are several inconsistencies. First, there is a feature in the spectrum at the transition between the first and second region that is not consistent with any of the experimentally reported spectra. This feature is an effective discontinuity at about the 13th harmonic where the spectrum increases rapidly. Second, there are discernable signals in the last region of the TDDFT-calculated spectrum whereas there are no signals in the third region (after the cutoff) in the observed spectra. Third, there are signals at every harmonic in the observed spectra (see Figure 4.2). The TDDFT-calculated spectrum does not have consistent peaks at the odd harmonics and there are peaks in the TDDFT-calculated spectrum that correspond to *even* harmonics which are disallowed by symmetry at this intensity. Finally, the quantitative agreement is poor. The experimental spectrum for argon cuts off at the 61st harmonic. The largest odd harmonic observed in the TDDFT spectrum is the 111th. Note that there is some arbitrariness in reporting that the 111th harmonic is the largest in this spectrum. The criterion we used to label a signal was that the peak had to be observable on the scale of the entire spectrum and it had to be at a frequency that is an odd harmonic. For example, from the far right inset in Figure 4.6, there is a strong peak around the 127th harmonic but because it's not at the 127th, we ignore. Also, there is a small peak at the 131st harmonic which is at an acceptable frequency but it is too small to distinguish at the larger scale.

Next, check the TDDFT results for the second trend observed by experiment that the number of harmonics produced decreases as the atomic weight of the target increases

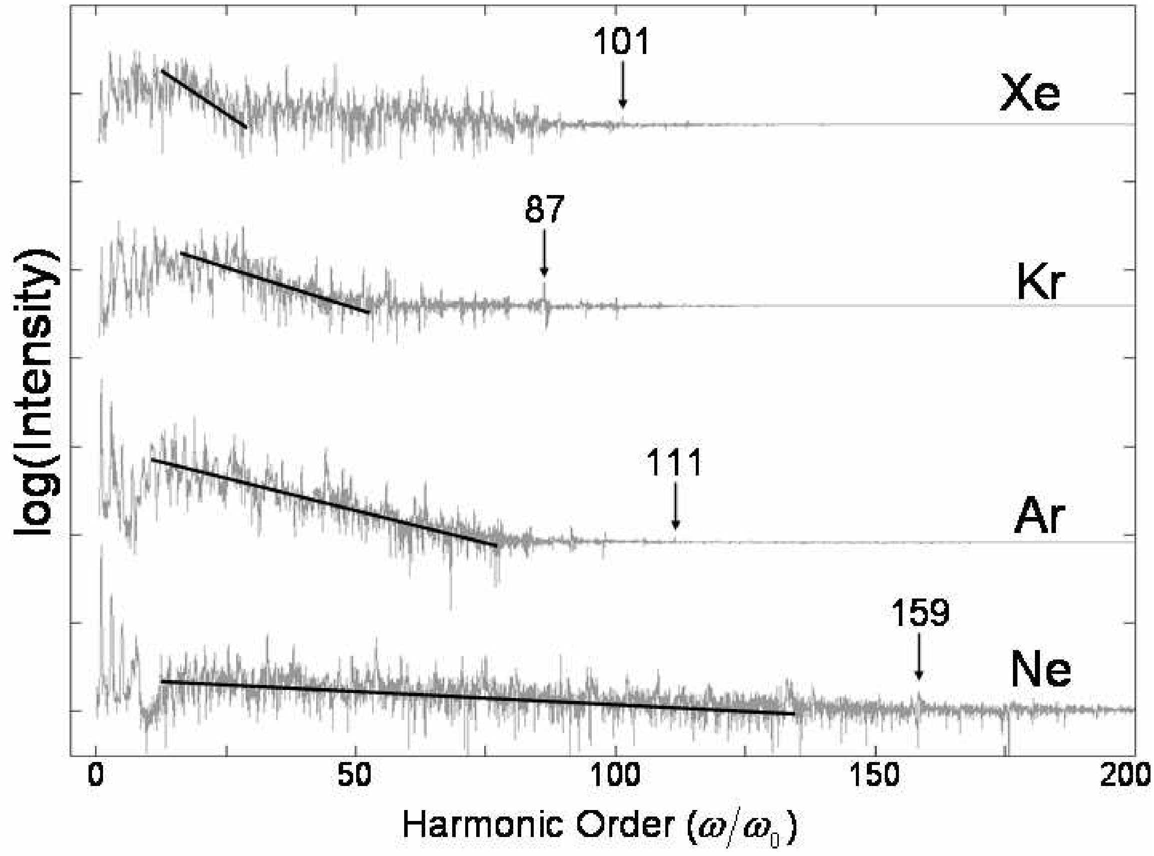

Figure 4.8: Comparison of the power spectra from the responses of neon, argon, krypton and xenon to an 800-nm, 21-fs pulse with peak intensity of 2.7x10^{13} W/cm^{-2}. The black lines are rough estimates of where the signal decays. The largest observable peaks at an odd harmonic for each atom are labeled.

(see Figure 4.2). The TDDFT-calculated intensity spectrum of four noble gases subjected to an 800-nm, 21-fs pulse with a peak intensity of 2.7x10^{13} W/cm^{-2} is shown in Figure 4.8.

In order to compare with experiment, we must first determine where the cutoffs are. If we take the cutoffs to be the largest observable odd harmonic, then the cutoffs are shown in Figure 4.8 (applying the same criteria described above). The TDDFT results are consistent with the experimentally observed trend that the larger the atom, the smaller the cutoff except for xenon, where the largest observable peak at an odd harmonic is *larger* than the largest observable odd harmonic for krypton. Moreover, the quantitative agreement is not very good (see Table 4.1). There is a large, systematic overestimation of the cutoff using this method.

Alternatively, we could evaluate the value for the cutoff using a second method. First, assume that a given spectrum has three regions as described earlier: a small quickly decaying region followed by a slowly decaying region followed by a flat signal. Take any peak in the third region as spurious and let the cutoff be the transition point between the two regions. To find this transition point in Figure 4.8, black lines roughly approximate the slope of the signal as it decays. Note that after the black lines, the signal is noisy but the average value is constant. There is arbitrariness to the placement of these lines. The xenon signal is particularly difficult because there is so much noise. There may be another very slight decay in the signal from about the 30th to the 70th harmonic. Ignoring this complication, if one assumes that the black lines provide a good representation of the second region, then the transition point is at the end of these lines are the cutoffs. The values for the cutoffs using this method are reported in Table 4.1. The qualitative agreement is better using this method since the larger atoms consistently have smaller

Table 4.1: The values of the cutoff in the spectrum are reported from experimentally observed and TDDFT-calculated spectra. The values reported for TDDFT method 1 are the largest observable peak at an odd harmonic. The values reported for TDDFT method 2 are the values at which the signal stops decaying – the transition point between the second and third regions.

	Experiment [18]	**TDDFT Method 1**	**TDDFT Method 2**
Neon	105	159	133
Argon	61	111	81
Krypton	41	87	51
Xenon	29	101	31

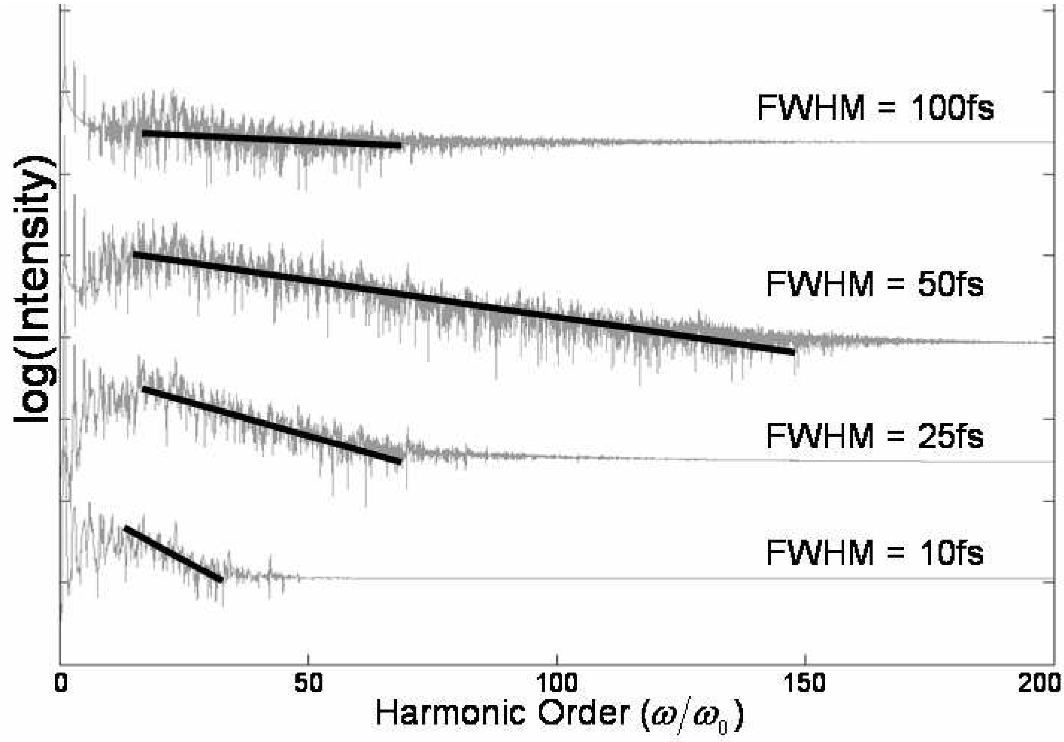

Figure 4.9: The spectra of argon subjected to 800nm light at 2.7x10^{13}W/cm^2 for four different pulse widths.

cutoffs than smaller atoms. The quantitative agreement is also much better using this second method although there remains a systematic overestimation of the cutoff.

Finally, consider the third experimentally observed trend that the number of harmonics (i.e. the cutoff) gets larger as the pulse width gets smaller (see Figure 4.4). The TDDFT-calculated intensity spectrum of argon subjected to an 800-nm pulse with a peak intensity of 2.7x10^{13} W/cm^{-2} with four different pulse widths is shown in Figure 4.19. The results clearly show the opposite effect for the TDDFT calculation for both methods described above for finding the cutoff. The longer pulses tend to generate more harmonics in the TDDFT-calculated spectra (with the exception of the 100-fs pulse). The inability of TDDFT to reproduce even the qualitative dependence on pulse width is an indication that it must be missing some essential physics.

4.4.4. Conclusions

We have demonstrated that TDDFT is able to capture the qualitative response of electrons to intense laser radiation for certain systems. However, it is clear from the lack of quantitative agreement and the failure to reproduce certain qualitative trends that TDDFT is not suitable quantitative for predictions for such systems. We believe that the error can be attributed to the following approximations that have been made in this TDDFT formulation.

First, the pseudopotential approximation requires that the core electrons sit in a spherically symmetric potential. For a typical chemical environment this is a valid approximation. However, the sufficiently intense laser light generates fields that are comparable to the field felt by a core electron due to the nucleus (on the order of 10 V/Å). Therefore the core electrons are no longer in a potential that is dominated by the spherically symmetric contribution from the nucleus.

The Adiabatic Local Density Approximation (ALDA) to the exchange-correlation potential is likely another source of error. As implied by the name, the ALDA is formally valid only when the electrons are moving slowly enough to stay on the adiabatic surface. For an electronic system that is blasted with an US laser pulse, the electrons react in a highly non-adiabatic manner.

Finally, the classical treatment of the electromagnetic fields probably contributes to the error. For example, when light couples to the Hamiltonian in this formulation where the long wave-length approximation is made there is no transfer of angular momentum between the electrons and light as there is in a real interaction because the electric field is assumed to be spatially constant at any given time. Transitions that would be disallowed by quantum mechanical selection rules occur without restriction.

For all these reasons, we believe that one should use caution when applying TDDFT with the ALDA to study the interaction of electrons and light. Although the results may not be quantitatively predictive, it is evident that TDDFT-calculations can provide insight into the dynamics of systems absorbing or emitting radiation.

4.4. References

[1] G. Vignale and W. Kohn, *Phys. Rev. Lett.* **77**, 2037 (1996).

[2] J.D. Jackson, *Classical Electrodynamics*, 3rd ed. Wiley (1998).

[3] S.L. Adler. *Phys Rev*. **126** 413 (1962).

[4] N. Wiser. *Phys Rev*. **129** 62 (1963).

[5] A Zangwill and P Soven. *Phys. Rev. A*. **21** 1561 (1980).

[6] I. Vasiliev, S. Öğüt and J.R. Chelikowsky. *Phys. Rev. Lett*. **78** 4805 (1997).

[7] A. Rubio, J.A. Alonso, X. Blasé, L.C. Balbas, S.G. Louie, *Phys. Rev. Lett.* **77** 247 (1996).

[8] K. Yabana and G.F. Bertsch, *Phys. Rev. B,* **54** 4484 (1996).

[9] A. Tsolakidis, D. Sanchez-Portal and R.M. Martin, *Phys. Rev. B*. **66** 235416 (2002).

[10] K. Selby, M. Vollmer, J. Masui, V. Kresin, W. deHeer, and W. Knight. *Z. Physik D* **12**, 477 (1989).

[11] K. Selby, M. Vollmer, J. Masui, V. Kresin, W. deHeer, and W. Knight. *Phys. Rev. B*. **40**, 5417 (1989).

[12] C.R. Wang, S. Pollack, M.M. Kappes, *Chem. Phys. Lett.* **166**, 26 (1989).

[13] C.R. Wang, S. Pollack, D. Cameron and M.M. Kappes, *J. Chem. Phys.* **93**, 3787 (1990).

[14] S. Kümmel, M. Brack, and P.G. Reinhard. *Phys. Rev. B.* **62** 7602 (2000).

[15] I. Vasiliev, S. Öğüt, and J.R. Chelikowsky. *Phys. Rev. Lett.* **82** 1919 (1999).

[16] A. McPherson, G. Gibson, H. Jara, U. Johann, T.S. Luk, I.A. KcIntyre, K. Boyer, and C.K. Rhodes, *J. Opt. Soc. Am. B*. **4**, 595 (1987).

[17] A. L'Huillier and P. Balcou, *Phys. Rev. Lett.* **70**, 774 (1993).

[18] J. Zhou, J. Peatross, M.M. Murnane, H.C. Kapteyn, and I.P. Christov, *Phys. Rev. Lett.* **76**, 752 (1996).

[19] Z. Chang, A. Rundquist, H. Wang, M.M. Murnane, H.C. Kapteyn, *Phys. Rev. Lett.* **79**, 2967 (1997).

[20] P.A. Franken, A.E. Hill, C.W. Peters, and G. Weinreich. *Phys. Rev. Lett.* **7**, 118 (1961).

[21] P.F. Moulton, *J. Opt. Soc. Am. B*. **3(1)**, 125 (1986).

[22] R. Bartels, S. Backus, E. Zeek, L. Misoguti, G. Vdovin, I.P. Christov, M.M. Murnane, and H.C. Kapteyn, *Nature*, **406**, 164 (2000).

[23] A. Paul, R.A. Bartels, R. Tobey, H. Green, S. Weiman, I.P. Christov, M.M. Murnane, H.C. Kapteyn, and S. Backus. *Nature*. **421**, 51 (2003).

[24] J.J. Macklin, J.D. Kmetec, and C.L. Gordon III, *Phys. Rev. Lett.* **70**, 766 (1993).

[25] S.G. Preston, A. Sanpera, M. Zepf, W.J. Blyth, C.G. Smith, J.S. Wark, M.H. Key, K. Burnett, M. Nakai, D. Neely, and A.A. Offenberger, *Phys. Rev. A*. **53** R31 (1996).